

Ph.D. THESIS

Chronic wound multiscale
evaluation:
from the molecular mechanisms
to an objective clinical follow-up

Marta Cullell i Dalmau

Thesis supervisors: Carlo Manzo and Marta Otero Viñas
Doctoral program: Experimental Sciences and Technology

2023



This is an era of specialists, each of whom sees his own problem and is unaware of the larger frame into which it fits.

Rachel Carson

Abstract

Chronic wounds are characterized by their inability to heal within an expected time frame. Although the clinical approach to chronic conditions has improved, there are insufficient tools to provide proper wound monitoring and early wound prognosis, and thus be able to make more informed decisions in therapies selection. On the other hand, the physiological repair of dermal wounds is regulated by molecular factors, but there is a lack of knowledge about how these molecular factors regulate fibroblast migration in the context of chronic wounds. The main objectives of this thesis are: 1) to study the effect of the vascular endothelial growth factor (VEGF) on dermal fibroblast migration in the framework of wound healing, 2) to develop new tools to help clinical staff to obtain quantitative measures of the wound healing evolution and to assess the efficacy of therapies in chronic wounds, and 3) to review the uses of artificial intelligence (AI) for skin lesion classification and develop pedagogical materials to make this technology more accessible to non-experts. Our results at the cellular and nanoscopic level about the effect of VEGF on dermal fibroblasts have brought to light some new evidence to understand the mechanisms behind therapies based on growth factors. Moreover, we implemented two tools that allow us to determine characteristic wound healing time, which is useful for early prognosis determination of wounds, and to compare the efficacy between therapies. Finally, we have provided accessible deep-learning algorithms to facilitate comprehension and acceptance of these tools by healthcare staff in the medical community. In conclusion, this thesis provides evidence of the benefits of a multidisciplinary approach to improving the comprehension of

molecular and cellular mechanisms of wound healing and introduces new technologies to support clinical wound healing follow-up and clinical decision-making.

Resum

Les úlceres cròniques es caracteritzen per la seva incapacitat de cicatritzar en un període establert de temps. Tot i que els avenços clínics han millorat recentment, encara manquen eines per realitzar un seguiment acurat d'aquestes ferides per tal de poder anticipar-ne l'evolució i que el personal mèdic pugui prendre millors decisions i seleccionar les teràpies més adequades. Per altra banda, s'ha descrit que els processos fisiològics implicats en la cicatrització estan regulats per factors moleculars. No obstant això, encara hi ha poc coneixement sobre com aquests factors moleculars regulen la migració dels fibroblasts en el context de les úlceres cròniques. Els objectius principals d'aquesta tesi son: 1) estudiar l'efecte del VEGF en l'activitat dels fibroblasts dèrmics en el context de la cicatrització de ferides, 2) desenvolupar noves eines per tal d'ajudar al personal mèdic a obtenir paràmetres quantitius que permetin determinar l'evolució de la ferida així com l'eficàcia de teràpies per al tractament de ferides cròniques, i 3) fer una revisió dels usos de la intel·ligència artificial (AI) per a la classificació de lesions de la pell, així com desenvolupar materials pedagògics per tal de fer aquesta tecnologia més accessible a no experts en la matèria. Els nostres resultats a nivell cel·lular i nanoscòpic sobre l'efecte del VEGF en els fibroblasts dèrmics aporten evidències que contribuiran a millorar la comprensió dels mecanismes d'actuació de les teràpies basades en aquests factors de creixement. També, hem implementat dues eines que permeten determinar el temps característic de cicatrització, mesura que permet determinar en estadis primerencs la prognòsis d'una ferida i comparar també l'eficàcia de diferents teràpies. Finalment, hem apropat al personal mèdic els fonaments dels algoritmes de *deep learning* per facilitar-ne la seva comprensió i acceptació en el col·lectiu de professionals de la salut. Per concloure, aquesta tesi posa de manifest que

l'abordatge de la recerca en ferides des d'una perspectiva multidisciplinària permet millorar la comprensió dels mecanismes moleculars i cel·lulars implicat en la cicatrització així com introduir noves tecnologies per facilitar el seguiment clínic de ferides cròniques i la presa de decisions clíniques.

Dedication

I want to dedicate this thesis to my family. First, to my parents, for always supporting my decisions and for the economical effort they did to pay for my expensive degree and living costs in another city. You never questioned my decision of studying a new and unknown degree and never mentioned the possible risk of that fact.

To my grandmother always kindly asked me about my Ph.D. *Iaia*, wherever you are, here is the thesis! Unfortunately, we couldn't celebrate it together.

To my husband, Jesús, to bear the weight of everything, the kids and the home, to give me time to focus on my Ph.D. To make a step to one side in your work renouncing from an exciting workplace to another with a better work schedule. Because you kindly accept those weekends and holidays I was working while I should be in a family. To be my rock, a friend to whom I can explain my problems and frustrations and who is always there.

And finally, but most importantly, to my children, Mar and Joel. This is what mama was doing all those weekends and holidays in front of the computer when you asked me to play and I said: "I can't, darling". I hope in a couple of years you could understand what a thesis means. I've done it because I love science but also to improve my career and have a better salary, to be able to offer you a good education as my parents did for me. Independently if you decided to study sciences or whatever you like, I wish one day you would forgive me for those moments being absent when you want to play or to be with your mama.

Acknowledgments

I want to acknowledge all the people who have taken part in this journey, and I'll try to don't forget anyone.

First, I want to thank my co-directors, Dr. Carlo Manzo and Dr. Marta Otero Viñas, for giving me the opportunity to do this thesis. To believe in me and think that a person with a job and two kids can do a Ph.D. I have learned a lot from your knowledge and different skills.

Thank you, Marta, for being here, always, and for sharing with me your experience in the field of animal cells. Although you have very busy scheduling, you always make a hole for me. For sharing with me your tips for writing a good manuscript and for your patience in revising the several versions of the manuscript. For our chats about the thesis and life, to read my mind and encourage me to continue in those bad days.

Thank you, Carlo, for sharing with me all your experience. To show me the process of creating a new group, and a new microscopy laboratory from the scratch. To be very patient with my lack of experience in Matlab programming and my complete absence of graphical arts skills which had been revealed during the figure creation process. To trust me, although my lack of experience, when I saw strange patterns on the screen. To push me to overcome my fears and leave my comfort zone. A few years ago, I wouldn't imagine myself writing and defending a thesis in English.

Thanks, Joan Bertran for sharing with me your experience and advice at the laboratory, always made a hole for me in your busy day. Also, to the other members of the QuBI Lab group, Clara Sandino, Xavi García, and Sergi Masó for our friendly chats and your feedback in the group meetings.

I want to thank all the nurses and members of the TR2Lab, Marta Ferrer, Fina Clapera, and Helena Sureda, for sharing with me all your clinical experience about chronic ulcers. For letting me experience a day in a wound-care unit. That day I learned that you should get out of your desk if you want to create new tools and methodologies that can be applied.

I want to thank Montserrat Masoliver, Cristina Martín, and all the technicians in the laboratory, for taking care of my cells during those days when I need to be more of a mother than a Ph.D. student.

Thank you very much Sarah Khan for your selfless grammatical revision of the manuscript. You are a good friend who can always be trusted.

To the degree students collaborating with our group during their final degree projects: Jesús Rebull, Marta Fernandez, and Francisco Navarro. With your different personalities and skills, you have made me a better person and professor. But also, for all those amusing moments and for all those laughs we share, you have made my Ph.D. funnier.

I also want to thank the Deans and heads of the department, to avoid giving me administrative tasks during this journey.

Table of Contents

Abstract	I
Resum	III
Dedication	V
Acknowledgments	VII
Table of Contents	IX
Abbreviations	1
Chapter 1. Introduction	3
1. Wound healing	3
Human skin structure	4
Extracellular matrix in skin.....	5
The wound-healing process.....	6
2. Dermal fibroblasts' role in wound healing.....	12
Single-cell migration	15
Collective cell migration	18
VEGF and biological therapies for treating chronic wounds.....	26
3. In vivo wound healing monitoring and quantification	27
Artificial intelligence as a future of wound monitoring.....	29
Segmentation process	30
Classification process.....	30
Chapter 2. Hypothesis and objectives	33

Chapter 3. Results.....	41
ARTICLE 1. VEGF-A differentially influences fibroblast migration and receptor spatiotemporal organization as a function of cell density.....	42
ARTICLE 2. A toolkit for the quantitative evaluation of chronic wounds evolution for early detection of non-healing wounds	57
ARTICLE 3. Research Techniques Made Simple: Deep Learning for the Classification of Dermatological Images	65
ARTICLE 4. Convolutional Neural Network for Skin Lesion Classification: Understanding the Fundamentals Through Hands-On Learning	75
Chapter 4. Discussion.....	84
VEGF-A differentially influences fibroblast migration and receptor spatiotemporal organization as a function of cell density (<i>article I</i>)	84
New tools to obtain quantitative values of wound healing evolution and to assess the efficacy of therapies in chronic wounds (<i>article II</i>).....	85
Improving knowledge and access to use of artificial intelligence (AI) for skin lesions classification (<i>articles III-IV</i>)	87
Chapter 5. Conclusions	90
Limitations of this doctoral thesis.....	92
Outlook and future plans.....	93
Appendix 1. Molecular techniques.....	94
Appendix 2. Wound healing and single particle tracking experiments.....	98
Appendix 3. Microscopy techniques.....	110
Bibliography.....	116

Abbreviations

AI: Artificial intelligence

$\alpha_5\beta_1$: Integrin formed by subunits $\alpha_5\beta_1$.

BSA: Bovine serum albumin

D: Diffusion coefficient

DL: Deep learning

ECM: Extracellular matrix

EGFR: Endothelial growth factor receptor

FBS: Fetal bovine serum

FA: Focal adhesions

FGF: Fibroblasts growth factor

FN: Fibronectin

GF: Growth factor

GFR: Growth factor receptor

hAb: Half antibody or reduced antibody

ML: Machine learning

MMP: Metalloproteinases

MSD: Mean-squared displacement

NA: Numerical aperture

Nrp-1 and Nrp-2 (Neuropilin 1 and 2)

PDGF: Platelet-derived growth factor

QD: Quantum dot

RGD: Arg-Gly-Asp motive

RIC: Reflection interference contrast microscopy

SPT: Single particle tracking

sVEGFR1, sVEGFR2, and sVEGFR3: Soluble forms of VEGF receptors 1, 2, and 3

TIRF: Total internal reflection fluorescence

TGF- α : transforming growth factor alpha

TGF- β : transforming growth factor beta

VEGF-A: Vascular endothelial growth factor isoform A

VEGF-B: Vascular endothelial growth factor isoform B

VEGF-C: Vascular endothelial growth factor isoform C

VEGFR-1: Vascular endothelial growth factor receptor 1

VEGFR-2: Vascular endothelial growth factor receptor 2

PRP: Platelet-rich plasma

PU: Pressure ulcers

Chapter 1.

Introduction

1. Wound healing

It is estimated that 1–2% of the population will suffer a chronic cutaneous wound in their lifetime in developed countries. Chronic wounds generally affect the adult population because of complications from aging or other comorbidities (diabetes, obesity, and cardiovascular diseases)¹². Ulcer prevalence and incidence rates are triple in the population over 75 years of age, and the presence of pressure ulcers has been associated with a 2- to 4-fold increased risk of death in the elderly. Considering that the population of elder people (aged 85 and over) is set to double over the next 20 years, the incidence of chronic wounds is expected to become a considerable challenge for health services³. It has been reported that new advanced therapies have contributed to increasing the healing of chronic wounds up to 50-60%⁴⁵. However, around 40% of wounds remain without a cure, which leads to a growing social problem with a significant impact on the use of health resources (2-3% of health budgets in developed countries)⁶⁷. More research on the wound healing process is necessary in order to contribute to the improvement of advanced therapies, which will end in an improvement in the life quality of elder people.

Human skin structure

The skin is the body's largest organ, covering the entire surface of the body (approximate area in adults of 2 m²) and it is structured in three layers: the epidermis, the dermis, and the hypodermis (Figure 1). The skin is one of the few organs in the human body that can repair and regenerate (recover its functionality) by itself after suffering an injury and it is also highly adaptive with different thicknesses and specialized functions in different body sites⁸. This characteristic is what allows the skin to perform its functions: a) a physical barrier against the environment, protecting us against temperature, ultraviolet light, pathogens, infection, and trauma; and b) immunologic surveillance, sensory perception, and control of the body's homeostasis in general⁸.

The epidermis is formed of several layers of keratinocytes. The most external one is composed of a dead cell layer filled with keratin, which has the functionality to act as a waterproof barrier and contributes to skin tone. The epidermis also contains sweat glands, sebaceous glands, and hair follicles. The dermis is rich in extracellular matrix (ECM), fibroblasts, hair follicles, blood vessels, lymphatic vessels, sweat glands, growth factors, and mechanoreceptors and provides the skin with strength, nutrients, and immunity (Figure 1). The subcutaneous adipose tissue or hypodermis underlies the dermis and functions as an energy reserve because of its composition of fat molecules and connective tissue⁸.

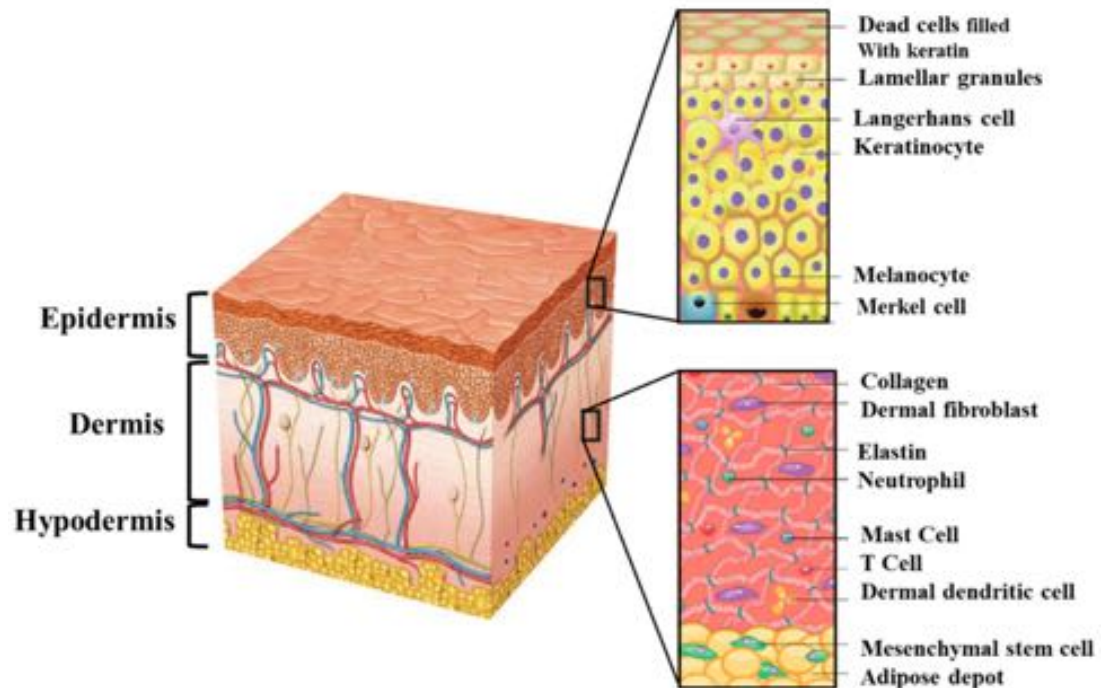


Figure 1. Anatomy of the human skin.

The skin consists of three layers: epidermis, dermis, and hypodermis organized with cellular components inserted into an extracellular matrix structure. Source Ref.⁹

Extracellular matrix in skin

Each skin layer is composed of specific cell types surrounded by the proteins of the extracellular matrix (ECM). The ECM is composed of several proteins, sugars, and other components that exercise the following main active functionalities: 1) to anchor the cells via membrane proteins to support their viability and proliferative activity, 2) to promote cell differentiation profiles through a biomechanical activity, and 3) contribute to the skin repair and regeneration after injury¹⁰. Each ECM component exercises a different contribution to skin functionality. Collagen, mostly produced by fibroblasts, endothelial, and epithelial cells, is responsible for supporting cell adhesion and migration and providing tensile strength. Elastin allows the skin to recover from continuous stretching¹¹. Fibronectin has multiple binding sites for different growth

factors such as fibroblast growth factor (FGF), platelet-derived growth factor (PDGF), and vascular endothelial growth factor (VEGF) with regulated skin cell functionality¹². Fibronectin is a multidomain structure formed by several repeats of Type I, II, and III subunits. (Figure 2). In domain 9-10, a region formed by (Arg-Gly-Asp) amino acids, called RGD epitope exists, which form the binding domain for integrins $\alpha_5\beta_1$, their principal receptor¹³. Fibronectin also has a union site for VEGF and other growth factors in domains 13-14. Some results reported that both RGD and VEGF union sites enhance migration and proliferation induced by VEGF and promote strong phosphorylation of the VEGF receptors¹⁴. The union sites of VEGF and the proximity to $\alpha_5\beta_1$ lead to a collaborative relationship that may affect cell function¹².

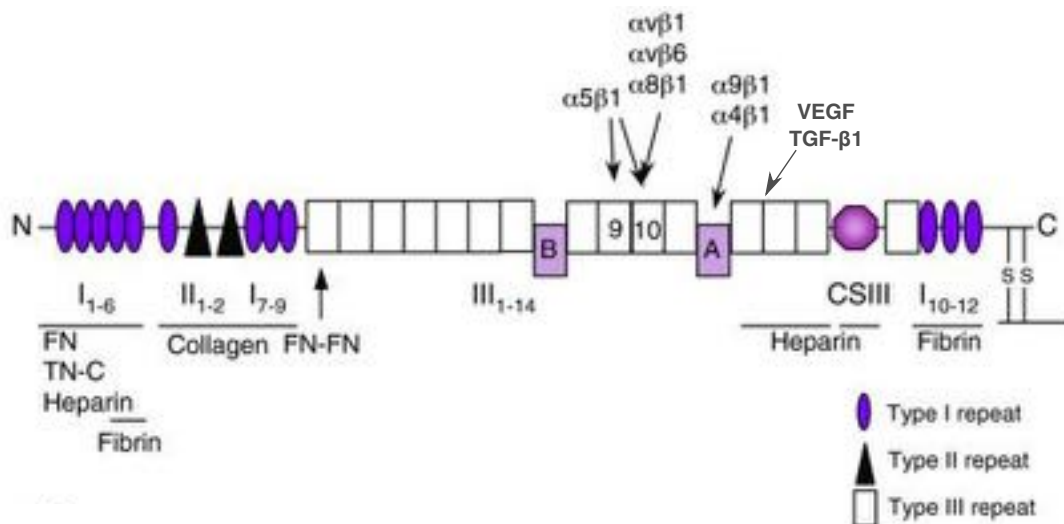


Figure 2. Fibronectin schematic structure and binding sites for other proteins

Fibronectin structure is formed by repeating homologous type I, II, and III units. Type III repeat sites are created by alternative splicing, as well as CSIII. The binding site for $\alpha_5\beta_1$, $\alpha_v\beta_1$, $\alpha_8\beta_1$, and $\alpha_9\beta_1$ integrins, as well as for heparin, VEGF, TGF- β_1 , collagen, and fibrin are also shown. Adapted from¹³.

The wound-healing process

We refer to a cutaneous wound as any alteration of the epidermal layer that can be caused by underlying pathophysiological changes or by external factors. When the

skin is injured, multiple cell types within the several skin layers need to coordinate to bring about healing. Wound healing is a complex and dynamic process starting immediately when the skin is injured and involves the reconstitution of the various layers of the skin¹⁵.

The wound healing process progresses through the following sequential and overlapping stages: hemostasis, inflammation, proliferation, and remodeling. The wound-healing process requires the synchronization of several cell types: epithelial cells, fibroblasts, immune cells, and endothelial cells.

Hemostasis phase

The hemostasis or coagulation phase starts immediately after injury to prevent exsanguination and generate a matrix to allow cell invasion to protect the vascular system. At this moment the platelets in the bloodstream are activated when they contact the collagen and other components of the injured tissue (Figure 3-1). This process of platelet activation causes the release of coagulation factors, growth factors, and cytokines that produce clot formation (stopping the bleeding) and the activation of the immune system¹⁶.

Inflammatory phase

During this phase growth factors and other cytokines released by platelets attract the cells of the immune system (neutrophils and monocyte) into the wound bed where they are responsible for preventing infection through their ability to eliminate pathogenic agents (Figure 3-2). Later, monocytes differentiate into macrophages to remove bacteria. Those cells act as regulatory cells for the inflammatory response providing different cytokines and other chemoattractant agents (growth factors like

transforming growth factor beta (TGF- β) and PDGF which allow fibroblasts, keratinocytes, and endothelial cells to be recruited to the wound area¹⁷.

The inflammatory stage progression and stop are critical for the other phases of the healing process to be properly activated. In fact, it has been described that low levels of macrophages and monocytes could produce persistent inflammation which drives healing problems like poor wound debridement, delayed angiogenesis, and delayed fibroblast proliferation and migration¹⁸.

Proliferation phase

The proliferation phase (also called new tissue generation) starts around 3 days after injury and includes five subphases that occur simultaneously: fibroplasia, ECM synthesis, angiogenesis, contraction, and re-epithelialization^{19,20}. Fibroplasia or granulation tissue is produced by the accumulation of fibroblasts that proliferate and migrate until occupying the entire wound bed (Figure 3-3). Granulation tissue is observed macroscopically and is a good clinical indicator for wound management. The active fibroblasts synthesize the ECM, mainly collagen III, which is deposited in the wound giving consistency to the newly formed tissue and acting as structural elements to support the angiogenesis process.

Angiogenesis (or new blood vessels) is critical for the progression of the proliferative phase promoting wound healing success. Local wound cells produce several angiogenic factors like transforming growth factor alpha (TGF- α), TGF- β , PDGF, FGF, and VEGF²¹. Those angiogenic factors promote endothelial cell proliferation, migration, and differentiation to generate new vessels²²

The granulation tissue formed during this phase provides volume to the wound and the fibroblasts that make it up undergo a process of differentiation into

myofibroblasts by interacting with the ECM. Myofibroblasts are a cell phenotype that is characterized by a high contractile capacity that promotes wound contraction and facilitates its closure.

Re-epithelialization, the last subphase of the proliferative phase, progresses by the keratinocytes' migration from the wound edges and allows the re-establishment of intact epidermis over granulation tissue²³.

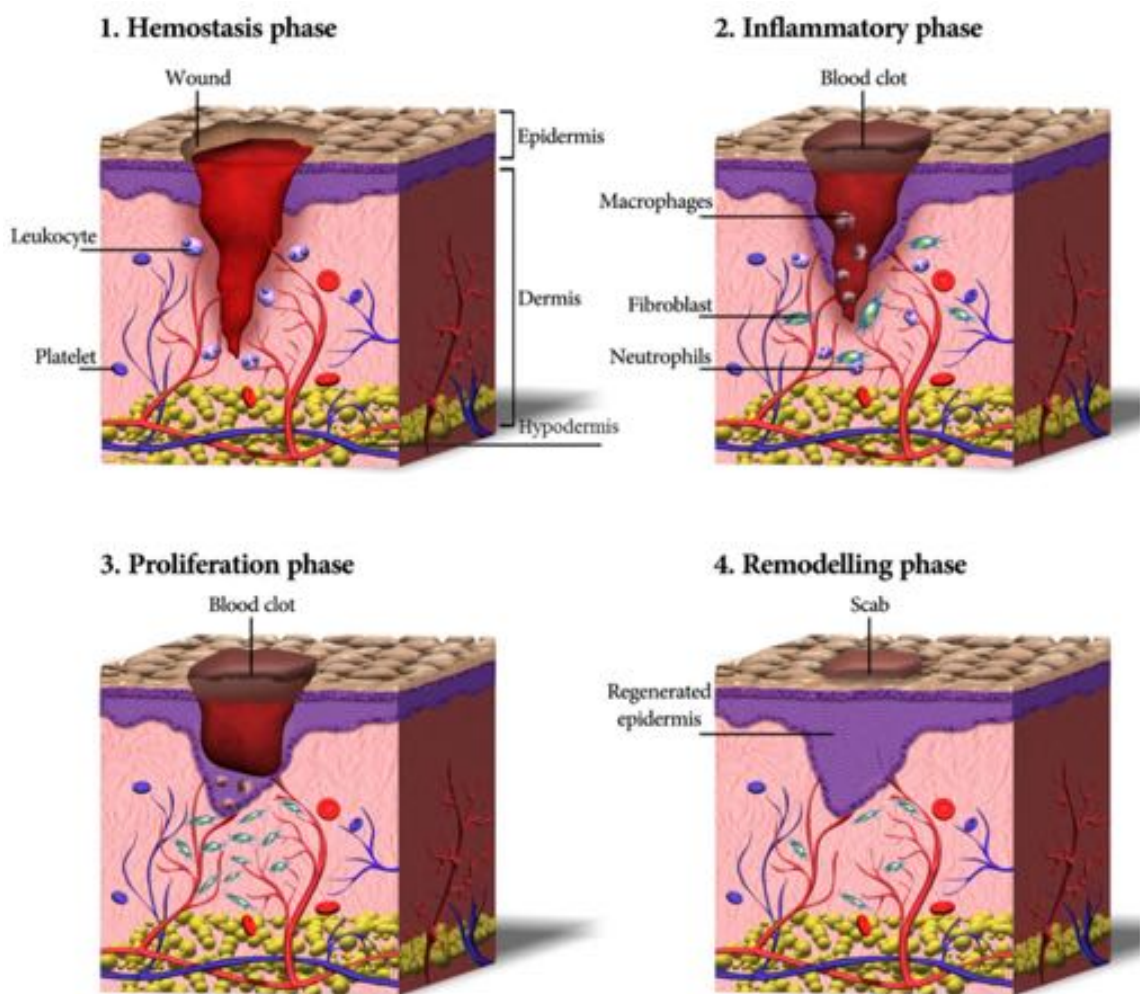


Figure 3. The wound healing phases with the essential cell types involved in this process.

Schematic diagram of wound healing process detailing the four continuous and overlapping phases: 1) Hemostasis, 2) Inflammation, 3) Proliferation, and 4) Remodeling. In each phase, the three skin layers and the main cell types involved are shown. From ref⁹.

Remodeling phase/ Maturation phase

In the last phase of the wound healing process (from day 21 to up to 1 year), the ECM experiences a lot of compositional changes. Collagen III is replaced by collagen I which increases skin elasticity (Figure 3-4). In addition, massive apoptosis of cells involved in the wound healing process produces the completed skin repair and the skin tensile strength repair²⁴.

However, several pathological conditions can alter this efficient and well-organized healing process. These conditions can slow down the healing process, which can last for long periods (weeks, months, or years) or even fail from the start, depending on the persistence of causal agents. Chronic cutaneous wounds, also known as ulcers, are characterized by their inability to heal following an orderly healing process to guarantee the anatomical and functional integrity of the wound area²⁵. The main factors that cause chronic wounds include local factors of the wound (infection, persistent inflammation, presence of necrotic tissue) and other clinical or social conditions of the patient (aging, frailty, hypoperfusion, presence of vascular diseases, diabetes, obesity, poor nutrition, excessive pressure, immunosuppression, severe burns or malignancy). Chronic wounds are heterogeneous in terms of size, body location, etiology, pathogenesis, morbidity, risk of loss of affected limb, host factors, and several other variables. The main factors that cause chronic wounds include local features of the wound (infection, persistent inflammation, presence of necrotic tissue) and other clinical or social conditions of the patient (aging, frailty, hypoperfusion, presence of vascular diseases, diabetes, obesity, poor nutrition, excessive pressure, immunosuppression, severe burns, or malignancy)²⁶.

An essential element to successfully treat chronic wounds is the correct clinical assessment, which includes the identification of the underlying cause of the wound,

called etiology. According to the etiology, the Wound Healing Society classifies chronic wounds into the following: venous ulcers, diabetic foot ulcers, arterial ulcers, and pressure ulcers²⁷. The wound etiology characterization is important for establishing appropriate wound management and treatment. The main characteristics of each wound etiology are described below:

Venous ulcers. Venous ulcers affect 5% of the adult population and are the most common wound etiology, representing about 57% of total leg ulcers. These ulcers are caused by chronic venous insufficiency due to the incompetence of vein valves which leads to elevated venous pressure due to venous reflux. The use of compression bandages is the most effective treatment for venous ulcer healing²⁸.

Diabetic ulcers. Diabetic ulcers are a common pathology in diabetic patients and represent 1% of chronic wounds. The main causes of diabetic foot ulcers are neuropathy (nerve damage causing loss of sensitivity in extremities), peripheral arterial disease, and mechanical pressure. Better control of diabetes disease contributes to the prevention of these kinds of ulcers²⁹.

Arterial ulcers. Arterial ulcers represent about 2.2% of ulcers but this prevalence increases considering that they are commonly mixed with other etiologies such as venous or diabetic. Those wounds are caused by peripheral arterial disease usually derived from atherosclerosis or other pathologies. Arterial ulcers heal when leg revascularization is achieved with surgical procedures like angioplasty or arterial bypasses²⁸.

Pressure ulcers. Pressure ulcers (PU) affect 0.02% of the population and are a common problem among patients with impaired mobility ranging from 3 to 32% of prevalence in long-term care patients. Those wounds occur over bony prominences and among the main causes are pressure but also shear, friction, moisture, and poor

nutrition. The best treatment for PU is prevention with continued repositioning of the patient³⁰. PU treatments depend on the ulcer severity and the patient's clinical conditions, and include a variety of treatments: conventional dressing, growth factors-rich therapies, vacuum therapies, and surgical reconstruction³¹.

2. Dermal fibroblasts' role in wound healing

Fibroblasts are the most abundant cells in connective tissues, and in the cutaneous tissue, they have a relevant role, especially during tissue repair after injury. As we previously described, fibroblasts play a key role in different phases of the wound healing process where they contribute at different levels such as structural filling of wound spaces or secreting ECM components and other mediators (growth factors and cytokines).

Fibroblasts can show different phenotypes depending on the tissue and can be also modified depending on the tissue functionality. Mostly, fibroblasts show an elongated or star-like cell shape, with some cytoplasmic projections with different morphologies and lengths that allow physical contact between cells. Fibroblasts have a well-differentiated cytoskeleton, especially when they acquire the myofibroblasts phenotype. Actin and alpha-actin proteins of the cytoskeleton are mostly distributed in the cell periphery promoting anchoring points of the plasma membrane with the ECM through transmembrane proteins, such as integrins. These structural interactions allow the fibroblasts to migrate through the ECM and be involved in tissue transformation³². During the wound-healing process, fibroblasts suffer several morphological and functional changes that we describe below.

Activation states of dermal fibroblasts along the wound-healing process

In the skin, fibroblasts can show different phenotypes depending on the skin's integrity and functionality, which affect their activity status. In normal healthy skin, fibroblasts are in a quiescent state characterized by having their cell cycle blocked but in a reversible mode, maintaining the ability to restart the cell cycle when conditions are favorable or stimulate cell division (Figure 4-A)³³. In this quiescent state, fibroblasts produce low levels of ECM, have no internal stress fibers, and have limited migratory activity³⁴. This quiescence state, also called cell-cell contact inhibition of proliferation, is activated by high cell density conditions allowing the regulation of tissue size to prevent uncontrolled cell expansion. Several signaling pathways are involved in this contact inhibition process, among them cadherins³⁵. Nevertheless, there is a lack of knowledge to fully understand the mechanism of this regulation³⁶.

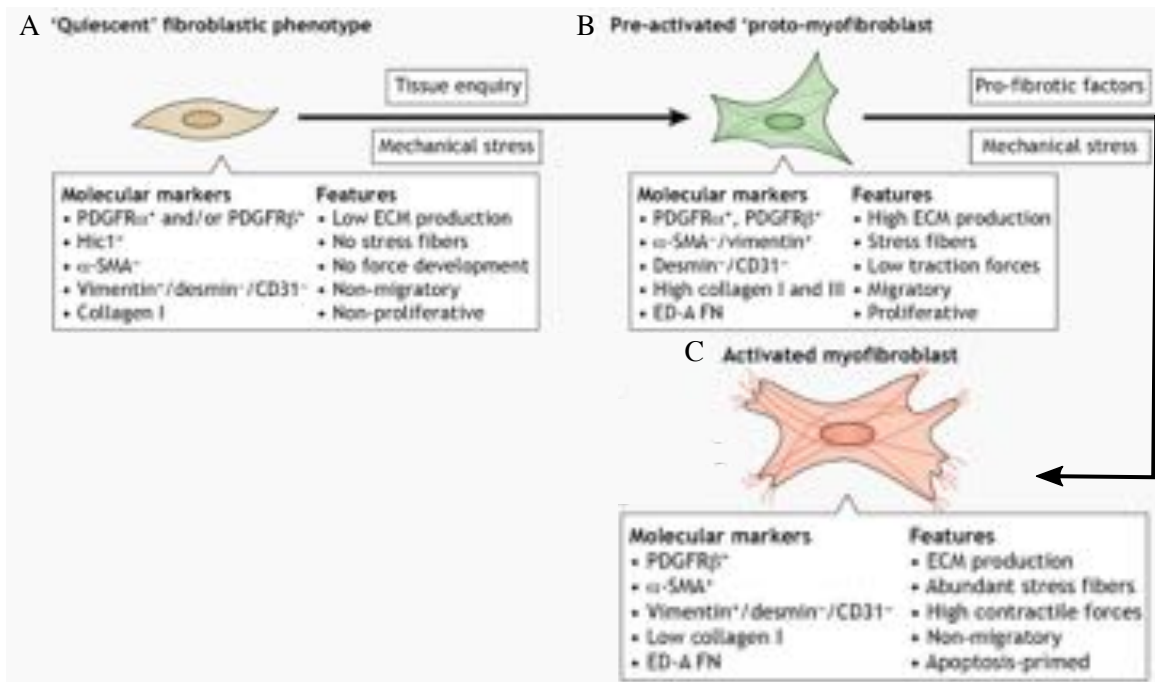


Figure 4. Fibroblasts progress during the wound healing stages and depending on the tissue microenvironment

A) Quiescent fibroblast phenotype in normal health conditions B) Continued mechanical stress activates myofibroblast precursor, which leads to pre-activated cells or proto-myofibroblasts. C) Under persistent stress and pro-fibrotic framework, fibroblasts become myofibroblasts that have a non-migratory behavior and high contractile forces. Adapted from³⁷.

Mechanical stress or tissue injury can switch fibroblasts from the quiescent to the proliferative state. Proliferative fibroblasts have stress fibers and secrete ECM proteins becoming proto-myofibroblasts or pre-activated fibroblasts (Figure 4-B). The main features of proto-myofibroblasts are their high migration and proliferation activity that, in the injury context, promote new tissue formation (granulation tissue).

In persistent mechanical forces or a pro-fibrotic environment, promoted by the presence of transforming growth factor-beta 1 (TGF)- β 1 or other cytokines³⁸, the proto-myofibroblasts can differentiate into myofibroblasts (Figure 4-C).

Myofibroblasts are a cell phenotype characterized by a high contractile capacity, due to their high expression levels of α -smooth muscle actin (α -SMA), which favors the contraction of the wound and facilitates its closure.

Myofibroblasts apoptosis is essential in the final phase of wound healing. However, in persistent fibrotic and inflammatory environmental conditions, the apoptotic mechanism fails to produce a permanent presence of myofibroblast in the tissue which impairs wound healing or produces several skin pathologies like fibrotic, hypertrophic, and keloid scars³⁷.

Role of fibroblasts migration in wound healing

As fibroblast migration is essential to promote successful wound healing, much effort has been done to understand the mechanism of action involved in fibroblast migration regulation. Several *in vitro* models have been developed to reproduce the *in vivo* conditions for a better understanding of the fibroblast migration role in wound healing, as the following: collective cell migration (to simulate migration in the context of high cell density) and single-cell migration (to study migration without the influence of cell-cell interactions). A study of the *in vitro* migration process is possible since there are fully-automated microscopes equipped with an incubation chamber to control temperature, gas, and humidity. Now we can create a proper environment for tracking living cells in culture for hours even days taking an image every few minutes.

Single-cell migration

Single or individual-cell migration experiments are those performed at low-cell densities (about 20% confluency, or less, of cell monolayer) where cells move independently. A single cell with free space around it can move in the x and y axes and

can change its direction several times during the period of study³⁹. On the other hand, cells can show a preferred migration direction (directional persistence) as a response to growth factors' gradient from zones with higher cell densities⁴⁰. This behavior makes it necessary to detect the position of each cell in each frame and finally connect those localizations to obtain trajectories. This process is usually performed with the help of tracking programs. Using the trajectory information, it is possible to determine variables like mean-squared displacement (MSD) and diffusion, but also turning angles, persistence, punctual velocity, etc. (See Appendix 2 for detailed measurements).

Cell migration is a multi-step process that implies the coordination of multiple membrane and intracellular components, so the single-cell migration assays are very useful to precisely study the cell migration mechanism. These assays are usually performed in two dimensions (2D) coating the plate surface using a specific ECM component such as collagen or fibronectin³⁹.

The single-cell migration process can be divided into several steps that can be repeated cyclically (Figure 5). From an unpolarized cell position (Figure 5-0), the asymmetric detection of cell migration-promoting agents, like cytokines or growth factors, causes the polarization of the cell⁴⁰ (Figure 5-1). Polarization is a complex process in which the main proteins related to cell movement are distributed to one cell edge. This polarization promotes actin polymerization resulting in the protrusions being pushed from the inside of the cell.

Those protrusions can create new adhesion points between actin filaments and ECM components through transmembrane receptors called focal adhesions. These focal adhesions newly created in the lamellipodium structure involve cytosolic proteins that connect several kinds of membrane integrins to the cytoskeleton. (Figure 5-2)⁴¹. These adhesion complexes confer traction points that allow the cell to move in the

migration direction while the adhesion points in the rear end of the cell detach by local proteolysis and contract (Figure 5-3) to allow the cell body translocation (Figure 5-4).

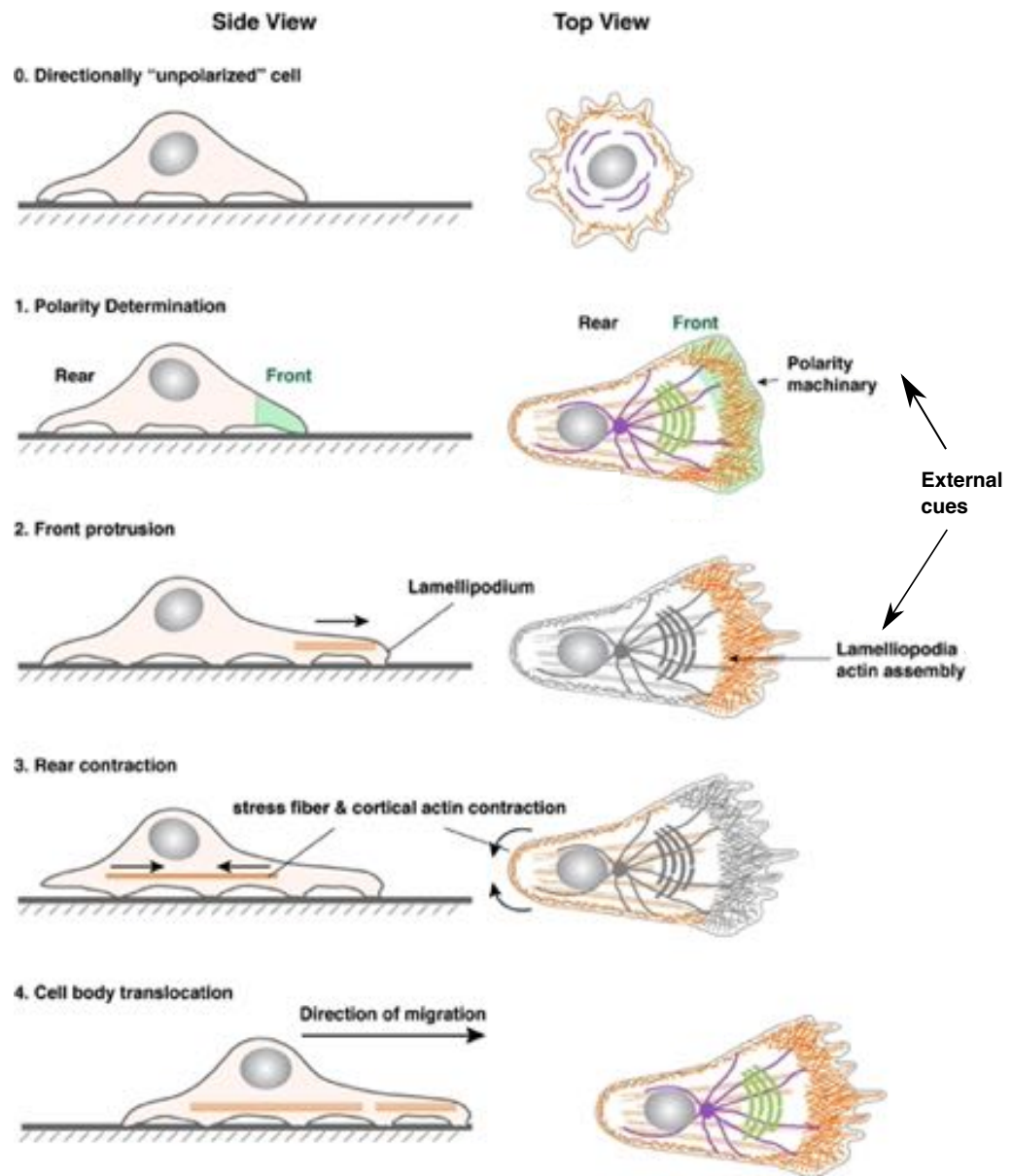


Figure 5. Steps and cellular changes in the single-cell migration process.

Diagram with both top and side views of a cell before and during migration. (0) unpolarized cell status. (1) Cell polarization determination in response to extracellular stimuli (2) Front protrusion and lamellipodium extension. (3) Rear contraction by stress fiber contraction effect. (4) Forward cell body translocation. Adapted from³⁹.

Collective cell migration

We refer to collective cell migration as the movement of multiple cells in the same direction, at the same time, and at a similar speed. This group dynamic is more directed and faster than individual cell migration because it is guided by soluble signals and by cell-cell interactions. This type of migration plays an important role during embryonic development, in cancer metastasis, and in different phases of wound healing⁴². However, different kinds of collective cell migration have been described depending on the cell type. As can be seen in Figure 6-A, epithelial cells like keratinocytes move collectively as a sheet keeping cells together with stable cell-cell junctions (adherens junctions, desmosomes, tight junctions, and gap junctions) to maintain their barrier function. However, fibroblasts, as a mesenchymal cells type, migrate collectively forming transient connections with each other. When two polarized mesenchymal cells collide, they form cell-cell N-cadherin-adhesions. This process, called contact-inhibition of locomotion produces changes in the cell migration movement because it causes the loss of polarity, retraction of cell protrusions, and finally cell re-polarization in the opposite direction⁴³. In contrast to these repulsion forces, cells are guided back to high cell density zones following a higher concentration of attractants produced for those cells⁴⁴.

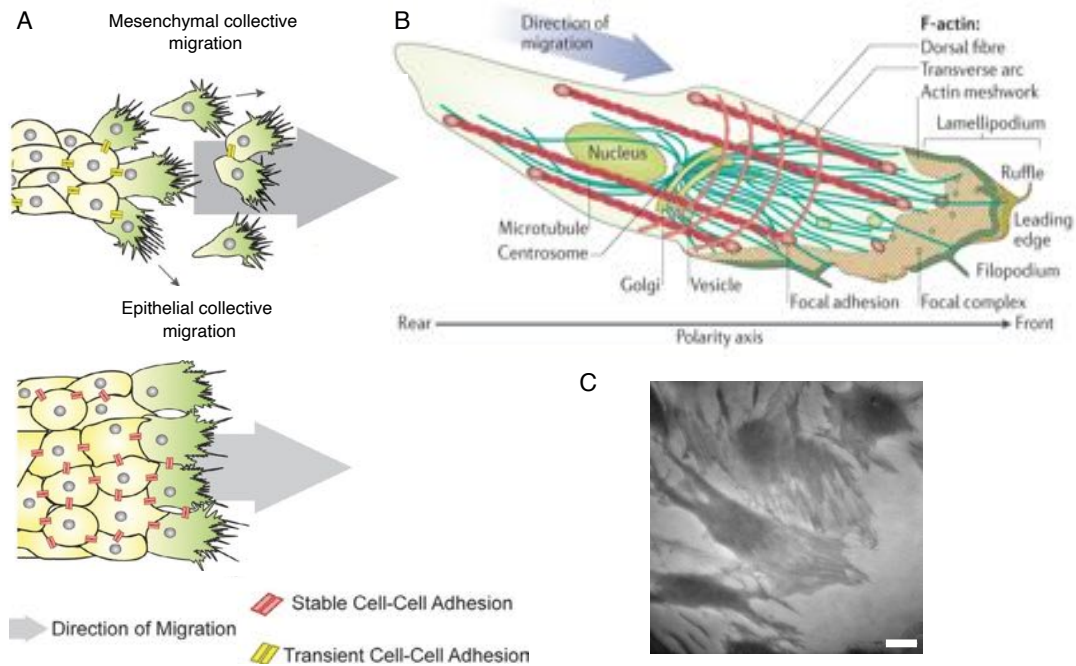


Figure 6. Collective cell migration types and cellular structures in polarized cells.

A) Top: mesenchymal cell migration behavior (i.e fibroblasts). Cells migrate directionally forming transient cell-cell connections. Bottom: Epithelial cell (keratinocytes) migration as a cohesive group, maintaining cell-cell adhesions. Adapted from⁴⁵. B) Representation of main components and organelles involved in cell polarization and cell migration. Adapted from⁴². C) Reflection Interference Contrast (RIC) image of dermal fibroblast 4h after wound (scratch) generation. Fibroblasts are polarized with protrusions in the leading edge oriented through the free space (left down part of the image). Darker parts show cell zones strongly attached to the glass. Scale bar=15 μm . Own source.

In both collective cell migration mechanisms, cells in the leading edge have the role of leaders due to their polarization (Figure 6-C)⁴⁵. As a distinctive characteristic of mesenchymal cell migration, in this case, cells in the second line and posterior become polarized when they lose contact with cells of previous lines. In addition, once transient cell-cell adhesions are broken, the cells migrate following the same steps explained in single-cell migration (Figure 5).

Collective cell migration has been traditionally studied through scratch assay experiments due to its technical simplicity⁴⁶. Briefly, this assay consists of the creation of a cell gap in a confluent cell monolayer that promotes cell migration from each edge

in the direction to the center of the gap. The cell migration rate can be determined by the quantification of the free cell area reduction by the calculation of several measures of the gap size (further details of this assay are in Appendix 1).

Integrins and their role in cell migration

Integrins are a major family of cell-surface-adhesion receptors that play important roles during developmental, and in normal and pathological cellular processes in humans. Integrins are transmembrane heterodimers of noncovalently associated α and β subunits. There are 24 different integrins in mammals resulting from the combination of 18 different α subunits and 8 β subunits (Figure 7-A). The subunits are linked through noncovalent interactions forming an extracellular ligand-binding head, two multi-domain “legs”, two transmembrane helices, and two short cytoplasmic tails⁴⁷ (Figure 7-B).

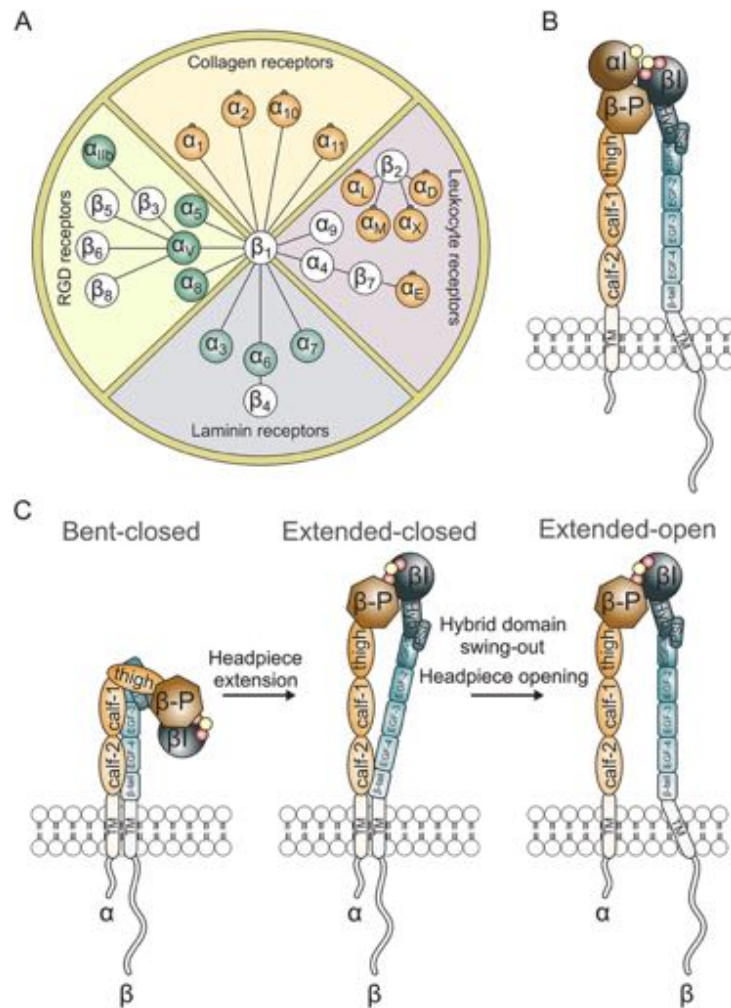


Figure 7. Integrin's family, structure, and different conformations.

A) Representation of the 24 different integrins described in mammals detailing the α and β units combination grouped by the ECM ligand they bind. B) Schematic representation of subunits α and β domains. C) Representation of several integrins conformations. Image from⁴⁸.

The principal role of integrins is to mediate the attachment of cells to the ECM ligands and transduce biochemical signals into the cells through intracellular proteins to give information to the cell about its environment⁴⁹. Remarkably, they work in a bidirectionally way, meaning they can transmit information both outside in and inside out. Inside-out signaling is an activation process of the integrins from the cytosol where protein adaptors, like talin, interact with the short cytosolic tail of the integrin triggering

a conformational change that allows integrin to bind the ligand⁵⁰. On the other hand, outside-in signaling occurs when integrins bind their ligand, which stabilizes their conformational state and, in turn, leads to integrin clustering further enhancing their avidity to the ECM ligand⁵⁰.

Depending on the activation route and status, integrins have three main different conformations: i. a bent-closed or inactive form, ii. An extent-closed conformation, and iii. An extended-open or active form (Figure 7-C). The integrins' conformation can be partially identified through the study of its mobility along the cell membrane: mobile integrins present the bent or inactive conformation and confined or immobile integrins have an extended-open conformation⁵¹.

One of the most relevant integrins involved in fibroblast migration is integrin $\alpha_5\beta_1$. This integrin belongs to a group of integrins that bind to ECM components such as fibronectin or vitronectin through the RDG epitopes of these proteins.

In normal conditions, during cell migration, small clusters of integrins appear at the leading edge binding the ECM called nascent adhesions. Those nascent adhesions evolve into bigger protein clusters, called focal adhesion complexes (FAC), formed by different types of integrins, intracellular proteins, some growth factor receptors, and cytoskeletal elements like actin bundles. The formation kinetics, shape, size, and distribution of these focal adhesions vary depending on their cell location and cell phenotype⁵². It has been reported that integrin $\alpha_5\beta_1$ is implicated in several pathologies such as cancer, inflammation, respiratory diseases, and viral infections such as SARS-Cov2. Some of the explanations for the involvement of this integrin in these pathological processes is the fact that integrin $\alpha_5\beta_1$ expression in epithelia is associated with inflammation and active proliferation⁵³. Since the regulation of the fibroblast

migration process is essential during the wound healing process, in this thesis, we are interested in studying the behavior of integrin $\alpha_5\beta_1$ in the context of wound healing.

The role of VEGF on dermal fibroblasts activity

As we previously explained, VEGF is a growth factor with an important role as a signaling molecule for the mobilization of different cell types during wound healing. In addition, there is different evidence related to altered levels of the growth factor or its receptors in chronic wounds⁵⁴. In addition, it has been reported that a decreased expression of VEGF is associated with poor wound healing⁵⁵. Several forms of VEGF have been identified in humans: VEGF-A, VEGF-B, and VEGF-C, VEGF-A being the most common form in adults. There exist 6 different isomeric forms of VEGF-A (121, 145, 165, 189, and 206), and the VEGF₁₆₅ is the most common and most biologically active⁵⁶. Cellular VEGF signaling depends on the interaction with different receptors. VEGF family receptors are composed of three receptors: VEGFR-1 (also known as Flt-1: fms-like tyrosine kinase 1), VEGFR-2 (KDR or Flk-1: fetal liver kinase-1), and VEGFR-3 (Flt-4) and two co-receptors Nrp-1 and Nrp-2 (Neuropilin 1 and 2) (Figure 8). Also, soluble forms of each VEGFR called sVEGFR1, sVEGFR2, and sVEGFR3 exist, which miss the transmembrane and intracellular domain.

The structure of the VEGF receptors is characterized by seven extracellular domains of which domains 2nd and 3rd are responsible for the interaction with VEGF and domains 4 to 7th for receptor dimerization⁵⁷.

In terms of the biological function of the VEGF receptors, it has been described that VEGFR-1 is the main contributor to the inflammation process, VEGFR-2 facilitates angiogenesis, and VEGFR-3 is expressed in lymphatic endothelium and may play a role in lymphangiogenesis. In addition, all three receptors have an important role

during embryonic vessel formation: in patients with compromised circulation, the VEGFR-2 decrease contributes to wound chronicity. On the other hand, in patients without compromised circulation, increased levels of VEGFR-1 increase the probability of wound chronicity⁵⁸. Those pieces of evidence lead us to believe that abnormal patterns of VEGFRs might be key elements of wound chronicity.

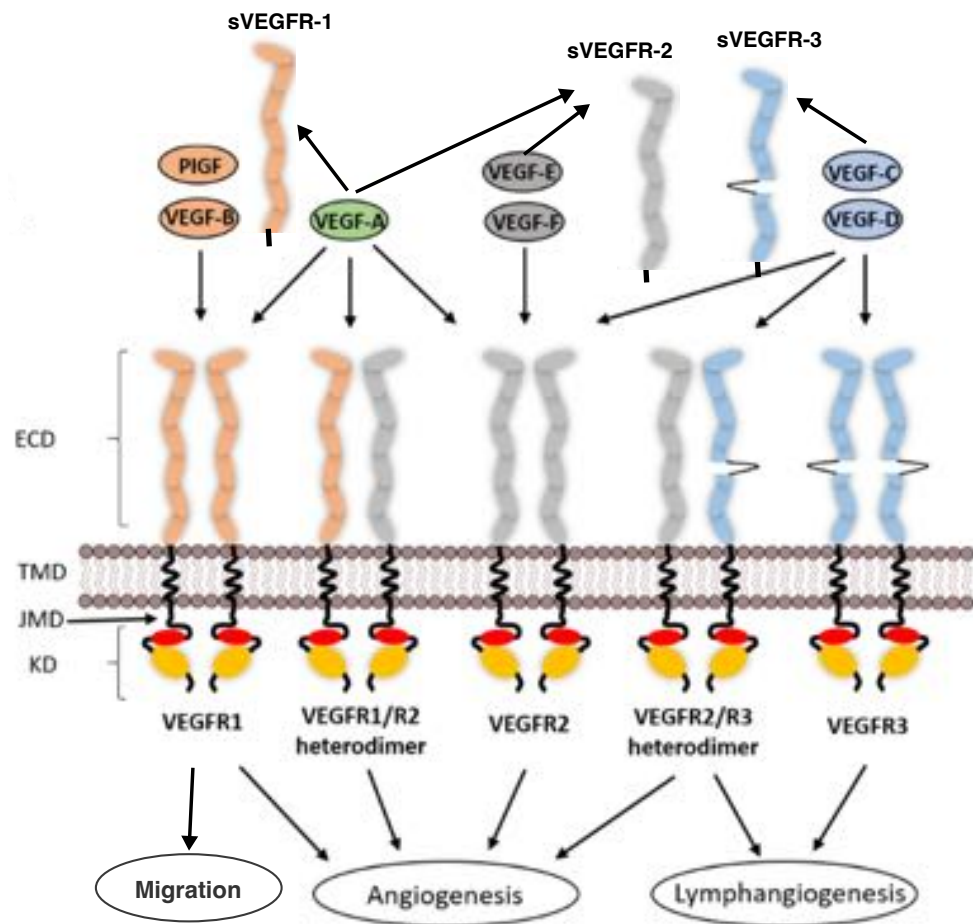


Figure 8: Schematic representation of all VEGF receptors and their ligands.

Image showing the three types of VEGF receptors in their homodimeric and heterodimeric form and some ligands. On the top, the soluble form of each receptor is represented that can also bind the ligand preventing the activation of the VEGF signaling through the full-length receptor. On the bottom the main biological function the signaling cascade activates for each receptor is reflected. Adapted from Ref. ⁵⁹.

VEGFR-1 is the only VEGF receptor expressed on dermal fibroblast⁶⁰ and for a long time, it was considered a simple decoy receptor with no signaling function, so it has

been poorly studied. VEGFR-1 binds to VEGF-A with an affinity that is approximately tenfold higher than VEGFR-2⁶¹; however, the precise biological mechanism of VEGFR-1 signaling is not well understood. VEGFR1-deficient mice exhibit overgrowth and disorganization of blood vessels. This result suggests that VEGFR-1 is a negative regulator of angiogenesis during embryonic development⁶¹. However, neither the role of VEGFR-1 signaling in wound healing is well understood nor its effect on dermal fibroblast activity.

Integrins and growth factors interactions and crosstalk

There is no reported evidence of the physical interaction between VEGFR-1 and integrin $\alpha_5\beta_1$. In addition, by making a query in the protein-protein interaction network using VisANT⁶² we observed a lack of direct interaction between both proteins (Figure 9). As can be seen in the interaction network, neither integrin subunit α_5 (ITGA5, purple) nor subunit β_1 (ITGB1, green) have direct interactions with VEGFR-1 (red). Although, there are interactions through VEGFR-1 co-receptors NRP1 (pale pink). Figure 2 shows that fibronectin has union sites for integrin $\alpha_5\beta_1$ and VEGF in closer domains. Due to this proximity, some synergetic relations between VEGF and integrins had been reported on endothelial cells⁶³.

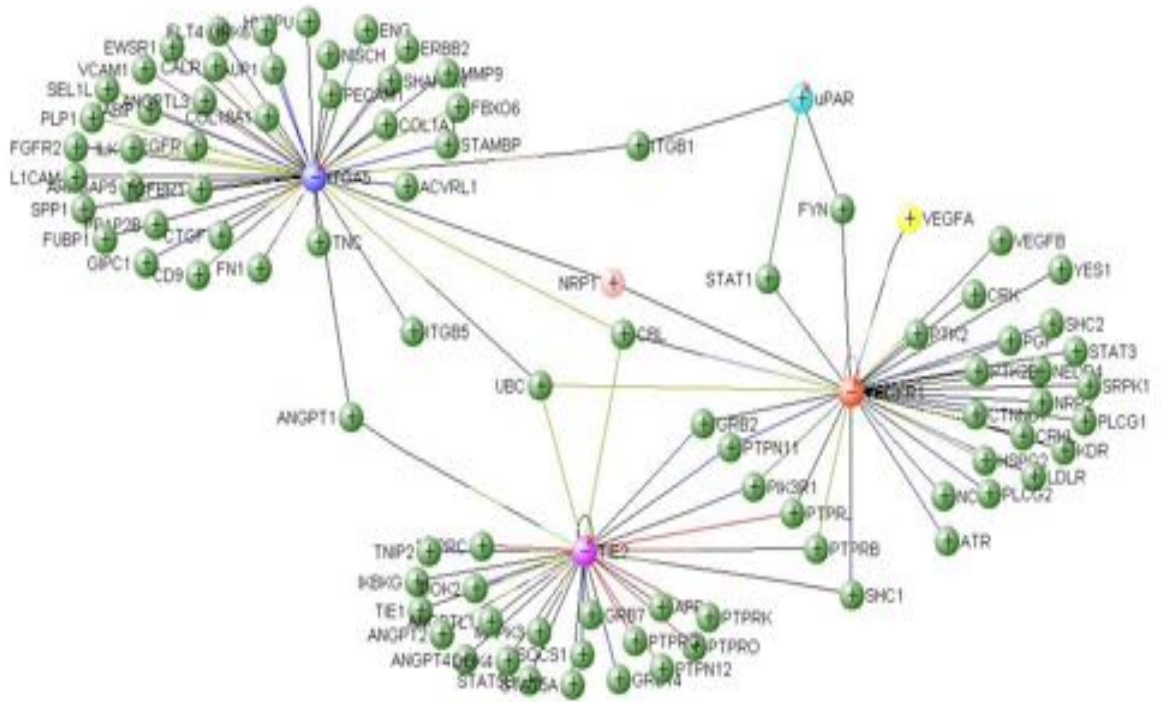


Figure 9: Protein-protein interaction network involving integrin $\alpha_5\beta_1$ and VEGFR-1.

Protein-protein interaction network performed with VisANT⁶² (accessed 11/06/2020) to study the interactions between integrin α_5 subunit (ITGA5, purple), integrin β_1 subunit (ITGB1, green), VEGFR-1 (red) and VEGFA (yellow)

VEGF and biological therapies for treating chronic wounds

One of the current advanced therapies for chronic wounds is the autologous platelet-rich plasma (PRP) therapy which is based on biological preparations rich in growth factors. Previous studies in our group have demonstrated promising results for treating chronic wounds^{64,65}. However, the different methods to prepare this therapy and the differences in patients' blood levels of those growth factors, make it difficult to characterize its composition and to study its efficacy⁶⁶. Despite the huge variability of PRP composition, several publications have described that VEGF₁₆₅ is one of the most enriched growth factors in PRP in comparison to normal blood levels⁶⁷. So, we have a

major interest in studying the role of VEGF concerning fibroblast migration for a better understanding of the efficacy of PRP therapy and its mechanism of action.

Single particle tracking (SPT) and reflection interference contrast microscopy (RICM) are powerful techniques used in the study of cell receptors. SPT allows for the visualization and tracking of individual molecules, providing information about their movement and interactions within the cell membrane⁶⁸. RICM, on the other hand, is a surface-sensitive imaging technique that can reveal the topography and composition of the membrane⁶⁹. By combining SPT and RICM, we can gain a more comprehensive understanding of the behavior and organization of cell receptors. A detailed explanation of these techniques and how we applied it can be found in Annex 3.

3. *In vivo* wound healing monitoring and quantification

Chronic wounds are complex to treat and require great expertise from clinical staff to guarantee wound resolution. The presence of several wound etiologies and the high effect of other comorbidities of patients such as diabetes or vascular diseases are among the causes of this complexity. Among the strategies with effective results, are weekly visits for wound cleaning, monitoring, and treatment application.

Wound healing monitoring techniques

Clinical wound monitoring included the visual description of the aspect of the wound, the identification of the presence of exudates, color, the presence of granulation tissue, and the precise quantification of the wound area. The determination of wound area can be difficult to quantify on some occasions by employing a ruler as it can be

irregular or formed by multiple spread ulcers. Among the methods used for wound measurement, manual and digital planimetry are considered reliable and cost-effective methods, particularly in wounds with irregular shapes⁷⁰.

To carry out a planimetry a sterile transparent adhesive film with a measurement grid (1 cm pace; OpSite flexigrid, Smith & Nephew) is placed over the wound and the wound margin is directly traced with a pen on the adhesive film (Figure 10-B). When direct contact with the wound does not constitute a matter of concern, this is the most widely used method. The ensuing evaluation of the area, performed by counting the number of squares falling within the outline, makes this method error-prone and tedious⁷¹. There are also some methods based on the market based on measurement of photography of the wound⁷². These methods usually need a reference mark with a known size near the wound to determine its real size. In some parts of the body, these methods are not very precise due to wound curvature or the difficulty to hold the reference mark, the camera, and the extremity of the patient at the same time. More complex methods, based on 3D reconstruction, volume filling, or laser scanners have also been proposed but are not routinely used due to their cost or invasiveness⁷². Despite the existence of these new devices for wound area measurement, more effort should be invested in this area to create new technologies that facilitate more precise measurements while being useful in the clinical practice setting, meaning they should be able to connect to the patient's clinical history, recording these values during the various visits.

The real interest in determining the wound area lies in being able to use these measurements for better clinical decision-making in choosing the appropriate treatment, especially for chronic wounds. In fact, as detailed in Appendix 2, various equations have been described over the years to determine the rate of healing and it has

been demonstrated that the healing rate has a predictive value in wound evolution and may also have a prognostic value. So, further studies in this area are needed to improve wound care.

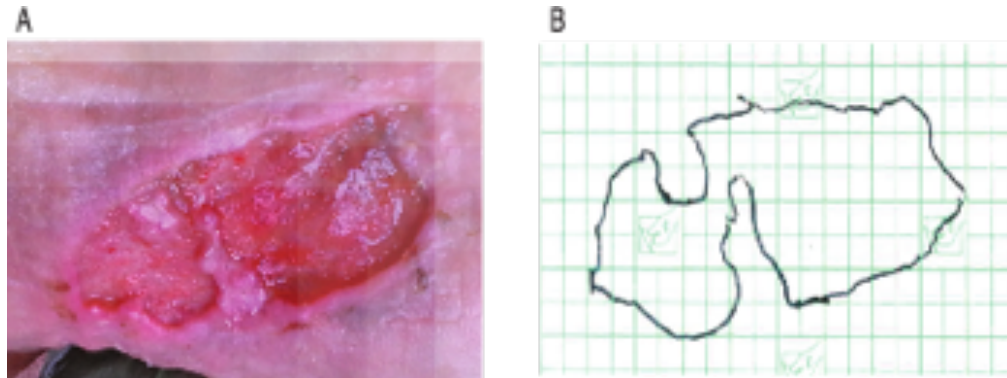


Figure 10. Leg ulcer monitoring using a planimetry

A) Image of a patient's leg ulcer. B) Detail of the planimetry from the leg ulcer using OpSite flexigrid transparent sheets. Big green squares delimited by tick lines (including 2 x 2 small squares) are 1 x 1 cm². Own source.

Artificial intelligence as a future of wound monitoring

One of the challenges in wound care practice is to have staff with the appropriate expertise to correctly diagnose wounds for later making correct decisions on wound treatment. For trainees and junior professionals, it may be very useful to have some support in this clinical decision-making especially when they are working alone. In this context, artificial intelligence tools that are currently developed might be good instruments to help these professionals. On the other hand, the accessibility of the updated variables of wound morphology in the clinical history of patients can be very helpful to clinicians for wound management follow-up.

Over the last two decades, artificial intelligence methods like convolutional neural networks (CNNs)⁷³ have become established tools for the classification of

biomedical images and they have been proposed as an instrument for clinical diagnosis in disciplines such as radiology, histology, ophthalmology, and dermatology⁷⁴. In dermatology, CNNs can be used for different finalities: i) segmentation purposes, allowing the automatic detection of skin lesion margins, and ii) classification, which permits the automatic diagnosis of the type of ulcer.

Segmentation process

Segmentation consists of the use of DL algorithms to detect and group pixels with similar characteristics and split pictures into different segments or structures⁷⁵. In the context of wound healing, this technology may be useful for the detection of skin lesions' margins to perform, in a second step, an automatic area measurement. Implementing this technology with a small device with a camera like a tablet or a smartphone can speed up the wound area measurement and the data entry of the clinical history and can save the development of tedious manual planimetry automatizing this part for reducing clinicians' time and improving the patient's comfort⁷⁸.

Classification process

Classification is the wider application of CNNs in medicine and, in concrete, in dermatology. Classification is described as the capacity of a CNN algorithm to assign a class level to a given image. That classification can be binary, which used to be in most of the clinical applications of malignant or benign lesions or multi-class classification. In the field of dermatology, important efforts have been dedicated to creating tools for the detection of skin cancer from dermoscopic images only⁷⁶ or in combination with regular photographic images⁷⁷. Without any prior knowledge about dermatology, CNNs extract and combine sets of abstract features and automatically

generate identifying characteristics (such as a combination of colors, shape, texture, border geometry, etc.) associated with the different data categories. In this way, an algorithm can learn how to achieve a precise classification of images not included in the training dataset, and even find patterns not identified by humans⁷⁸.

Those great advances in the skin lesions classification have been made possible because there are public repositories of skin lesions. The International Skin Imaging Collaboration (ISIC) has developed several repositories of skin lesions images and their metadata associated with the classification. These repositories have been used from 2016 to 2020 for the ISBI melanoma detection challenge. In those challenges, teams around the world competed for the creation of the CNN architecture that best classifies different types of melanomas and skin lesions^{76,79,80}. Unquestionably, a milestone was set by the work published by Esteva and coworkers in Nature⁷⁷, in which they trained a standard CNN architecture (Google's Inception v3) on both dermoscopic and standard photographic images using a dataset of over 100,000 images, proving that the CNN performed similarly to tested experts in classifying malignant versus benign lesions of both epidermal and melanocytic origin.

Currently, for chronic wound classification, no public database of chronic wounds exists for properly training a DL algorithm to assist clinicians in wound etiology classification or other purposes. For an adequate algorithm training process, the dataset should be representative of all types of etiologies, including the less common ones; it must ensure the presence of wounds from all human skin colors; and the images must avoid the presence of illumination reflexes that can be usual in case of wounds with wet exudate. In 2020, Wang and colleagues collected the best existing wound image collection with 1109 annotated ulcers. Wang's team in collaboration with two different health centers needed 2 years to gather this information⁸¹. Despite this great

achievement and the investment of huge efforts to carry out this project, this has a huge limitation because this dataset only includes foot ulcers, making this dataset unusable for wound diagnosis (classification) finalities⁷⁵. Therefore, it would be interesting if clinicians and researchers from all around the world could collaborate to extend the Wang's collection to include other etiologies.

On the other hand, despite the great results obtained using DL in dermatology, this technology is still poorly used or tested by doctors for several reasons. In general, clinicians have little background in computing programming skills and in using the jargon of the AI area, factors that might condition their interest in furthering their understanding of that area. It is also challenging for clinicians to be able to access testing platforms about that kind of technology, which would be the best way to understand this technology. All these factors lead to some reservations about the use of DL algorithms for assisting in the diagnosis of dermatological diseases. In addition, if physicians are not part of the teams that develop and test processes, this would increase the difficulties to validate them and for them to be accepted by the medical community.

Chapter 2.

Hypothesis and objectives

Chronic wounds are characterized by their inability to heal within an expected time frame. Although the clinical approach to chronic conditions has improved (prevention, diagnosis, and treatment) there are insufficient tools for a proper wound evolution follow-up for anticipating wound prognosis and thus be able to better decision-making in therapies selection. On the other hand, the physiological repair of dermal wounds is regulated by molecular factors generated in the dermal and blood tissues. However, there is a lack of knowledge about the mechanism of fibroblast migration regulation in the context of chronic wounds.

Our **hypothesis** is that a multiscale approach from a biophysics point of view should provide a new perspective for a better understanding of the wound healing process and gives useful tools for clinical wound healing follow-up to support clinical decision-making. This thesis' objectives are detailed as follows:

Objective 1. To study the VEGF effect on dermal fibroblast migration activity in the framework of wound healing:

- By determining the VEGF effect on fibroblasts' collective and single-cell migration in the context of high and low cell density, respectively.
- By analyzing the VEGF effect on the membrane diffusion of two membrane receptors (VEGFR-1 and integrin $\alpha5\beta1$) in the context of isolated cells and in a wound healing *in vitro* model.

Objective 2. To develop new tools to help clinical staff to get quantitative values of the wound healing evolution and to assess the efficacy of therapies in chronic wounds:

- By creating a tool for precise wound area and shape measurements.
- By developing a routine to get wound evolution parameters with prognostic value.

Objective 3. To review the uses of artificial intelligence (AI) for skin lesions classification and develop pedagogical materials to make this technology more accessible to non-experts:

- By introducing the utility of deep learning (DL) for automated skin image classification to non-experts.
- By developing pedagogical material to support clinicians and medical students in becoming familiar with the principles of convolutional neural network (CNN) used in AI tools to classify skin lesions.

Chapter 3.

Results

The development of the objectives of this thesis has led to the publication of three scientific articles and one in the process of revision, listed below. A copy of each article and a summary of the results of each one is included in this chapter.

- **VEGF-A differentially influences fibroblast migration and receptor spatiotemporal organization as a function of cell density.**

Cullell-Dalmau M, Otero-Viñas M, Masoliver M, Bertran J, Manzo C. (To be submitted).

- **A toolkit for the quantitative evaluation of chronic wounds evolution for early detection of non-healing wounds**

Cullell-Dalmau M, Otero-Viñas M, Ferrer-Solà M, Sureda-Vidal H, Manzo C. J Tissue Viability. 2021 May;30(2):161-167. doi: 10.1016/j.jtv.2021.02.009. Epub 2021 Mar 2.

- **Research Techniques Made Simple: Deep Learning for the Classification of Dermatological Images**

Cullell-Dalmau M, Otero-Viñas M, Manzo C. J Invest Dermatol. 2020 Mar;140(3):507-514.e1. doi: 10.1016/j.jid.2019.12.029.

- **Convolutional Neural Network for Skin Lesion Classification: Understanding the Fundamentals Through Hands-On Learning**

Cullell-Dalmau M, Noé S, Otero-Viñas M, Meic I, Manzo C. Front Med (Lausanne). 2021 Mar 4;8:644327. doi: 10.3389/fmed.2021.644327.

ARTICLE 1. VEGF-A differentially influences fibroblast migration and receptor spatiotemporal organization as a function of cell density.

The main objective of this study was to analyze the role of VEGF-A on dermal fibroblast migration functionality at molecular and cellular levels.

Our results on sparse cells showed that VEGF treatment increases the migration velocity but reduces the motion persistence. We also observe that those differences changed in a time-dependent fashion. On high cell density conditions, we determine the collective cell migration behavior. We again observed a rich temporal pattern and dependence of migration velocity on the initial gap area. To include these dependencies, we determine the $rate_{1/2}$ which significantly decreased as a function of VEGF-A concentration. These opposite results depending on cell density conditions led us to hypothesize possible crosstalk between VEGF-A signaling and cell-cell interactions.

We also analyzed the VEGFR-1 and integrin $\alpha_5\beta_1$ spatial distribution on the cell membrane in two experimental cell models: on cells from the wound scratch margin and cells from the unperturbed monolayer, under control and VEGF-A treatment conditions. For the integrin, we observed a mixture of diffraction-limited spots and small clusters forming focal adhesions with a higher density at the wound margin compared to those in the unperturbed monolayer. However, the VEGF-A treatment reduces the median spot size of integrin $\alpha_5\beta_1$ independently of the cell location. VEGFR-1 showed a homogeneous distribution through the membrane of diffraction-limited spots and a significant increase in spot density in cells at the wound margin. VEGF-A treatment revealed no effect on VEGFR-1 spot density.

In addition, the analysis of the VEGF-A effect, at the nanoscopic level, on the lateral diffusion of integrin $\alpha_5\beta_1$ and the VEGFR-1. For integrin $\alpha_5\beta_1$ we observed an influence of cell density with a progressive increase in the probability of undergoing

mobile motion determined in unperturbed monolayer ($\approx 10\%$), cells at the wound margin ($\approx 15\%$), or isolated cells ($\approx 30\%$) without differences in the averaged diffusion coefficient across conditions. For the VEGFR-1 most trajectories were compatible with receptor immobilization with probabilities of $\approx 15\%$ of being mobile for all conditions and we determine an average diffusion coefficient in the range of $0.1-0.2 \mu\text{m}^2/\text{s}$. In that case, the VEGF-A treatment produced small changes in the mobile fraction that correlated with those observed for cell migration. While VEGF-A nearly doubled the mobile fraction of VEGFR-1 for fibroblasts in the unperturbed monolayer and at the wound margin, the treatment produced a minor decrease in isolated cells. In fact, the average diffusion coefficient was found to be insensitive to VEGF-A treatment but was significantly higher at the wound margin and for isolated cells concerning the unperturbed monolayer.

VEGF-A differentially influences fibroblast migration and receptor spatiotemporal organization as a function of cell density

Marta Cullell-Dalmau^{1,2}, Marta Otero-Viñas^{1,2,3}, Montse Masoliver^{1,2}, Joan Bertran^{1,2}, and Carlo Manzo^{1,2,*}

¹Faculty of Sciences, Technology, and Engineering, University of Vic – Central University of Catalonia (UVic–UCC), Vic, Barcelona, Spain.

²Institut de Recerca i Innovació en Ciències de la Vida i de la Salut a la Catalunya Central (IrisCC), 08500 Vic, Barcelona, Spain.

³Tissue Repair and Regeneration Laboratory (TR2Lab), 08500 Vic, Barcelona, Spain.

*Correspondence: carlo.manzo@uvic.cat

ABSTRACT VEGF-A is a potent angiogenic growth factor that specifically acts on endothelial cells and has various effects, including the induction of angiogenesis and the promotion of cell migration. However, the role of VEGF-A in regulating cell migration and the process of wound healing is yet unclear. In this work, we used optical microscopy to investigate the effect of VEGF-A on human dermal fibroblast migration with a multiscale approach. Experiments performed on cell monolayers and individual cells were complemented with single-molecule imaging of receptors involved in adhesion and migration (the integrin $\alpha5\beta1$), and signaling (VEGFR-1). The results showed that VEGF-A treatment led to increased velocity and reduced persistence in individual cell migration. In contrast, VEGF-A treatment slowed down the collective migration of fibroblasts. VEGF-A further affected the dynamic nanoscale organization of cell surface receptors in a nontrivial way, showing a dependence on the cell density. Overall, the results highlight a complex interplay between VEGF-A signaling, cell-cell interactions, adhesion, and migration.

INTRODUCTION

Wound healing is a complex biological process that involves a series of events to restore tissue integrity after injury and requires the coordination of various cells and molecular signals. Understanding the mechanisms underlying wound healing is important for developing treatments to promote faster and more efficient healing (1).

Dermal fibroblasts are key players in the process of tissue repair and are involved in the formation of a provisional extracellular matrix (ECM) that serves as a scaffold for cell migration and tissue repair. Additionally, fibroblasts secrete growth factors and cytokines that stimulate angiogenesis and recruit immune cells to the wound site. Fibroblasts also respond to physical cues in the environment, such as mechanical stress, and can migrate towards the wound site to help close the wound and restore tissue integrity (2).

Vascular endothelial growth factor A (VEGF-A) is a potent angiogenic factor that has been shown to play a role in regulating cell migration and the process of wound healing. VEGF-A acts as a chemoattractant for fibroblasts, attracting them to the site of injury (3). This process is facilitated by the binding of VEGF-A to its receptors, Vascular Endothelial Growth Factor Receptor 1 (VEGFR-1, also known as Flt-1) and 2 (VEGFR-2, also known as KDR) (4). VEGFR-1 is widely expressed in many cell types, including dermal fibroblasts. For long, VEGFR-1 has been considered a decoy receptor that does not directly activate signaling pathways, but contributes to the overall regulation of VEGF-mediated signaling by preventing VEGF interaction with other receptors, such as VEGFR-2 (5). However, recent studies have challenged this interpretation and proposed a direct role for VEGF (6).

VEGF-A has been shown to play a role in enhancing wound

healing and tissue regeneration in the context of platelet-rich plasma (PRP), a concentrate of platelets obtained from a patient's own blood that is rich in growth factors, including VEGF-A (7). Additionally, VEGF has been shown to interplay with integrin receptors (8–10) which mediate adhesion to the ECM and modulate migration (11). Yet, clinical trials using recombinant VEGF-A reported non-significant results on wound healing treatment (12).

In this article, we use microscopy techniques to study VEGF-A effect in regulating the individual and collective migration of human dermal fibroblasts. We further apply single-molecule imaging to link cellular function to the spatial organization and dynamics of the integrin $\alpha5\beta1$ and VEGFR-1. Through the combination of imaging at the cellular and molecular level, we reveal a complex interplay of VEGF-A with the cellular locomotory and signaling machinery, involving the effect of adhesion and cell-cell interactions. The results of these studies postulate a direct role for VEGFR-1 and provide insights into the mechanisms by which VEGF-A influences the behavior of fibroblasts during migration. As such, they may have important implications for the development of new treatments for a variety of diseases and conditions.

MATERIALS AND METHODS

Cell culture and sample preparation

Primary dermal fibroblasts from newborn foreskin (ATCC, Manassas, VA, SCRC-1041) were cultured in high-glucose Dulbecco's modified eagle medium (DMEM, Gibco, 11960085) with 1% of penicillin, 1% of streptomycin, and 1% glutamine (hereafter, complete medium) supplemented with 10% fetal

bovine serum (FBS, Sigma-Aldrich, F0804) at 37 °C in 5% CO₂ atmosphere.

Primary dermal fibroblasts were seeded on fibronectin-coated 35-mm diameter glass-bottom dishes (VWR, 734-2904) in DMEM complete medium with 10% FBS at 1×10^5 cell/mL for migration assays and 3.2×10^5 cell/mL for wound healing assays. Cells were incubated for 48 h. Dishes were previously coated with 4 mg/mL fibronectin (Sigma-Aldrich, F2006) for 1 h and then blocked with 2 mg/mL bovine serum albumin (BSA). Before imaging, cells were starved for 24 h in DMEM complete medium with 0.5% FBS to arrest cell proliferation. We performed the wound healing experiments by scratching the monolayer with a sterile 200- μ L pipette tip to generate a cell-depleted region. Samples were washed twice with phosphate-buffered saline (PBS) and supplied with DMEM complete medium with 0.5% FBS (control medium). To assess the effect of VEGF-A, samples were further supplied with either 20 ng/mL or 100 ng/mL of VEGF-A 165 (Sigma-Aldrich, V5765).

For fluorescence imaging, samples were prepared as described for wound healing assays. After 4 h of treatment with VEGF-A or control medium, cells were fixed with 4% paraformaldehyde (PFA) for 10 min and permeabilized with Triton X-100 at 0.1% for 10 min. After washing, cells were blocked with 3% BSA, 2% human serum, and 20 nM of glycine in PBS for 20 min. Cells were first incubated with primary antibodies, either anti-integrin $\alpha 5$ (BD Pharmingen, 555651) or anti-VEGFR-1 (Invitrogen, SY09-09) at 5 μ g/mL for 45 min, and, after washing, with secondary antibodies (either anti-mouse IgG Alexa Fluor 488 or anti-rabbit IgG CFM 594, 5 μ g/mL for 45 min). Fluorescent beads (TetraSpeck, Invitrogen) were added as fiducial markers for channel overlay in two-color imaging. Computational analyses were carried out to ensure that the anti-VEGFR-1 antibody did not interfere with the extracellular binding site of VEGFR-1.

Live-cell single-molecule imaging (SMI) experiments were performed either on isolated cells or on cell monolayers ensuing wound healing. Samples were prepared as described for cell migration and wound healing assays, respectively. For SMI on isolated cells, no starving was performed. After 4 h of treatment, cells were washed and blocked with PBS with MgCl₂ and CaCl₂ (+/+ PBS) (Sigma-Aldrich, D8662) supplemented with 6% BSA. Cells were labeled with 0.01 mg/mL half-antibody fragments previously conjugated with streptavidin-coated quantum dots (Sigma-Aldrich, Q10121MP) dissolved in +/+ PBS with 6% BSA for 15 min at 37 °C. Samples were washed and imaged in +/+ PBS with 6% BSA. Half-antibody fragments were obtained following a protocol similar to the one used in (13). Briefly, mouse anti-human integrin $\alpha 5$ antibody (50 μ L; BD Biosciences, 610633) was dialyzed (ThermoFisher, Slide-A-Lyze MINI Dialysis Device, 2K) against PBS overnight at room temperature to replace the commercial buffer. Then, antibodies were reduced with 1 mM DTT for 30 min at room temperature and dialyzed again, using Slide-A-Lyze MINI Dialysis Device 2K, for 4h at room temperature against PBS to remove DTT. To avoid reassociation of reduced antibodies, sulfhydryl groups were blocked by incubating with iodoacetamide 20 mM for 1 hour at 4 °C with agitation. Iodoacetamide was then removed from the reaction by dialysis overnight at 4 °C. Finally, reduced

antibodies were biotinylated with a 10-fold molar excess of EZ-Link Sulfo-NHS-LC-Biotin (Thermo Scientific) for 30 min at room temperature with agitation and stored at 4 °C until use.

Imaging experiments

Experiments were performed on a Leica DMI8 inverted fluorescence microscope equipped with a total internal reflection fluorescence (TIRF) module and an environmental chamber (Okolab).

For wound healing and individual cell migration assays, samples were imaged with a 10 \times phase-contrast objective at 37 °C in a 5% CO₂ atmosphere for 24 h at time intervals of 15 min (migration) or 30 min (wound healing). For individual cell migration, we selected 5 to 8 regions of interest (ROIs) per sample in zones with approximately 20% of cell confluence. For wound healing assays, 5 to 8 ROIs were selected per sample taking care to avoid irregular zones and peripheral regions and including both the wound margins and inner regions of the cell monolayer.

For fluorescence and live-cell SMI, samples were illuminated in TIRF geometry. Excitation was provided by the light of two CW lasers (Obis, Coherent, $\lambda=488$ nm, 1 kW/cm² and Oxxius, $\lambda=561$ nm, 2.5 kW/cm²). Fluorescence was collected through an oil-immersion objective (Leica, 100 \times , NA = 1.47) and guided toward an sCMOS camera (95B, Photometrics) using proper filters (Chroma). For SMI, movies were recorded at a frame rate of 50 Hz at 37 °C in a 5% CO₂ atmosphere. Reflection interference contrast (RIC) images were obtained by illuminating the sample with an LED (pE300, CoolLED) filtered with a bandpass filter (Chroma) and collecting the reflected light through a 10/90 beam splitter (Chroma).

Image processing and statistical analysis

For individual cell migration assays, cell detection and tracking were performed with ImageJ using the plugin Track-Mate (14) with a blob diameter of 40 μ m, a maximum linking distance of 30 μ m, a gap closing distance of 50 μ m, and a maximum frame gap of 2 frames. Only trajectories longer than 30 frames (corresponding to 7.5 h) were used for further quantification that were performed in MATLAB (the MathWorks Inc., Natick, Massachusetts) using custom scripts. For wound healing assays, images were analyzed using scripts written in MATLAB based on the algorithm described in (15) to detect the area corresponding to the wound region. Further kinetic parameters were calculated using custom MATLAB scripts (16). For fluorescence imaging, spots were detected in MATLAB following a pipeline similar to the one described in (17). For live-cell SMI, movies were analyzed using the u-track package (18). Trajectories were quantified and classified according to the algorithm described in (19).

Statistical analysis were performed in R (R Core Team, 2022). For data that did not pass the normality test, statistical significance was calculated with the Kruskal-Wallis test followed by *post hoc* Wilcoxon test. Sample sizes were based on previously published experiments in which statistical differences were identified.

RESULTS

VEGF-A differentially influences the collective and individual cell migration

Individual cell migration

We first sought to investigate the effect of VEGF-A treatment on the individual migration of human dermal fibroblasts *in vitro*. We thus performed time-lapse microscopy and recorded the motion of cells seeded at a low confluence on fibronectin-coated coverslips. We used tracking software (14) to reconstruct individual cell trajectories (Figure 1A-B) and estimate kinetic parameters for ≈ 1000 cells in each condition. Trajectories of individual cells in both conditions showed a directional persistence (Figure 1B) with a distribution of the turning angle pronouncedly peaked around $\phi = 0$ (Figure 1C). The calculation of the average velocity (Figure 1D) and the motile persistence (i.e., the end-to-end displacement divided by the total displacement, Figure 1E) for each cell revealed small but significant differences in cell motility upon VEGF-A treatment, characterized by a higher velocity and reduced persistence.

To better understand these differences, we represented these two quantities as a function of time (Figure 1F-G). The velocity displayed a progressive increase up to ≈ 12 h from the beginning of the experiments (Figure 1F). Treated cells moved faster in the first phase of the experiments, until ≈ 7 h. The directional persistence of cells in control conditions slightly increased over time, whereas cells treated with VEGF-A maintained a rather constant persistence (Figure 1G). Cells in both conditions showed comparable persistence values for the first ≈ 7 h, after which they showed a diverging behavior. As a further test, in Figure 1H we quantified the mean-squared displacement for each trajectory, which displayed the typical superdiffusive behavior with scaling exponent $1 < \alpha < 2$, as expected for the active process of cell locomotion (20). In agreement with the results obtained for the motile persistence, we observed a significant reduction of α upon VEGF-A treatment (Figure 1I).

VEGF-A seems to promote a faster yet less persistent motion for isolated cells. Our data seemingly indicate the occurrence of a time-dependent mechanism, defining two temporal regions responsible for the differences observed in Figures 1D-E.

Collective migration

To gain insights into the mechanism responsible for changes in fibroblasts' migration induced by VEGF-A, we reckoned to measure the collective migration properties of fibroblasts. We performed wound healing assays by scratching cells' monolayers and imaging them using phase-contrast microscopy (Figure 2A), both in control medium and with VEGF-A treatment. The time-lapse imaging shows a progressive reduction of the initial wound area over time due to the movement of the two wound margins until the monolayer is fully reconstituted (Figure 2A). Time traces of the wound area vs. time corresponding to similar values of initial wound area (Figure 2B) suggested a progressive slowdown of the wound healing process as a function of VEGF-A concentration (Figure 2B) and a reduction of the longitudinal wound closure rate (Figure 2C).

Figure 2C also shows that the closure rate exhibits a rich temporal pattern that was hardly reproducible for different wounds and regions of interest. Together with the variability in initial gap length, this made difficult the quantification of kinetic parameters. A plot of half the initial gap size ($\text{gap}/2$) as a function of $t_{1/2}$, i.e. the time to reduce the gap to half of its initial value (Figure 2D), showed a positive correlation between the two quantities and a change of slope upon VEGF-A treatment. To monitor the wound healing velocity and mitigate the dependence on the initial gap size, we thus calculated $\text{rate}_{1/2} = \frac{\text{gap}}{2 \cdot t_{1/2}}$ for every region of interest previously imaged. As shown in Figure 2E, $\text{rate}_{1/2}$ significantly decreased as a function of VEGF-A concentration.

In contrast to the experiments of individual migration, VEGF-A seems to slow down the collective migration of fibroblasts. This evidence led us to hypothesize a possible crosstalk between VEGF signaling, cell-cell interactions, and scratch-induced signaling in migration.

The spatial distribution of integrin $\alpha 5 \beta 1$ and VEGFR-1 is influenced by cell density and VEGF-A treatment

Migration experiments suggested a complex interplay of VEGF-A with other signal mechanisms involved in migration. We thus focused our investigation at the molecular level by studying the spatial organization of two membrane proteins: the integrin $\alpha 5 \beta 1$, a major cellular receptor for the extracellular matrix protein fibronectin, that plays a fundamental role in adhesion and migration (21) and the VEGFR-1 receptor, involved in the activation of several intracellular signaling pathways upon VEGF-A binding (22).

We used RIC and TIRF microscopy to image the basal membrane of fibroblasts and determine the spatial distribution of both receptors after scratching. We performed experiments both on cells forming the unperturbed monolayer or at the wound margin, in control medium or with VEGF-A treatment (Figure 3A). In all the cases, RIC imaging (Figure 3A, top panels) showed well-stretched cells, with an elongated shape in the unperturbed monolayer and a large adhesion area at the wound margin. The TIRF images obtained for the integrin $\alpha 5 \beta 1$ (Figure 3A, middle panels) revealed a mixture of diffraction-limited spots and small clusters, forming focal adhesions (FAs) or fibrillar adhesions aligned along stress fibers (23).

The density of these structures was higher in cells at the wound margin as compared to those in the monolayer, as further confirmed by the image quantification in Figure 3B, whereas VEGF-A produced no difference. However, VEGF-A produced a reduction of the median spot size, independently of the cell location and concentration (Figure 3C). TIRF imaging of VEGFR-1 showed the occurrence of diffraction-limited spots with a quite homogeneous distribution throughout the membrane (Figure 3A, lower panels). Similarly as observed for the integrin $\alpha 5 \beta 1$, the quantification of the spot density revealed no effect of VEGF-A treatment but a significant increase in spot density for cells at the wound margin (Figure 3D). As shown in Figure 3E, the spot size was roughly constant, independent of both the treatment and the cell location.

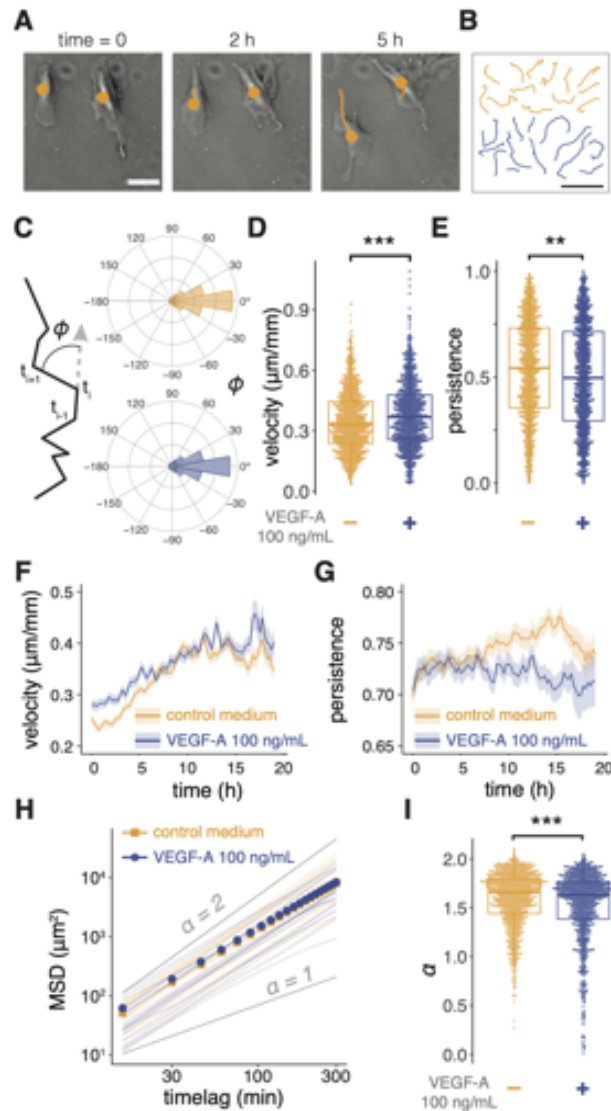


Figure 1: VEGF-A effect on individual migration. **A** Phase-contrast images of a region of interest from a cell migration experiment at different times. Orange circles and segmented lines indicate the centroid of the detected cells and the linked trajectory. Scale bar = 150 μm . **B** Representative trajectories of the same duration (20 h) obtained for cells in control medium (orange) and 100 ng/mL VEGF-A (blue). Scale bar = 500 μm . **C** Schematic of the calculation of the turning angle ϕ and rose plots of ϕ for cells in control medium (orange) and 100 ng/mL VEGF-A (blue). **D-E** Boxplot of the average velocity (**D**) and the motile persistence (end-to-end displacement divided by total displacement, (**E**) measured for each cell in the two experimental conditions. **F-G** Cell velocity (**F**) and motile persistence (**G**) as a function of time. Continuous lines represent the average values calculated over a time window of 3 frames (velocity) or 10 frames (persistence), and the shaded areas correspond to the standard error of the mean. **H** Log-log plot of the mean-squared displacement (MSD) versus the timelag. Colored lines correspond to exemplary trajectories and symbols to their ensemble averages. Gray lines depict the scaling law of Brownian motion ($\alpha = 1$) and ballistic motion ($\alpha = 2$) and are meant as a guide to the eye. **I** Boxplot of the anomalous diffusion exponent α obtained from the power law fit of the MSD for each cell in the two experimental conditions. Differences were assessed through a two-tail Wilcoxon test (\cdot : **: $p < 0.01$, ***: $p < 0.001$). Data correspond to $n = 1002$ cells, 3 technical replicates (control) and $n = 921$ cells, 3 technical replicates (VEGF-A).

The lateral diffusion of the integrin $\alpha 5\beta 1$ and VEGFR-1 is influenced by cell density and VEGF-A treatment

The experiments discussed so far provided interesting hints about the role of VEGF-A for dermal fibroblast migration. First, VEGF-A showed a small but nontrivial effect on cell migration. Second, the density of both integrin $\alpha 5\beta 1$ and

VEGFR-1 was enhanced in cells with a pronounced migratory phenotype, as those at the wound margin. However, the presence of VEGF-A seemed to reduce integrin $\alpha 5\beta 1$ clustering. To gain more insights into the effects observed at the molecular scale and link them to the migration properties, we performed live-cell SMI to study the lateral diffusion of integrin $\alpha 5\beta 1$ and VEGFR-1 in control condition or upon VEGF-A treatment in different cellular arrangements (Figure 4).

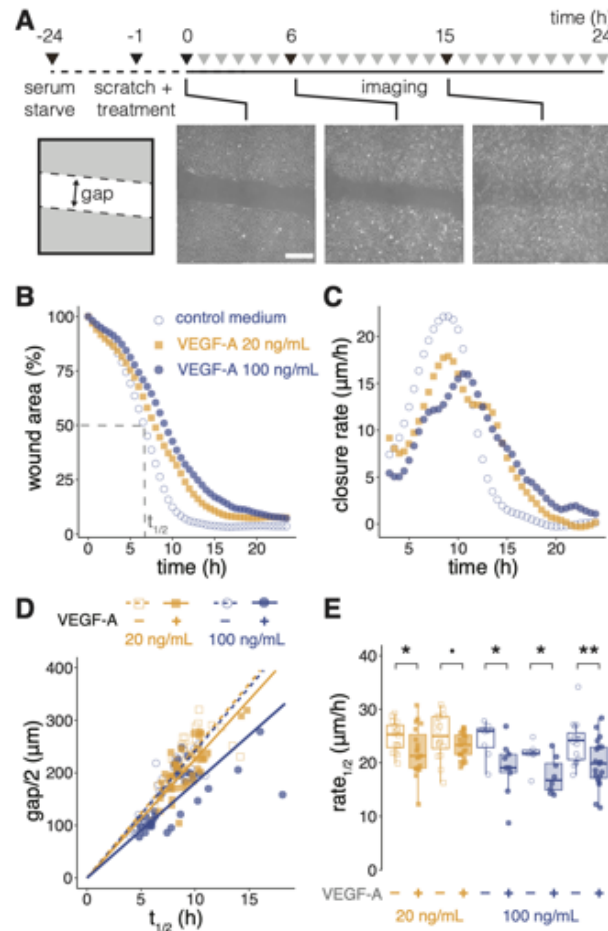


Figure 2: VEGF-A effect on collective migration. **A** Schematic of the experimental procedure used for the wound healing assay and exemplary phase-contrast images of the same field of view at different times. Scale bar = 500 μm . **B** Time traces of the percentage of wound area versus time for representative experiments having similar initial wound gap size performed in control medium (empty blue dots), 20 ng/mL (filled orange squares), and 100 ng/mL VEGF-A (filled blue dots). **C** Wound closure rate for the same experiments as in **B**. **D** Scatter plot of half the initial gap size ($\text{gap}/2$) as a function of the time to reduce the gap to half of its initial value ($t_{1/2}$) obtained for each field of view of different experiments performed in control medium, 20 ng/mL, and 100 ng/mL VEGF-A. Lines represent the result of linear regression with an intercept equal to 0, providing the following slopes (mean \pm s.e.) and p -values (t -test): (24.3 \pm 0.7) $\mu\text{m}/\text{h}$ for the control of 20 ng/mL VEGF-A ($p < 0.001$), (22.5 \pm 0.5) $\mu\text{m}/\text{h}$ for 20 ng/mL VEGF-A ($p < 0.001$), (24.0 \pm 0.6) $\mu\text{m}/\text{h}$ for the control of 100 ng/mL VEGF-A ($p < 0.001$), (17.9 \pm 0.9) $\mu\text{m}/\text{h}$ for the 100 ng/mL VEGF-A ($p < 0.001$). **E** Boxplot of the $\text{rate}_{1/2}$ obtained for each field of view of different experiments performed in control medium, 20 ng/mL, and 100 ng/mL VEGF-A. The meaning of the symbols is the same as in **D**. Data in **D-E** correspond to 2 (20 ng/mL VEGF-A) and 3 biological replicates (100 ng/mL VEGF-A). Differences were assessed through a one-tail Wilcoxon test ($\therefore p < 0.1$, $*$: $p < 0.05$, $**$: $p < 0.01$).

These experiments were performed on cells of the unperturbed monolayer (Figure 4A), at the wound margin (Figure 4B), or isolated (Figure 4C). RIC images were used to select regions of interest for tracking and thus exclude trajectories lying outside the cell area. We used TIRF microscopy to record the motion of individual molecules sparsely labeled with half-antibody fragments conjugated with quantum dots (Figure 4D). Movies were analyzed to obtain single-molecule trajectories (Figure 4E) and quantify diffusion parameters (Figure 4F,G).

As typically observed for membrane proteins (24, 25), trajectories obtained for both receptors displayed diverse diffusion patterns (Figure 4E). In fact, membrane heterogeneity, conformational changes, and interactions with ligands and other membrane components produce different diffusion

modes that can be detected through dedicated analysis at the single-trajectory level (26). Using an algorithm based on the moment scaling spectrum (19), trajectories were classified as restrained (i.e., immobile or confined), mobile, or directed. The average MSD and the distribution of the diffusion coefficient obtained for the trajectory of each of these classes are shown in Figure 4F, G for the integrin $\alpha 5\beta 1$ in isolated fibroblasts in control medium. The probability of occurrence of directed motion was nearly negligible ($< 2\%$) in all the cases. For each class, we calculated the fraction of occurrence and the average diffusion coefficient. To compare results obtained for the two receptors in all the experimental conditions, we focused the following discussion on the quantification of trajectories classified as mobiles.

The integrin $\alpha 5\beta 1$ displayed a progressive increase in the

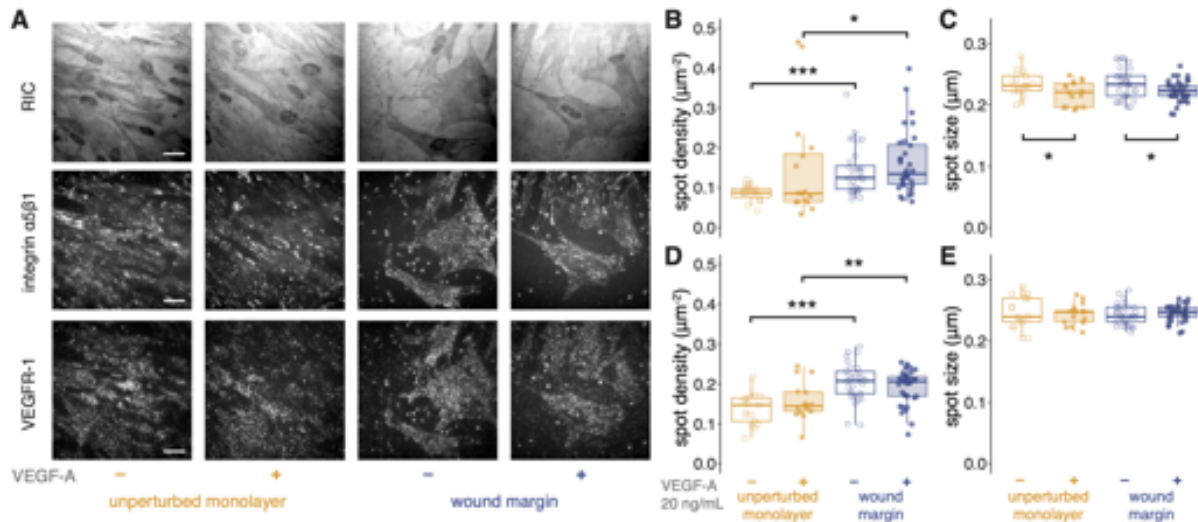


Figure 3: VEGF-A and wound influence receptors' spatial organization. **A** Reflection interference contrast (RIC, upper panels) and total internal reflection fluorescence (TIRF) imaging of the integrin $\alpha5\beta1$ (middle panels) and VEGFR-1 (lower panels) in cells of the unperturbed monolayer and the wound margin, either in control conditions or treated with 20 ng/mL VEGF-A. Bright spots outside the cell areas correspond to fiducial markers used for channel overlay. Scale bar: 20 μm ; **B-E** Boxplot corresponding to the quantification of the images described in **A**, reporting the spot density (**B**, **D**) and the median spots size (**C**, **E**) measured for the integrin $\alpha5\beta1$ (**B**, **C**) and VEGFR-1 (**D**, **E**) on different cells. Data correspond to 17 to 34 cells for each condition out of 3 technical replicates. Differences were assessed through a one-tail Wilcoxon test (*: $p < 0.05$, **: $p < 0.01$, ***: $p < 0.001$).

probability of undergoing mobile motion when the cell density was reduced. The mobile probability measured for cells of the unperturbed monolayer was $\approx 10\%$ and increased for cells at the wound margin ($\approx 15\%$) and isolated ($\approx 30\%$, Figure 4H). VEGF-A did not produce significant changes in the mobile probability. The average diffusion coefficient of the mobile fraction (Figure 4I) showed similar values ($\approx 0.15 \mu\text{m}^2/\text{s}$) across all conditions, except for a small (non-significant) increase observed at the wound margin without treatment.

Surprisingly, most of the trajectories obtained for VEGFR-1 were found compatible with receptor immobilization or confinement. In all the conditions, the mobile population had a probability $\lesssim 15\%$ and an average diffusion coefficient in the range of 0.1-0.2 $\mu\text{m}^2/\text{s}$. For VEGFR-1, the treatment with VEGF-A (Figure 4L) produced small changes in the mobile fraction that correlated with those observed for cell migration. VEGF-A nearly doubled the mobile fraction of VEGFR-1 for fibroblasts in the unperturbed monolayer and at the wound margin and produced a minor decrease in isolated cells. The average diffusion coefficient was found to be insensitive to VEGF-A but was significantly higher at the wound margin and for isolated cells with respect to the unperturbed monolayer (Figure 4M).

DISCUSSION

Several studies have reported an increased migration induced by VEGF in endothelial cells (27, 28). However, the literature investigating this effect in dermal fibroblasts is surprisingly poor, in particular, if one considers the essential roles that these cells play in cutaneous wound repair and angiogenesis (29).

As schematically depicted in Figure 5, our experiments reveal a complex interplay of VEGF-A with the signaling

machinery, involving cell activation and with subtle effects on the molecular spatiotemporal organization.

For sparse fibroblasts, we found that VEGF-A increases the migration speed while decreasing the directional persistence, with a complex temporal pattern. A similar effect was observed for epidermal growth factor (30) and, qualitatively, it is in line with results obtained in monocytes and endothelial cells (31). Persistent cell motility has been linked to the activation of the transcriptional coactivators Yes-associated protein (YAP) and transcriptional coactivator with PDZ-binding motif (TAZ) by limiting FA maturation (32).

Interestingly, this effect was reversed for the collective migration of fibroblasts. The wound healing assays showed that VEGF-A produces a slower collective migration, although with a small effect size.

Fibroblasts migrating *in vitro* have been shown to have different speeds and morphology when compared to single fibroblasts in cell culture (33). It has been also shown that confluent endothelial cells have a reduced capacity to respond to specific growth factors as compared with sparse cells (34, 35). Nevertheless, the comparison between the two situations offered hints about the interplay between VEGF-A and the signaling mechanisms involved in cell locomotion. In both situations, cells are influenced by the biochemical and physical properties of their surroundings and use similar mechanisms to adhere to the surrounding matrix and protrude (36). However, while individual migration mostly relies on interactions with the extracellular matrix, during collective migration cells influence each other's behavior through cell-cell contacts (33).

A similar effect was observed for epidermal growth factor (30) and, qualitatively, it is in line with results obtained in monocytes and endothelial cells (31).

In wound healing assays, cells are grown at a high conflu-

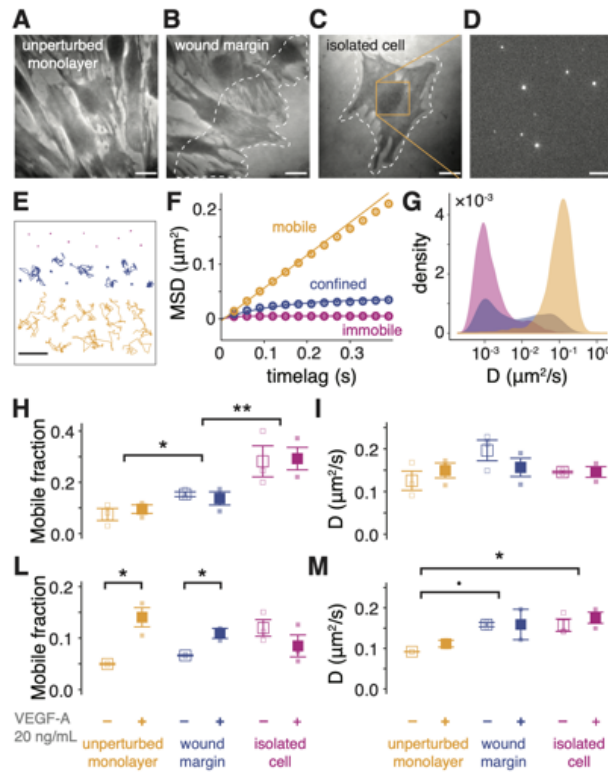


Figure 4: VEGF-A treatment and cell arrangement influence the lateral diffusion of membrane receptors. **A-C** Reflection interference contrast (RIC) images of dermal fibroblasts in the different cell arrangements used for the live-cell single-molecule imaging experiments, i.e., the unperturbed monolayer (**A**), the wound margin (**B**), and isolated cells (**C**). The images were used to draw regions of interest (dashed lines) and track molecules lying within these areas. Scale bar = 20 μm . **D** Zoomed-in region of a frame of a single-molecule imaging experiment, showing sparse quantum dots labeling the molecule of interest. Scale bar = 5 μm . **E** Representative trajectories of the same duration (3 s) obtained for the integrin $\alpha 5\beta 1$ displaying different diffusion patterns. Scale bar = 1 μm . **F-G** Ensemble averaged mean-squared displacement (**F**) and probability density of the diffusion coefficient of individual trajectory (**G**) of the integrin $\alpha 5\beta 1$ in isolated fibroblasts in control medium. The colors in **E-F** indicate trajectories classified as immobile (violet), confined (blue), and mobile (orange). **H-M** Fraction (**H, L**) and diffusion coefficient (**I, M**) of the mobile trajectories of the integrin $\alpha 5\beta 1$ (**H, I**) and VEGFR-1 (**L, M**) in all the experimental conditions. Small symbols correspond to the results of individual biological replicates. Large symbols correspond to averages over biological replicates, error bars represent standard error of the mean. Data correspond to at least 30 cells and 2000 trajectories for each biological replicate. Differences were assessed through a one-tail Wilcoxon test ($\therefore p < 0.1$, $*$: $p < 0.05$, $**$: $p < 0.01$).

ence and low serum concentration. In these conditions, direct contact between cells activates the Hippo pathway and leads to the inactivation of YAP and TAZ to maintain cell quiescence (37–39). Similarly as in tissue injury (40), wounding of *in vitro* cultured cells activates YAP, which drives cell migration to promote wound healing (41–43). YAP/TAZ can enhance the assembly of FA complexes by directly promoting the transcription of integrins and FAs docking proteins (44).

Mechanical and biochemical stress can also activate fibroblasts to become myofibroblasts through an intermediate step in which they show a proto-myofibroblast phenotype (45). The intermediate phenotype is characterized by increased contractility, more bundles of actin-myosin stress fibers, and more prominent FA structures, accompanied by clustering of integrins (46) in a process that is driven by Rho GTPase (47). YAP/TAZ also promote myofibroblast differentiation, increased matrix remodeling potential (48), and contribute to the maintenance of a synthetic and contractile phenotype (49). For cardiac fibroblasts, inactivation of the Hippo signaling has been shown to produce the sponta-

neous transition toward myofibroblast (50, 51). Myofibroblast YAP/TAZ have critical importance in driving progressive scarring in the kidney, lung, and liver (52).

Along this line, Our experiments suggest that the different behavior observed for the two conditions could be related to the YAP/TAZ activation and/or to the fibroblast to proto-myofibroblasts transition produced by cell scratching.

YAP/TAZ also has a role in mediating VEGF signaling. VEGF signaling impacts Rho family GTPase activity and cytoskeletal dynamics, which contribute to YAP/TAZ activation, and YAP/TAZ-mediated transcriptional changes sustain Rho family GTPase activity and cytoskeletal dynamics to impact vascular growth and remodeling in endothelial cells (53, 54). The presence of growth factors influences the phenotype transition from fibroblast to myofibroblast (55), but how it affects proto-myofibroblast maturation is currently unclear (56). Recently, studies of the effect of platelet-rich plasma on growth factor-induced differentiation of fibroblasts into myofibroblasts showed that the fibroblast-myofibroblast transition is negatively regulated via VEGF-A/VEGFR-1 to

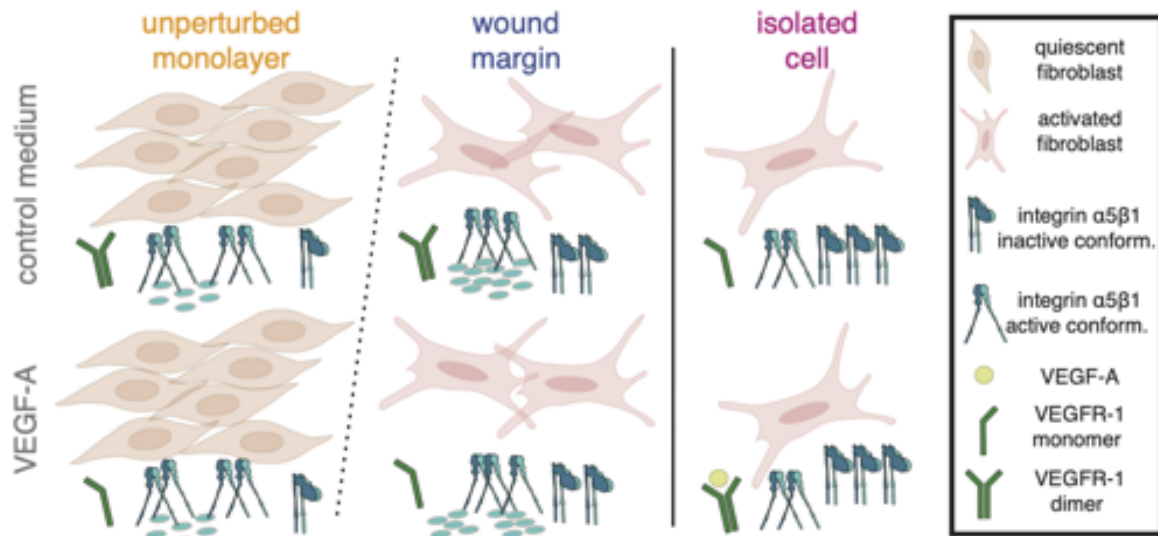


Figure 5: **Schematic of the experimental results.** VEGF-A differentially influences fibroblast migration depending on cell density and activation through changes of receptor spatiotemporal organization. At high cell density, cells show elongated shapes consistent with a quiescent fibroblast phenotype. Upon wounding, their shape is consistent with an activated fibroblast phenotype, similar to the one observed for proto-myofibroblast. Cells at the wound margin and isolated show different migration properties and receptor spatiotemporal organization as a consequence of VEGF-A treatment, pointing toward a complex interplay between different signaling pathways.

attenuate the myofibroblast phenotype (57).

A partial switch of primary human fibroblasts to a myofibroblast-like phenotype has been observed also under common culture conditions (58). Moreover, the scratching of the cell monolayer activates several mechanisms that can contribute to the shift of quiescent fibroblasts into pre-activated proto-myofibroblasts, such as the increase in intracellular calcium (59). In this scenario, the reduced wound healing rate observed for the collective migration of fibroblasts (Figure 2B-E) in the presence of VEGF-A could be associated to the attenuation of fibroblasts' differentiation into proto-myofibroblasts. While in control medium, the biochemical and mechanical stress induce by starvation and wounding induce the migratory phenotype, this effect is reduced in treated cells by VEGF-A/VEGFR-mediated antifibrotic pathway (57).

The imaging experiments shown in Figure 3 further support this hypothesis. The RIC images show a marked change of phenotype between the unperturbed monolayer and the wound margin. Fluorescence imaging further displays a corresponding increase of receptor density for both the integrin $\alpha 5\beta 1$ and VEGFR-1. Integrin $\beta 1$ expression has been strongly linked to fibroblast differentiation (60–62) and found to be upregulated in myofibroblasts through YAP/TAZ-mediated signaling (63). At low cell density, cells have a higher numbers of FAs and associated stress fibers (64).

Moreover, the presence of VEGF-A produces a reduction in integrin clustering, one of the steps for the acquisition of the proto-myofibroblast phenotype (46). While this finding is consistent with the attenuation of the myofibroblast phenotype induced by the VEGF-A treatment (57), it might also involve the VEGF-induced recycling of the integrin $\alpha 5\beta 1$ (65). Emerging evidence suggests an active role of VEGFR-1 in cell migration (6). The increase of VEGFR-1 density at the basal membrane could be associated with receptor overexpression

triggered by the increase of intracellular calcium ensuing cell damage (66). On the other hand, it could also be explained as a consequence of the redistribution of membrane receptors involved in cell-cell contacts ensuing monolayer scratching, as reported for VEGFR-2 (35).

Several studies have previously investigated the diffusion of the $\alpha 5\beta 1$ and other $\beta 1$ integrins in living cells, with overall results in line with our experiments on untreated sparse cells (67, 68). Integrin mobility has been often used as a proxy for inferring the conformational state and/or interactions with ligands and the actin cytoskeleton (69). Our experiments (Figure 4) indicate a major difference in the fraction of mobile integrins between sparse cells and monolayers and no significant effect of VEGF-A. In particular, quiescent fibroblasts in the unperturbed monolayer only have a minor fraction of mobile integrins, which is increased upon the activation of the migratory phenotype. These results can be interpreted according to the differences in mobile fraction induced by integrin activation (69) and location inside or outside FA (68). According to this view, integrins in cell monolayers are mostly immobilized in an extended conformation and engaged with the actin cytoskeleton. This fraction significantly decreases in combination with the formation of FAs observed at the wound margin. Individual fibroblasts display a further increase of the mobile fraction that can be associated with integrins free or transiently localized in nascent adhesions during adhesion turnover (23).

To the best of our knowledge, the lateral diffusion of VEGFR-1 at the single-molecule level has not been reported earlier. We found VEGFR-1 to be mainly immobile or confined, as reported for other growth factors (24). The small mobile component showed a diffusion coefficient similar to the one measured for VEGFR-2 (70). The increase of VEGFR-1 mobility upon VEGF-A treatment is rather counter-intuitive as

one would have expected an increase of receptor dimerization under the presence of its ligand, with a consequent reduction of mobility (70). A possible explanation might involve a change in VEGFR-2 dimerization constant upon VEGF-A binding, converting VEGFR-1 involved in heterodimers in resting conditions into monomers (5, 71). However, this hypothesis is challenged by the fact that several studies reported that VEGFR-2 is not expressed in fibroblasts (72, 73). Changes in the receptor diffusion coefficient in confluent cells might instead be generally associated with cell density-dependent phenomenon regulating the activity of growth factor receptors as, e.g., observed for VEGFR-2 (74) but the understanding of the exact mechanism needs further study.

CONCLUSION

Our experiments and analyses demonstrate a complex relationship between receptors' interactions, molecular organization, and mobility that determine fibroblasts' behavior in migration and wound healing. Our data further hint that these mechanisms are modulated by other factors, such as cell density, differentiation, and signaling ensuing cell damage. The comparison of experiments performed in different cellular arrangements strongly suggests the involvement of the Hippo pathway and of the fibroblast to proto-myofibroblasts transition in controlling cellular and molecular behavior. Overall, these results highlight the need to perform multiscale studies, investigating receptors at the nanoscopic level in their native cellular environment and linking them to cellular outcomes, thus bridging the gap between the molecular, cellular, and multicellular scales.

AUTHOR CONTRIBUTIONS

CM and MC-D designed the research. MC-D, MM, and JB performed the experiments. CM and MC-D analyzed the data and wrote the article with contributions from all the authors. CM and MO-V supervised the research.

ACKNOWLEDGMENTS

MO-V acknowledges support of the PO FEDER of Catalonia 2014–2020 (project PECT Osona Transformació Social, Ref. 001-P-000382), and the Spanish Ministry of Science, Innovation, and Universities through the Instituto de Salud Carlos III-FEDER program (FIS PI19/01379). CM acknowledges support through grant RYC-2015-17896 funded by MCIN/AEI/10.13039/501100011033 and “ESF Investing in your future”, grants BFU2017-85693-R and PID2021-125386NB-I00 funded by MCIN/AEI/10.13039/501100011033/ and FEDER “ERDF A way of making Europe”, and grant AGAUR 2017SGR940 funded by the Generalitat de Catalunya. CM also acknowledges the support of NVIDIA Corporation with the donation of the Titan Xp GPU.

REFERENCES

- Gurtner, G. C., S. Werner, Y. Barrandon, and M. T. Longaker, 2008. Wound repair and regeneration. *Nature* 453:314–321.
- Darby, I. A., B. Laverdet, F. Bonté, and A. Desmoulière, 2014. Fibroblasts and myofibroblasts in wound healing. *Clinical, cosmetic and investigational dermatology* 301–311.
- Bao, P., A. Kodra, M. Tomic-Canic, M. S. Golinko, H. P. Ehrlich, and H. Brem, 2009. The role of vascular endothelial growth factor in wound healing. *Journal of Surgical Research* 153:347–358.
- Shibuya, M., 2006. Vascular endothelial growth factor receptor-1 (VEGFR-1/Flt-1): a dual regulator for angiogenesis. *Angiogenesis* 9:225–230.
- Cudmore, M. J., P. W. Hewett, S. Ahmad, K.-Q. Wang, M. Cai, B. Al-Ani, T. Fujisawa, B. Ma, S. Sissaoui, W. Ramma, et al., 2012. The role of heterodimerization between VEGFR-1 and VEGFR-2 in the regulation of endothelial cell homeostasis. *Nature communications* 3:972.
- Weddell, J. C., S. Chen, and P. Imoukhuede, 2017. VEGFR1 promotes cell migration and proliferation through PLC γ and PI3K pathways. *NPJ systems biology and applications* 4:1.
- Lubkowska, A., B. Dolegowska, G. Banfi, et al., 2012. Growth factor content in PRP and their applicability in medicine. *J Biol Regul Homeost Agents* 26:3S–22S.
- Byzova, T. V., C. K. Goldman, N. Pampori, K. A. Thomas, A. Bett, S. J. Shattil, and E. F. Plow, 2000. A mechanism for modulation of cellular responses to VEGF: activation of the integrins. *Molecular cell* 6:851–860.
- De, S., O. Razorenova, N. P. McCabe, T. O'Toole, J. Qin, and T. V. Byzova, 2005. VEGF–integrin interplay controls tumor growth and vascularization. *Proceedings of the National Academy of Sciences* 102:7589–7594.
- Somanath, P. R., A. Ciocea, and T. V. Byzova, 2009. Integrin and growth factor receptor alliance in angiogenesis. *Cell biochemistry and biophysics* 53:53–64.
- Kanchanawong, P., and D. A. Calderwood, 2022. Organization, dynamics and mechanoregulation of integrin-mediated cell–ECM adhesions. *Nature Reviews Molecular Cell Biology* 1–20.
- Hanft, J. R., R. A. Pollak, A. Barbul, C. van Gils, P. S. Kwon, S. M. Gray, C. J. Lynch, C. P. Semba, and T. J. Breen, 2013. Phase I trial on the safety of topical rhVEGF on chronic neuropathic diabetic foot ulcers@articlevinals1999confluence, title=Confluence of vascular endothelial cells induces cell cycle exit by inhibiting p42/p44 mitogen-activated protein kinase activity, author=Viñals, Francesc and Pouysségur, Jacques, journal=Molecular and cellular biology, volume=19, number=4, pages=2763–2772, year=1999, publisher=Am Soc Microbiol . <https://doi.org/10.12968/jowc.2008.17.1.27917> 17. <https://www.magonlineibrary.com/doi/10.12968/jowc.2008.17.1.27917>.

13. Low-Nam, S. T., K. A. Lidke, P. J. Cutler, R. C. Roovers, P. M. van Bergen en Henegouwen, B. S. Wilson, and D. S. Lidke, 2011. ErbB1 dimerization is promoted by domain co-confinement and stabilized by ligand binding. *Nature Structural & Molecular Biology* 18:1244–1249.
14. Tinevez, J. Y., N. Perry, J. Schindelin, G. M. Hoopes, G. D. Reynolds, E. Laplantine, S. Y. Bednarek, S. L. Shorte, and K. W. Eliceiri, 2017. TrackMate: An open and extensible platform for single-particle tracking. *Methods* 115:80–90. <https://www.sciencedirect.com/science/article/pii/S1046202316303346>.
15. Vargas, A., M. Angeli, C. Pastrello, R. Mcquaid, H. Li, A. Jurisicova, and I. Jurisica, 2016. Robust quantitative scratch assay. *Bioinformatics* 32:1439–1440. <https://academic.oup.com/bioinformatics/article/32/9/1439/1743750>.
16. Bobadilla, A. V. P., J. Arévalo, E. Sarró, H. M. Byrne, P. K. Maini, T. Carraro, S. Balocco, A. Meseguer, and T. Alarcón, 2019. In vitro cell migration quantification method for scratch assays. *Journal of the Royal Society Interface* 16:20180709.
17. Horzum, U., B. Ozdil, and D. Pesen-Okvur, 2014. Step-by-step quantitative analysis of focal adhesions. *MethodsX* 1:56–59.
18. Jaqaman, K., D. Loerke, M. Mettlen, H. Kuwata, S. Grinstein, S. L. Schmid, and G. Danuser, 2008. Robust single-particle tracking in live-cell time-lapse sequences. *Nature Methods* 5:695–702. <http://www.nature.com/naturemethods>.
19. Vega, A. R., S. A. Freeman, S. Grinstein, and K. Jaqaman, 2018. Multistep track segmentation and motion classification for transient mobility analysis. *Biophysical Journal* 114:1018–1025.
20. Czirók, A., K. Schlett, E. Madarász, and T. Vicsek, 1998. Exponential Distribution of Locomotion Activity in Cell Cultures. *Physical Review Letters* 81:3038. <https://journals.aps.org/prl/abstract/10.1103/PhysRevLett.81.3038>.
21. García, A. J., and D. Boettiger, 1999. Integrin–fibronectin interactions at the cell-material interface: initial integrin binding and signaling. *Biomaterials* 20:2427–2433.
22. Ferrara, N., H. P. Gerber, and J. LeCouter, 2003. The biology of VEGF and its receptors. *Nature Medicine* 9:669–676. <https://www.nature.com/articles/nm0603-669>.
23. Chastney, M. R., J. R. Conway, and J. Ivaska, 2021. Integrin adhesion complexes. *Current Biology* 31:R536–R542.
24. Kusumi, A., Y. Sako, and M. Yamamoto, 1993. Confined lateral diffusion of membrane receptors as studied by single particle tracking (nanovid microscopy). Effects of calcium-induced differentiation in cultured epithelial cells. *Biophysical Journal* 65:2021–2040.
25. Manzo, C., and M. F. Garcia-Parajo, 2015. A review of progress in single particle tracking: from methods to biophysical insights. *Reports on progress in physics* 78:124601.
26. Muñoz-Gil, G., G. Volpe, M. A. Garcia-March, E. Aghion, A. Argun, C. B. Hong, T. Bland, S. Bo, J. A. Conejero, N. Firbas, et al., 2021. Objective comparison of methods to decode anomalous diffusion. *Nature communications* 12:6253.
27. Favot, L., T. Keravis, V. Holl, A. Le Bec, and C. Lugnier, 2003. VEGF-induced HUVEC migration and proliferation are decreased by PDE2 and PDE4 inhibitors. *Thrombosis and Haemostasis* 90:334–343. <http://www.thieme-connect.com/products/ejournals/html/10.1160/TH03-02-0084http://www.thieme-connect.de/DOI/DOI?10.1160/TH03-02-0084>.
28. Deissler, H., S. Lang, and G. E. Lang, 2008. VEGF-induced effects on proliferation, migration and tight junctions are restored by ranibizumab (Lucentis) in microvascular retinal endothelial cells. *British journal of ophthalmology* 92:839–843.
29. Li, W., J. Fan, M. Chen, S. Guan, D. Sawcer, G. M. Bokoch, and D. T. Woodley, 2004. Mechanism of Human Dermal Fibroblast Migration Driven by Type I Collagen and Platelet-derived Growth Factor-BB. *Molecular Biology of the Cell* 15:294–309. <https://www.molbiolcell.org/doi/10.1091/mbc.e03-05-0352>.
30. Ware, M. F., A. Wells, and D. A. Lauffenburger, 1998. Epidermal growth factor alters fibroblast migration speed and directional persistence reciprocally and in a matrix-dependent manner. *Journal of cell science* 111:2423–2432.
31. Kliche, S., and J. Waltenberger, 2001. VEGF receptor signaling and endothelial function. *IUBMB life* 52:61–66.
32. Mason, D. E., J. M. Collins, J. H. Dawahare, T. D. Nguyen, Y. Lin, S. L. Voytik-Harbin, P. Zorlutuna, M. C. Yoder, and J. D. Boerckel, 2019. YAP and TAZ limit cytoskeletal and focal adhesion maturation to enable persistent cell motility. *Journal of Cell Biology* 218:1369–1389.
33. Trepatt, X., Z. Chen, and K. Jacobson, 2012. Cell migration. *Comprehensive Physiology* 2:2369.
34. Viñals, F., and J. Pouyssegur, 1999. Confluence of Vascular Endothelial Cells Induces Cell Cycle Exit by Inhibiting p42/p44 Mitogen-Activated Protein Kinase Activity. *Molecular and Cellular Biology* 19:2763–2772. <https://journals.asm.org/doi/10.1128/MCB.19.4.2763>.
35. Lampugnani, M. G., A. Zanetti, M. Corada, T. Takahashi, G. Balconi, F. Breviario, F. Orsenigo, A. Cattellino, R. Kemler, T. O. Daniel, and E. Dejana, 2003. Contact inhibition of VEGF-induced proliferation requires

- vascular endothelial cadherin, β -catenin, and the phosphatase DEP-1/CD148. *Journal of Cell Biology* 161:793–804. <http://www.jcb.org/cgi/doi/10.1083/jcb.200209019>.
36. De Pascalis, C., and S. Etienne-Manneville, 2017. Single and collective cell migration: the mechanics of adhesions. *Molecular biology of the cell* 28:1833–1846.
 37. Zhou, D., C. Conrad, F. Xia, J. S. Park, B. Payer, Y. Yin, G. Y. Lauwers, W. Thasler, J. T. Lee, J. Avruch, and N. Bardeesy, 2009. Mst1 and Mst2 Maintain Hepatocyte Quiescence and Suppress Hepatocellular Carcinoma Development through Inactivation of the Yap1 Oncogene. *Cancer Cell* 16:425–438.
 38. Yu, F. X., B. Zhao, and K. L. Guan, 2015. Hippo Pathway in Organ Size Control, Tissue Homeostasis, and Cancer. *Cell* 163:811–828.
 39. Pavel, M., M. Renna, S. J. Park, F. M. Menzies, T. Ricketts, J. Füllgrabe, A. Ashkenazi, R. A. Frake, A. C. Lombarte, C. F. Bento, K. Franze, and D. C. Rubinsztein, 2018. Contact inhibition controls cell survival and proliferation via YAP/TAZ-autophagy axis. *Nature Communications* 9:1–18. <https://www.nature.com/articles/s41467-018-05388-x>.
 40. Meng, Z., T. Moroishi, and K.-L. Guan, 2016. Mechanisms of Hippo pathway regulation. *Genes & development* 30:1–17.
 41. Zhao, B., X. Wei, W. Li, R. S. Udan, Q. Yang, J. Kim, J. Xie, T. Ikenoue, J. Yu, L. Li, P. Zheng, K. Ye, A. Chinnaiyan, G. Halder, Z. C. Lai, and K. L. Guan, 2007. Inactivation of YAP oncoprotein by the Hippo pathway is involved in cell contact inhibition and tissue growth control. *Genes & Development* 21:2747–2761. <http://genesdev.cshlp.org/content/21/21/2747.full>.
 42. Zhao, B., Q. Y. Lei, and K. L. Guan, 2008. The Hippo–YAP pathway: new connections between regulation of organ size and cancer. *Current Opinion in Cell Biology* 20:638–646.
 43. Lee, M.-J., M. R. Byun, M. Furutani-Seiki, J.-H. Hong, and H.-S. Jung, 2014. YAP and TAZ regulate skin wound healing. *Journal of Investigative Dermatology* 134:518–525.
 44. Nardone, G., J. Oliver-De La Cruz, J. Vrbsky, C. Martini, J. Pribyl, P. Skládál, M. Pešl, G. Caluori, S. Pagliari, F. Martino, et al., 2017. YAP regulates cell mechanics by controlling focal adhesion assembly. *Nature communications* 8:15321.
 45. D'Urso, M., and N. A. Kurniawan, 2020. Mechanical and physical regulation of fibroblast–myofibroblast transition: from cellular mechanoreponse to tissue pathology. *Frontiers in bioengineering and biotechnology* 8:609653.
 46. Van De Water, L., S. Varney, and J. J. Tomasek, 2013. Mechanoregulation of the myofibroblast in wound contraction, scarring, and fibrosis: opportunities for new therapeutic intervention. *Advances in wound care* 2:122–141.
 47. Chrzanowska-Wodnicka, M., and K. Burridge, 1996. Rho-stimulated contractility drives the formation of stress fibers and focal adhesions. *The Journal of cell biology* 133:1403–1415.
 48. Dey, A., X. Varelas, and K.-L. Guan, 2020. Targeting the Hippo pathway in cancer, fibrosis, wound healing and regenerative medicine. *Nature reviews Drug discovery* 19:480–494.
 49. Piersma, B., S. de Rond, P. M. Werker, S. Boo, B. Hinz, M. M. van Beuge, and R. A. Bank, 2015. YAP1 is a driver of myofibroblast differentiation in normal and diseased fibroblasts. *The American journal of pathology* 185:3326–3337.
 50. Johansen, A. K. Z., and J. D. Molkentin, 2019. Hippo signaling does it again: arbitrating cardiac fibroblast identity and activation. *Genes & development* 33:1457–1459.
 51. Xiao, Y., M. C. Hill, L. Li, V. Deshmukh, T. J. Martin, J. Wang, and J. F. Martin, 2019. Hippo pathway deletion in adult resting cardiac fibroblasts initiates a cell state transition with spontaneous and self-sustaining fibrosis. *Genes & Development* 33:1491–1505.
 52. He, X., M. F. Tolosa, T. Zhang, S. K. Goru, L. U. Severino, P. S. Misra, C. M. McEvoy, L. Caldwell, S. G. Szeto, F. Gao, et al., 2022. Myofibroblast YAP/TAZ activation is a key step in organ fibrogenesis. *JCI insight* 7.
 53. Elaimy, A. L., and A. M. Mercurio, 2018. Convergence of VEGF and YAP/TAZ signaling: Implications for angiogenesis and cancer biology. *Science Signaling* 11:eaau1165.
 54. Totaro, A., T. Panciera, and S. Piccolo, 2018. YAP/TAZ upstream signals and downstream responses. *Nature cell biology* 20:888–899.
 55. Balza, E., L. Borsi, G. Allemanni, and L. Zardi, 1988. Transforming growth factor β regulates the levels of different fibronectin isoforms in normal human cultured fibroblasts. *FEBS letters* 228:42–44.
 56. Klingberg, F., B. Hinz, and E. S. White, 2013. The myofibroblast matrix: implications for tissue repair and fibrosis. *The Journal of pathology* 229:298–309.
 57. Chellini, F., A. Tani, L. Vallone, D. Nosi, P. Pavan, F. Bambi, S. Zecchi Orlandini, and C. Sassoli, 2018. Platelet-rich plasma prevents in vitro transforming growth factor- β 1-induced fibroblast to myofibroblast transition: involvement of vascular endothelial growth factor (VEGF)-A/VEGF receptor-1-mediated signaling. *Cells* 7:142.
 58. Baranyi, U., B. Winter, A. Gugerell, B. Hegedus, C. Brostjan, G. Laufer, and B. Messner, 2019. Primary human fibroblasts in culture switch to a myofibroblast-like phenotype independently of TGF beta. *Cells* 8:721.

59. Zhang, B., J. Jiang, Z. Yue, S. Liu, Y. Ma, N. Yu, Y. Gao, S. Sun, S. Chen, and P. Liu, 2016. Store-Operated Ca²⁺ Entry (SOCE) contributes to angiotensin II-induced cardiac fibrosis in cardiac fibroblasts. *Journal of Pharmacological Sciences* 132:171–180. <https://www.sciencedirect.com/science/article/pii/S1347861316300603>.
60. Shochet, G. E., E. Brook, B. Bardenstein-Wald, H. Grobe, E. Edelstein, L. Israeli-Shani, and D. Shitrit, 2020. Integrin alpha-5 silencing leads to myofibroblastic differentiation in IPF-derived human lung fibroblasts. *Therapeutic Advances in Chronic Disease* 11:2040622320936023.
61. Norman, J. T., and L. G. Fine, 1999. Progressive renal disease: fibroblasts, extracellular matrix, and integrins. *Nephron Experimental Nephrology* 7:167–177.
62. White, L. R., J. B. Blanchette, L. Ren, A. Awn, K. Trpkov, and D. A. Muruve, 2007. The characterization of α 5-integrin expression on tubular epithelium during renal injury. *American Journal of Physiology-Renal Physiology* 292:F567–F576.
63. Martin, K., J. Pritchett, J. Llewellyn, A. F. Mullan, V. S. Athwal, R. Dobie, E. Harvey, L. Zeef, S. Farrow, C. Streuli, et al., 2016. PAK proteins and YAP-1 signalling downstream of integrin beta-1 in myofibroblasts promote liver fibrosis. *Nature communications* 7:12502.
64. Dobrokhotov, O., M. Samsonov, M. Sokabe, and H. Hirata, 2018. Mechanoregulation and pathology of YAP/TAZ via Hippo and non-Hippo mechanisms. *Clinical and translational medicine* 7:1–14.
65. Alexander, R. A., G. W. Prager, J. Mihaly-Bison, P. Uhrin, S. Sunzenauer, B. R. Binder, G. J. Schütz, M. Freissmuth, and J. M. Breuss, 2012. VEGF-induced endothelial cell migration requires urokinase receptor (uPAR)-dependent integrin redistribution. *Cardiovascular research* 94:125–135.
66. Man, X.-Y., X.-H. Yang, S.-Q. Cai, Z.-Y. Bu, and M. Zheng, 2008. Overexpression of vascular endothelial growth factor (VEGF) receptors on keratinocytes in psoriasis: regulated by calcium independent of VEGF. *Journal of cellular and molecular medicine* 12:649–660.
67. Rossier, O., V. Oceau, J.-B. Sibarita, C. Leduc, B. Tessier, D. Nair, V. Gatterdam, O. Destaing, C. Albigès-Rizo, R. Tampé, L. Cagnet, D. Choquet, B. Lounis, and G. Giannone, 2012. Integrins β 1 and β 3 exhibit distinct dynamic nanoscale organizations inside focal adhesions. *Nature Cell Biology* 14:1057–1067. <http://www.nature.com/articles/ncb2588>.
68. Orré, T., A. Joly, Z. Karatas, B. Kastberger, C. Cabriel, R. T. Böttcher, S. Lévêque-Fort, J. B. Sibarita, R. Fässler, B. Wehrle-Haller, O. Rossier, and G. Giannone, 2021. Molecular motion and tridimensional nanoscale localization of kindlin control integrin activation in focal adhesions. *Nature Communications* 12:1–17. <https://www.nature.com/articles/s41467-021-23372-w>.
69. Bakker, G. J., C. Eich, J. A. Torreno-Pina, R. Diez-Ahedo, G. Perez-Samper, T. S. van Zanten, C. G. Figdor, A. Cambi, and M. F. Garcia-Parajo, 2012. Lateral mobility of individual integrin nanoclusters orchestrates the onset for leukocyte adhesion. *Proceedings of the National Academy of Sciences* 109:4869–4874.
70. da Rocha-Azevedo, B., S. Lee, A. Dasgupta, A. R. Vega, L. R. de Oliveira, T. Kim, M. Kittisopikul, Z. A. Malik, and K. Jaqaman, 2020. Heterogeneity in VEGF Receptor-2 Mobility and Organization on the Endothelial Cell Surface Leads to Diverse Models of Activation by VEGF. *Cell Reports* 32:108187.
71. King, C., and K. Hristova, 2019. Direct measurements of VEGF–VEGFR2 binding affinities reveal the coupling between ligand binding and receptor dimerization. *Journal of Biological Chemistry* 294:9064–9075.
72. Cianfarani, F., G. Zambruno, L. Brogelli, F. Sera, P. M. Laccal, M. Pesce, M. C. Capogrossi, C. M. Failla, M. Napolitano, and T. Odorisio, 2006. Placenta Growth Factor in Diabetic Wound Healing: Altered Expression and Therapeutic Potential. *The American Journal of Pathology* 169:1167–1182.
73. Eming, S. A., B. Brachvogel, T. Odorisio, and M. Koch, 2007. Regulation of angiogenesis: Wound healing as a model. *Progress in Histochemistry and Cytochemistry* 42:115–170. <https://www.sciencedirect.com/science/article/pii/S0079633607000319>.
74. Rahimi, N., and A. Kazlauskas, 1999. A role for cadherin-5 in regulation of vascular endothelial growth factor receptor 2 activity in endothelial cells. *Molecular Biology of the Cell* 10:3401–3407.

ARTICLE 2. A toolkit for the quantitative evaluation of chronic wounds evolution for early detection of non-healing wounds

The main objective of this study was to provide physicians with a useful tool based on the analysis of wound area vs. time for the early prediction of non-healing wound evolution to support clinicians in clinical decision-making to select the appropriate therapy for chronic wounds.

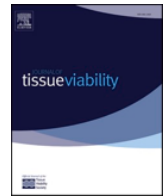
We realize that the first step to achieving this goal was to develop a method to obtain exact measures from wound planimetries. So, we developed user-friendly software (Woundaries) in Matlab to calculate the exact surface area, perimeter, and the following shape descriptors: initial wound circularity, roughness, and aspect ratio, from scanned or photographed planimetries. We supplied our software with a graphic user interface with two sliders to easily control the parameters of the image processing algorithm. Once the image is adjusted, the users can define a calibration area based on the measurement grid for unit conversion. Finally, the software shows the measures on the screen and gives the user the option to export the results to a file.

The software was tested using a validated device by comparing the area measurements of 48 different wound planimetries, resulting in non-significant differences in measurements between both methods. The repeatability and reproducibility assessments showed non-significant differences in wound quantification between different operators and good reproducibility results.

In addition, we developed another tool to determine the characteristic healing time, based on a previously reported wound healing exponential decay model. Due to the presence of a delay time at the beginning of the healing process observed in some wounds, we developed a methodology to include that situation. Our script tests for the better fit between a simple exponential behavior with 2 free parameters or a mixed

model, composed of an initial linear behavior followed by an exponential decay, with 4 free parameters in total.

Finally, our tools were tested on simulations and retrospectively applied to data from 120 wounds from 85 patients treated with biological therapy (autologous platelet plasma therapy) or with conventional therapeutics in a wound clinical unit. Our results showed a significant difference between both groups, with faster healing (lower characteristic time of healing) in wounds of patients treated with biological therapy. The therapy results analyzed by gender showed significant differences in the healing time for those patients receiving the therapy in comparison with those receiving conventional treatments. However, no statistically significant differences between both therapeutic strategies were observed in men. In addition, no significant differences were observed in healing time by patients' age, wound localization, or other health conditions. Interestingly, our results showed that traumatic wounds heal significantly faster than arterial and unclassified wounds. However, we did not find any relation between characteristic healing time and wound shape descriptors.



A toolkit for the quantitative evaluation of chronic wounds evolution for early detection of non-healing wounds

Marta Cullell-Dalmau^a, Marta Otero-Viñas^{b,c,*}, Marta Ferrer-Solà^{b,d}, Helena Sureda-Vidal^{b,d}, Carlo Manzo^a

^a The Quantitative BioImaging (QuBI) Lab, University of Vic – Central University of Catalonia (UVic-UCC), C. de La Laura, 13, 08500, Vic, Spain

^b Tissue Repair and Regeneration Laboratory (TR2Lab), University of Vic – Central University of Catalonia (UVic-UCC), Fundació Hospital Universitari de la Santa Creu de Vic, and Hospital Universitari de Vic, 08500, Vic, Spain

^c University of Vic – Central University of Catalonia, C. de La Laura, 13, 08500, Vic, Spain

^d Fundació Hospital Universitari de la Santa Creu de Vic, Rambla de l'Hospital, 52, 08500, Vic, Spain

ARTICLE INFO

Keywords:

Chronic wound
Wound healing evolution
Platelet-poor plasma
Wound area

ABSTRACT

Background: Chronic wounds resulting from a number of conditions do not heal properly and can pose serious health problems. Beyond clinician visual inspection, an objective evaluation of the wound is required to assess wound evolution and the effectiveness of therapies.

Aim: Our objective is to provide a methodology for the analysis of wound area vs. time for the early prediction of non-healing wounds evolution.

Methods: We propose a two-step approach consisting of: i) wound area quantification from planimetries and ii) classification of wound healing through the inference of characteristic parameters. For the first step, we describe a user-friendly software (Woundaries) to automatically calculate the wound area and other geometric parameters from hand-traced planimetries. For the second, we use a procedure for the objective classification of wound time evolution and the early assessment of treatment efficacy. The methodology was tested on simulations and retrospectively applied to data from 85 patients to compare the effect of a biological therapy with respect to general basic therapeutics.

Results: Woundaries provides measurements of wound surface equivalent to a validated device. The two-step methodology allows to determine if a wound is healing with high sensitivity, even with limited amount of data. Therefore, it allows the early assessment of the efficacy of a therapy.

Conclusion: The performance of this methodology for the quantification and the objective evaluation of wound area evolution suggest it as a useful toolkit to assist clinicians in the early assessment of the efficacy of treatments, leading to a timely change of therapy.

1. Introduction

The term chronic wound generally refers to an ulcer that does not progress through the normal stages of healing and often stall in the inflammatory phase [1]. Chronic wounds frequently occur in adults with vascular disease or diabetes and are generally classified as vascular ulcers, pressure ulcers (UPP), and diabetic ulcers [2]. Due to the societal and economic burden associated with chronic wounds and their increasing incidence, extensive efforts toward the development of advanced therapies, including plasma-derived products have been

deployed [3,4].

In spite of the application of advanced therapies, chronic wounds often do not respond to treatments. In these cases, an early detection of unresponsiveness, followed by wound re-assessment and change of treatment, can reduce the risk of complications and lead to an improved outcome [5]. Usually, the evolution of the wound is only assessed through visual inspection, e.g. by monitoring surface granulation and size. In this scenario, a quantitative characterization of wound geometry as a function of time can help to detect subtle variations before a visually-observable change occurs, leading to a change of therapy at an

* Corresponding author. Tissue Repair and Regeneration Laboratory (TR2Lab), University of Vic – Central University of Catalonia (UVic-UCC), C. de la Laura, 13, 08500, Vic, Spain.

E-mail address: marta.otero@uvic.cat (M. Otero-Viñas).

<https://doi.org/10.1016/j.jtv.2021.02.009>

Received 2 October 2020; Received in revised form 3 February 2021; Accepted 24 February 2021

Available online 2 March 2021

0965-206X/© 2021 The Authors. Published by Elsevier Ltd on behalf of Tissue Viability Society. This is an open access article under the CC BY license

(<http://creativecommons.org/licenses/by/4.0/>).

early stage [6]. For this reason, several approaches have been proposed for the measurement of wound size [6–11]. Among them, digital planimetry is considered a reliable and cost-effective method for area measurement, particularly in wounds with irregular shapes [6]. However, its accuracy is affected by the camera lens orientation [7,9] and by the three-dimensional curvature of the wound. When the direct contact with the wound does not constitute a matter of concern, these problems can be simply overcome by manually tracing its outline on a transparent film placed over the wound. The ensuing evaluation of the area, performed by counting the number of squares falling within the outline, makes this method error-prone and tedious [7]. More complex methods, based on 3D reconstruction, volume filling or laser scanners have also been proposed but are not routinely used due their cost or invasiveness [10,12].

Besides the measurement of the wound area, the prediction of its evolution is essential to assist clinicians in timely therapeutic decisions. This prediction can be obtained through the proper modelling of the kinetic of wound area and the inference of parameters that quantify the effect of treatments [13–17]. While the kinetic of wound area has been extensively described and approximated by means of nonlinear models [13–15,17], the number of attempts aimed at using size and shape information to predict wound evolution have been so far rather limited [16]. Recently, methods based on artificial intelligence have shown outstanding results but they still require further validation before being accepted for routine clinical uses [18].

In this work, we describe and validate a simple toolkit for the measurement and quantitative evaluation of wounds evolution. We further apply it to a set of clinical data from patients with chronic wounds treated with different therapies. In addition, we assess its capability for the early detection of unresponsive wounds, with the objective to

support professionals in clinical decision making.

2. Methods

2.1. Wound area and shape quantification

At each weekly visit, after wound cleaning, wounds were photographed with a digital camera (Fig. 1A). Thus, a sterile transparent adhesive film with a measurement grid (1 cm pace; OpSite flexigrid, Smith & Nephew) was placed over the wound and the wound margin was directly traced, obtaining the wound planimetry (Fig. 1B). All the clinical procedures used were in accordance with the institutional guidelines and were approved by the ethics committee of the hospital. Patients gave written informed consent.

The wound margin was digitalized through either a scanner or a digital camera and processed using a custom software named Woundaries (freely available on the github repository <https://github.com/qubilab/woundaries>) written in Matlab (The MathWorks, Inc., Natick, Massachusetts, United States) to calculate the surface area, perimeter, and several other shape descriptors. The software consists in a graphic user interface (Fig. 1C) that allows the upload and the visualization of the digitalized planimetry and the selection of the area of interest. The user can adjust two sliders controlling the values of parameters of the image processing algorithm. The first slider controls a threshold value used to transform the image in a black and white map, and it is aimed at removing the grid texture from the image, while highlighting the wound planimetry. In the case of a not completely closed planimetry, the second slider can be used to join gaps in the wound boundary by an edge linking function [19]. The steps of the image processing algorithm are visualized and updated at each sliders' movement, together with the overlay

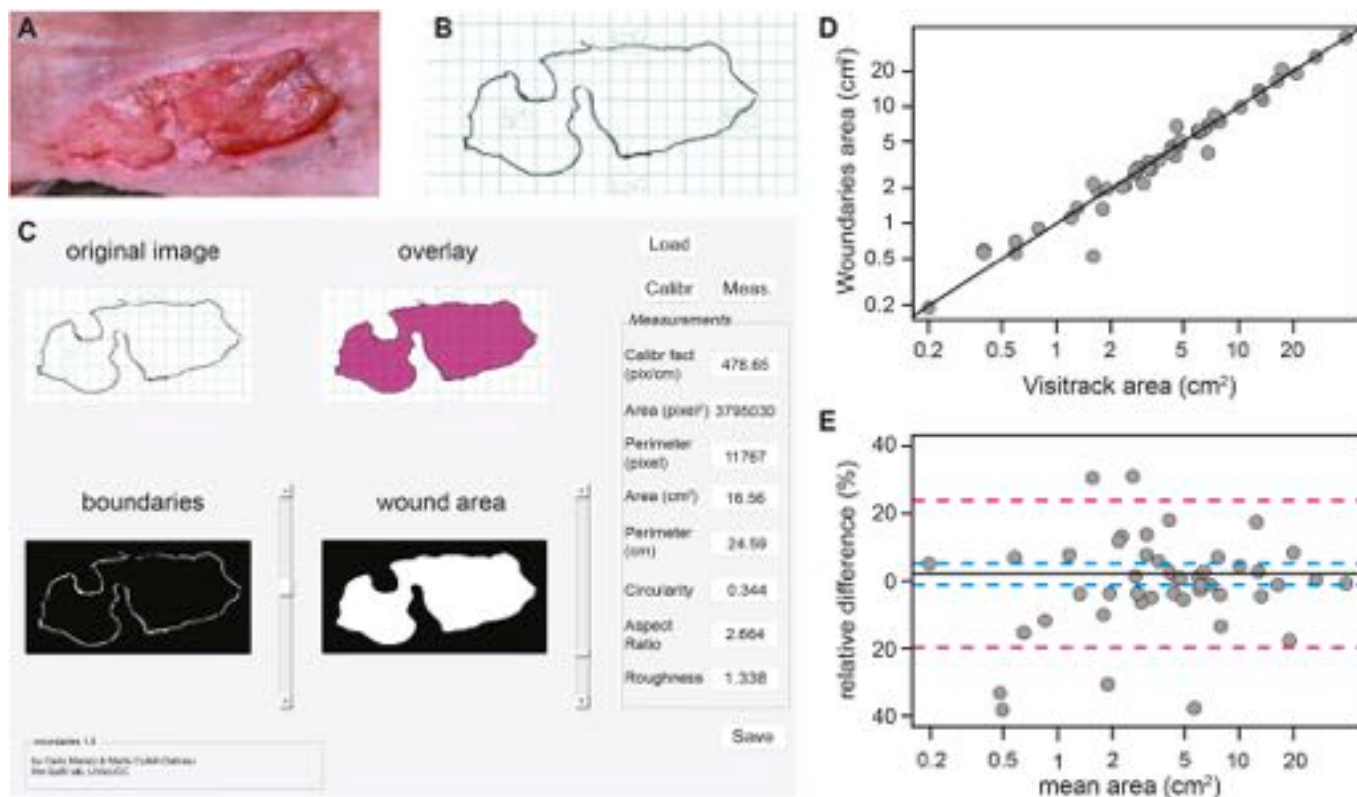
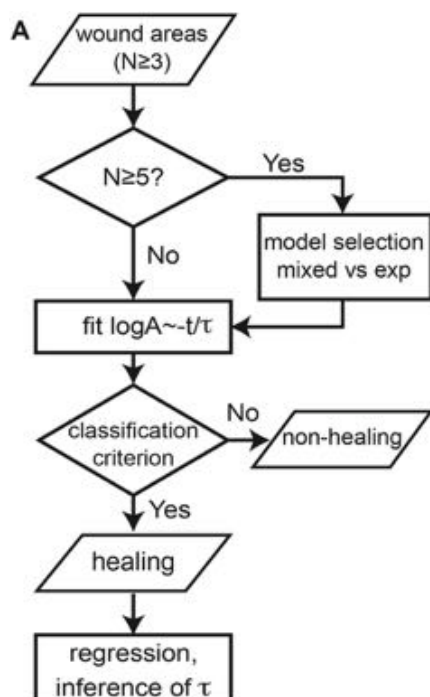


Fig. 1. Schematic and performance of the Woundaries software. (A) A digital photograph of a representative wound and (B) the corresponding planimetry. (C) Screenshot of the Woundaries software during the quantification of the wound represented in panels A–B. (D–E) Comparison of the quantification of 23 representative wounds performed by means of Woundaries and Visitrack. (D) A log-log scatter plot of the data (circles) and a straight line with unitary slope and null intercept, used as a visual reference. (E) A Bland–Altman semilog plot of the percentage of relative difference between the two methods of measurement (circles). Continuous black line corresponds to the mean difference. Dashed blue lines correspond to the standard error of the mean and dashed magenta lines to the standard error. (For interpretation of the references to colour in this figure legend, the reader is referred to the Web version of this article.)

of the original planimetry with the wound area (Fig. 1C). Once the adjustment of the parameters produces a closed contour faithfully matching the planimetry outline and completely filled (Fig. 1C), then the “Measure” button enables the calculation of wound area, shape and other geometry descriptors. The software allows users to define a calibration area based on the measurement grid for unit conversion. By means of this calibration, the unknown area of a pixel can be calculated and thus the total number of pixels (and their fractions) contained within the contour are converted into area units. All the measurements can be saved in a text file for further analysis.

To validate our method, area measurements obtained for a subset of planimetries with different shapes and sizes were measured with Woundaries (by the same operator) and with a previously-validated device (Visitrak, Smith & Nephew, United Kingdom, measurements were performed by two members of the sanitary staff of the hospital) [7]. The subset was composed by 48 wounds (mean area = 6.32 cm², median area = 3.87 cm², IQR = 5.05 cm², minimum area = 0.19 cm², maximum area = 39.17 cm²). The equivalence of both measurements was assessed through a Passing-Bablok regression, providing results compatible with null intercept (−0.02 cm², 95% confidence interval −0.19 to 0.12 cm²) and unitary slope (1.00, 95% confidence interval 0.96 to 1.04).

The results can be visually confirmed through the scatter plot of the data and a Bland–Altman plot of the percentage of relative difference between the two methods (Fig. 1D–E). The relative difference was calculated as the absolute difference between the two measures divided by their average and multiplied by 100 to be transformed in a percentage. To assess the repeatability and reproducibility of Woundaries, 3 wounds having small (6.54 cm²), medium (13.38 cm²), and large size (20.05 cm²), were repeatedly measured (n = 10) by three different operators. A statistical analysis performed through a Gage R&R ANOVA showed non-significant differences in wound quantification due to different operators (p-value = 0.923) and interactions (p-value = 0.29) and was used to calculate repeatability (standard deviation = 0.27 cm², corresponding to 4.1% percent study variation) and reproducibility (standard deviation = 0 cm²).



2.2. Wound evolution classification routine

We developed a routine for wound classification, based on model selection, parameter inference, and a statistical test. Time series corresponding to at least 3 wound area measurements collected at different times were analysed using a custom routine written in R 3.5.0 [20] as schematically represented in Fig. 2A.

Time series composed by at least 5 measurements were first analysed through a fitting procedure aimed at establishing whether it was possible to identify a delay time, produced by an initial stall or increase in wound area [17]. This analysis is based on the comparison of the results obtained by fitting the data with two models: a first model, consisting in a simple exponential behaviour with 2 free parameters; and a mixed model, composed by an initial linear behaviour followed by an exponential decay, with 4 free parameters in total (Fig. 2B and C). The best model was determined as the one providing the smallest reduced χ^2 . In order to avoid overfitting, no attempt was made to calculate an initial delay for time series composed by less than 5 measurements; moreover, the delay parameter was constrained to be smaller than the time at which the (n-2)th data point was collected. In the cases in which the mixed model provided a better fitting, only the data collected at times larger than the calculated delay were considered for the following calculations. For time traces composed by 3 or 4 points, the analysis described above was bypassed, and data were directly fed into the ensuing step. At this point, we performed a linear regression of the logarithm of the area vs. time, $\log A = \log A_0 - t/\tau$, where A represent the surface area, t is the time at which the area was measured, A_0 is the area at time zero, and τ is a characteristic time. Based on the fitting results obtained for the characteristic time and its 95% confidence interval, wounds were classified as healing if the null hypothesis, corresponding to $\tau \leq 0$, could be rejected. It must be noticed that a negative τ produces an area increasing with time.

2.3. Data simulations

To test the classification/regression routine performance, we simulated data reproducing area vs. time for both healing and non-healing wounds. The traces were composed by a varying number of data

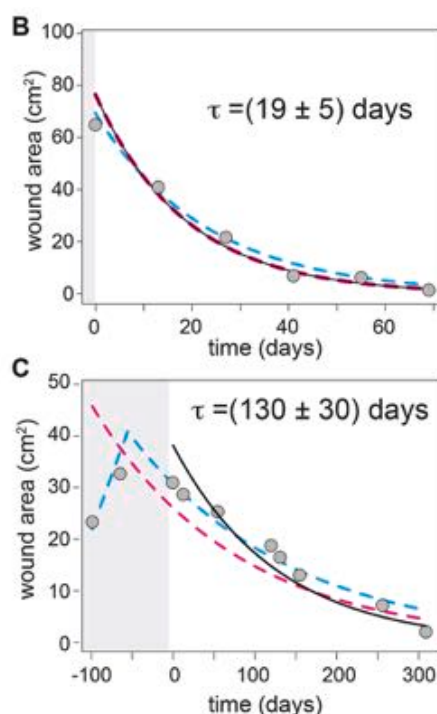


Fig. 2. Schematic and performance of the classification routine. (A) Flow diagram of the procedure used to classify wound as healing or non-healing and calculate the characteristic parameter. (B–C) Representative data sets of wound areas vs. time (circles) and corresponding fits by means of simple exponential (dashed magenta line) and a mixed model (dashed blue line), composed by an initial linear behaviour followed by an exponential decay. The fit comparison was used to determine the best fit and calculate the initial delay. The data in panel (B) were best fitted with a simple exponential and no delay was determined (continuous black line). In contrast, the data in panel (C) were best fitted with a mixed model. Only the data collected at times larger than the delay were considered for further calculations (continuous black line). The characteristic time errors correspond to the 95% confidence interval. (For interpretation of the references to colour in this figure legend, the reader is referred to the Web version of this article.)

points and had a different frequency of collection. To mimic the actual conditions, the logarithm of the area vs. time was simulated as to follow a linear behaviour with different slopes. The data were further corrupted with Gaussian noise with zero mean and standard deviation $\sigma = 0.125$, as estimated from the clinical data (Fig. 3A).

2.4. Methodology application to clinical data

The methodology described above was retrospectively applied to clinical data of patients to evaluate its capability to determine the wound healing kinetics upon different treatments. Patient socio-demographic characteristics, wounds' aetiologies, and wound treatment were collected. Patients were classified between those receiving autologous poor-platelet plasma (PPP) therapy [21] and those receiving general basic therapeutics [4]. The characteristic time of healing was used to classify the wounds as healing ($\tau > 0$) or non-healing. For the healing ones, this parameter was further used for the statistical comparison of wound healing rate upon different treatments.

2.5. Data treatment and statistical analysis

Unless differently specified, data were analysed using parametric tests to compare the mean of two (t-test) or more groups (ANOVA). Shapiro-Wilk and Levene tests were first applied to check for normality and homoscedasticity. Non-normal and heteroscedastic data were Box-Cox or logarithmically transformed. Post-hoc analyses were performed by means of Tukey's honest significant difference test. The tests were considered significant if their p -value was smaller than 0.05.

3. Results

3.1. Wound area measurement

We first validated the tool for wound area and shape characterization. The area of 23 wound planimetries was quantified through the Woundaries (Fig. 1A–C). These results were thus compared to those obtained through the validated device Visitrak [22] applied to the same dataset.

The scatter plot of the results obtained with both methods of measurement (Fig. 1D) display a good agreement. A Bland–Altman plot [23] of their relative differences with respect to the average (Fig. 1E) and a paired t-test ($p = 0.152$) were used to exclude significative differences between both methods. As a further verification, a paired-samples test of equivalence [24] also showed the equivalence of both methods at a level of significance of 5%.

3.2. Wound evolution assessment

We developed and validated a routine for the classification of wound

area time-series and the inference of kinetic parameters. The routine is based on a model selection scheme, followed by a regression for the inference of the characteristic time of healing.

To test its performance, the routine was applied to simulated data corresponding to healing and non-healing wounds. The method shows a high specificity, with a false positive rate well below the nominal type I error (5%). Expectedly, the method sensitivity was found to depend on the number of points available for the fit and to the extent of time these points cover with respect to the healing characteristic time (Fig. 3B). As an example, while with 4 data points covering $\sim 0.87 \tau$ (corresponding to an expected reduction of the initial area of the $\sim 60\%$) it is possible to classify a wound as healing with 90% sensitivity, reaching the same conclusion within a time of $\sim 0.3 \tau$ (corresponding an area reduction of $\sim 25\%$) requires 21 measurements (Fig. 3B). Therefore, our results show that a quantitative inspection of the wound at high frequency can further improve the determination of its evolution.

As an *a posteriori* validation of the model used to describe the data, the logarithm of areas and times were plotted after rescaling by the fitting parameters A_0 and τ , respectively (Fig. 3B), showing a very good agreement.

3.3. Application to clinical data

We carried out a retrospective study on observational data corresponding to 120 wounds from 85 patients treated in our wound clinical outpatient unit between 2015 and 2017. Table 1 shows patients' characteristics.

Fig. 4A and B shows the distribution of wounds with respect to their aetiology and the sex of the patient (4A), and respect to patient age group and sex (4B). Ulcers were treated with PPP therapy (47.5%) or general basic therapeutics (52.5%).

Table 1
Baseline patients' characteristics.

Characteristic		Number of patients (%)
Sex	Males	36 (42.4%)
	Females	49 (57.6%)
Number of ulcers	1 ulcer	59 (69.4%)
	2 ulcers	19 (22.4%)
	3 or 4 ulcers	7 (8.2%)
	Aetiology	
Aetiology	Venous	35 (29.2%)
	Arterial	17 (14.2%)
	Traumatic/surgical	23 (19.2%)
	Pressure	12 (10%)
	Others	33 (27.6%)
Age groups	50–59 years	9 (10.6%)
	60–69 years	21 (24.7%)
	70–79 years	25 (29.4%)
	80–89 years	24 (28.2%)
	90 years or older	6 (7.1%)

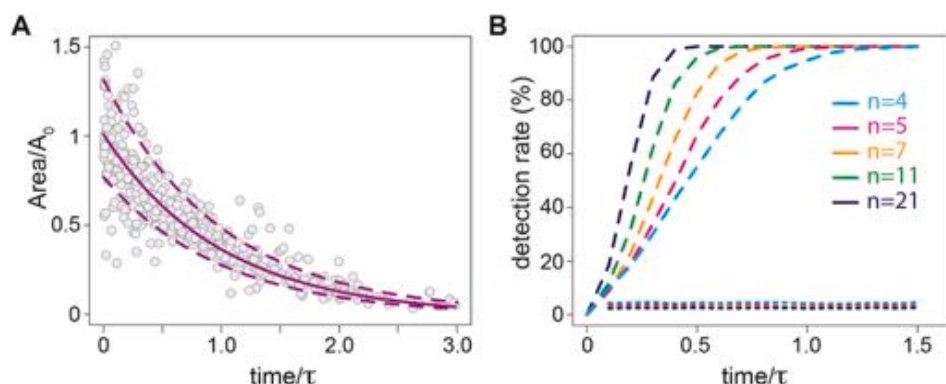


Fig. 3. Performance of the classification routine on simulated data. (A) Plot of all the measured wound areas vs. time (circles) rescaled on the basis of the parameters A_0 and τ calculated by the fitting procedure and for times larger than the respective delays. The agreement with an exponential decay with unitary parameters validates the choice of the model. Dashed magenta lines correspond to standard errors. (B) Detection rate (dashed lines) and false positive error rate (dotted lines) as a function of the normalized characteristic time of healing, as determined from simulations with a varying number of data points (different colours). (For interpretation of the references to colour in this figure legend, the reader is referred to the Web version of this article.)

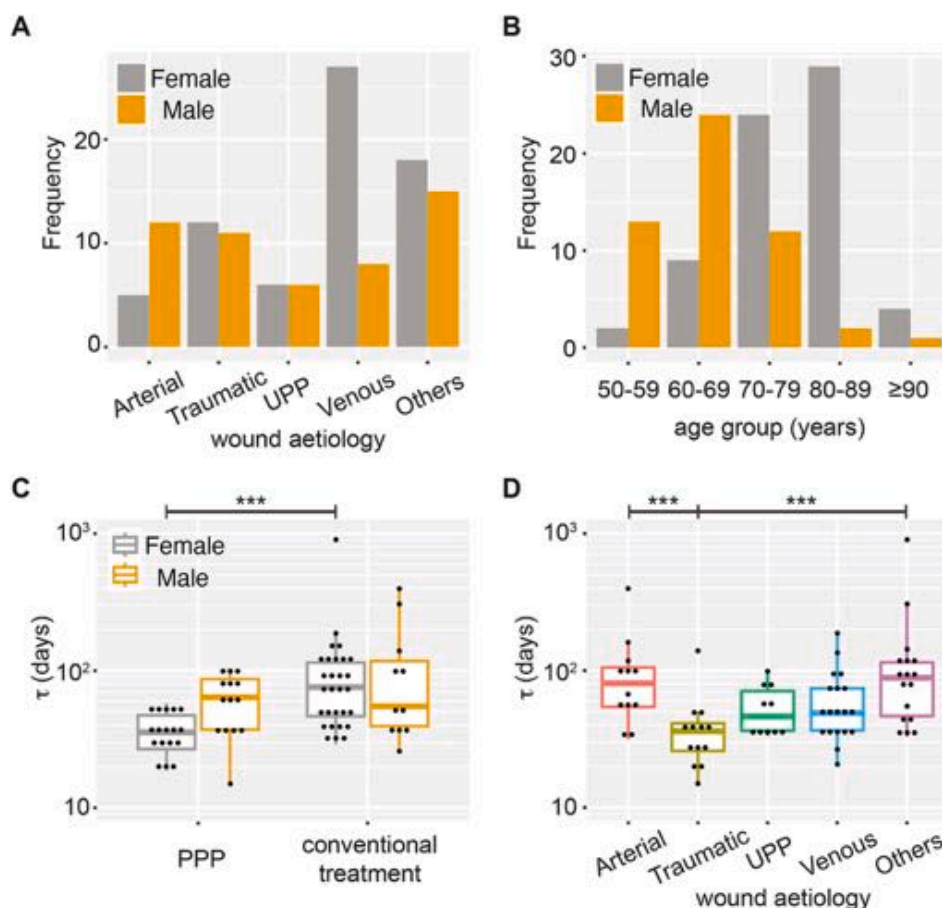


Fig. 4. Statistical analysis of chronic wounds. (A–B) Frequency histogram of the analysed wounds as a function of aetiology and patients' sex (A) and of age group and sex (B). (C–D) Box and whiskers plot of the healing time determine by the fitting algorithm as a function of wound treatment and patients' sex (C) and of wound aetiology (D). *** corresponds to p -value smaller than 0.05.

According to the criterion of classification described above, the PPP therapy did not produce significant differences in the probability of healing (Fisher's test, $p = 0.355$), despite a slightly lower percentage of healing (54.4%) observed in PPP-treated wounds with respect to wounds treated conventionally (63.5%). For healing wounds, the fitting provided the characteristic time of healing τ , corresponding to the time at which the wound area reduces to $\sim 37\%$ of its initial value. This parameter did show a significant difference between groups undergoing different treatments, with a significantly faster healing (lower characteristic time of healing τ) for the PPP-treated ones. This effect can be almost entirely attributed due to female patients (Fig. 4C, $p = 2.5 \times 10^{-4}$), whereas wounds from male patients do not seem to heal faster when treated with PPP. To investigate whether this difference was related to other factors, e.g. a higher incidence of a given type of wound in a sex group, we analysed the healing time with respect to wound aetiology and treatment (Fig. 4D). This analysis shows that traumatic wounds heal significantly faster than arterial ($p = 4.5 \times 10^{-4}$) and unclassified wounds ($p = 6.2 \times 10^{-5}$). Similar analyses were also carried out to explore whether patients' age, the presence of health conditions, and wound location had any influence on the wound healing time but did not show significant effects.

We attempted to find correlation between healing and other measured geometrical parameters (initial wound circularity, roughness, and aspect ratio) as a function of the main factors involved in the study, however we could not find any conclusive evidence.

4. Discussion

Monitoring the evolution of ulcers is a complex process in which quantitative variables such as wound area are essential. Despite emerging methods to measure the area based on photography or 3D scanners, planimetry is still widely used. In this scenario, we reckoned it could be useful to develop a graphic user interface (Woundaries) for wound area measurements. Woundaries aims to provide a user-friendly tool that allows the automatic calculation of wound area together with several shape descriptors from digitalized planimetry. To help the user to intuitively adjust the image, all the steps of the image processing algorithm are visualized. The code works also for partly open curves that can result from an incomplete planimetry drawing. The output data are easily saved in a text file for further processing (e.g., the wound classification step) or batch analysis. Importantly, we demonstrated that measurements obtained by Woundaries are equivalent to those provided by the validated device Visitrack. Being based on digitalized planimetry images, our method does not present fundamental limitations with respect to the size of wound to be assessed. However, we must point out that large wounds (area larger than 400 cm^2) cannot be easily traced on planimetry. Therefore, alternative strategies for the tracing must be used to subsequently enable the use of Woundaries. Additionally, we observed that measurements obtained by Woundaries show a good repeatability and reproducibility in the explored range of wound sizes. The wound descriptors provided by the Woundaries can be further processed by means of other routines for prognostic use. Along this line, we developed a classification routine that uses wound area vs. time traces to sort wound as healing or non-healing. For the healing case,

the characteristic parameter of wound area evolution was also inferred, thus predicting the dynamics of wound closure. With the help of simulations, we analysed the performance of our routine in providing a reliable prognosis as a function of the number and the frequency of measurements. As an example, for a wound with a nominal characteristic healing time of 2.5 months, predicting its evolution with ~70% classification sensitivity requires collecting measurements at least once a week for 5 consecutive weeks. The same sensitivity can be reached earlier if the frequency of measurement is increased. In addition to the need of an accurate methodology, this result further stresses the importance of a regular and frequent clinical follow up of the wound. In fact, wound healing characteristic time should be estimated as soon as possible in order to verify if a specific treatment is being effective.

Since it has been previously reported that other wound and patient factors also have prognostic value [16], the classification routine could provide a more accurate prediction by the simultaneous evaluation of additional wound descriptors as, e.g., the geometrical parameters provided by the Woundaries. However, the implementation of these analyses requires further efforts in studying and modelling their time evolution in healing and non-healing wounds.

The rapid determination of the efficacy of a specific treatment is particularly crucial when applying advanced therapies for chronic wounds [25]. In fact, biological therapies are expensive and time-consuming to prepare; they usually require several applications before their effect could be visually observed. Therefore, a method able to determine the effect of a treatment in a shorter time could significantly contribute to improve wound management.

We applied our methodology to analyse 120 wounds of different aetiologies from patients receiving conventional therapeutics or PPP therapy, a well-established autologous therapy in our clinical facilities. The statistical analysis of the data showed that traumatic wounds heal significantly faster than other aetiologies such as venous wounds. Moreover, while the PPP therapy does not seem to increase the probability of healing as compared to conventional treatment, it shows a significant effect in reducing the wound closure time in female patients. However, assessing whether this is a direct effect of patient's sex or a consequence of other factors, such as the higher incidence among female patients of wounds with a shorter healing time (e.g. venous wounds), requires further verification.

In addition, we didn't report any relation with healing kinetics and initial morphology although other authors reported some correlations studying a unique aetiology wounds [26,27].

5. Conclusion

In this study, we demonstrated a reliable and user-friendly method for the quantification of area and shape descriptors from digitalized hand-traced planimetries. Based on our results, the proposed method has a straightforward implementation and could be easily adopted in routine wound monitoring. In this sense, we are currently developing a phone/tablet app including the Woundaries capabilities.

Our methodology provides information on wound healing evolution and estimates kinetic parameters of the process. It is based on an objective evaluation of parameters of wound evolution and provides the early identification of non-healing wounds, thus facilitating the assessment of the efficacy of therapies. Therefore, we believe that our methodology can assist sanitary staff in clinical decision making, thus improving chronic wounds management and early prediction of wounds evolution.

Funding sources

This work was supported by the FEDER/Ministerio de Ciencia, Innovación y Universidades – Agencia Estatal de Investigación through the “Ramón y Cajal” program 2015 (Grant No. RYC-2015-17896); the “Programa Estatal de I+D+i Orientada a los Retos de la Sociedad”

(Grant No. BFU2017-85693-R); “Suport als grups de recerca de Catalunya SGR” from the Generalitat de Catalunya (AGAUR Grant No. 2017SGR940); the Department of Health of the Catalan Government (Generalitat de Catalunya) through the “Pla Estratègic de Recerca i Innovació en Salut (PERIS)” program 2016 (SLT002/16/00191); the PO FEDER of Catalonia 2014–2020 (project PECT Osona Transformació Social, Ref. 001-P-000382); the Spanish Ministry of Science, Innovation, and Universities through the Instituto de Salud Carlos III FEDER program (FIS PI19/01379); and the Industrial Doctorates Plan of the Secretary for University and Research of the Ministry of Business and Knowledge of the Generalitat de Catalunya (2019DI054).

Conflicts of interest

The authors have no conflict of interest.

Acknowledgments

The authors kindly acknowledge Jesús Rebull and Pablo Magán for preliminary image analysis and quantification, and all the members of the wound clinical unit of the Hospital Universitari de la Santa Creu de Vic for help with data collection.

References

- [1] Singer AJ, Clark RAF. Cutaneous wound healing. *N Engl J Med* 1999;341:738–46. <https://doi.org/10.1056/NEJM199909023411006>.
- [2] Frykberg RG, Banks J. Challenges in the treatment of chronic wounds. *Adv Wound Care* 2015;4:560–82. <https://doi.org/10.1089/wound.2015.0635>.
- [3] Han G, Ceilley R. Chronic wound healing: a review of current management and treatments. *Adv Ther* 2017;34:599–610. <https://doi.org/10.1007/s12325-017-0478-y>.
- [4] Otero-Viñas M, Falanga V. Mesenchymal stem cells in chronic wounds: the spectrum from basic to advanced therapy. *Adv Wound Care* 2016;5:149–63. <https://doi.org/10.1089/wound.2015.0627>.
- [5] Papazoglou ES, Zubkov L, Mao X, Neidrauer M, Rannou N, Weingarten MS. Image analysis of chronic wounds for determining the surface area. *Wound Repair Regen* 2010;18:349–58. <https://doi.org/10.1111/j.1524-475X.2010.00594.x>.
- [6] Jørgensen LB, Sørensen JA, Jemec GBE, Yderstræde KB. Methods to assess area and volume of wounds – a systematic review. *Int Wound J* 2016;13:540–53. <https://doi.org/10.1111/iwj.12472>.
- [7] Foltynski P, Ladyzynski P, Ciechanowska A, Migalska-Musial K, Judzewicz G, Sabalinska S. Wound area measurement with digital planimetry: improved accuracy and precision with calibration based on 2 rulers. *PLoS One* 2015;10:1–13. <https://doi.org/10.1371/journal.pone.0134622>.
- [8] Stockton KA, McMillan CM, Storey KJ, David MC, Kimble RM. 3D photography is as accurate as digital planimetry tracing in determining burn wound area. *Burns* 2015;41:80–4. <https://doi.org/10.1016/j.burns.2014.04.022>.
- [9] Foltynski P. Ways to increase precision and accuracy of wound area measurement using smart devices: advanced app Planimator. *PLoS One* 2018;13:e0192485. <https://doi.org/10.1371/journal.pone.0192485>.
- [10] Khong PCB, Yeo MSW, Goh CC. Evaluating an iPad app in measuring wound dimension: a pilot study. *J Wound Care* 2017;26:752–60. <https://doi.org/10.12968/jowc.2017.26.12.752>.
- [11] Frade RA, Vardasca R, Carvalho R, Mendes J. Automatic classification of ulcers through visual spectrum image. *Eur. Congr. Comput. Methods Appl. Sci. Eng.* 2018: 297–305. https://doi.org/10.1007/978-3-319-68195-5_32.
- [12] O'Meara SM, Bland JM, Dumville JC, Cullum NA. Systematic review of wound measurement instruments. *Wound Repair Regen* 2012;20:263–76. <https://doi.org/10.1111/j.1524-475X.2012.00783.x>.
- [13] Cardinal M, Phillips T, Eisenbud DE, Harding K, Mansbridge J, Armstrong DG. Nonlinear modeling of venous leg ulcer healing rates. *BMC Dermatol* 2009;9. <https://doi.org/10.1186/1471-5945-9-2>.
- [14] Wallenstein S, Brem H. Statistical analysis of wound-healing rates for pressure ulcers. *Am J Surg* 2004;188. [https://doi.org/10.1016/S0002-9610\(03\)00294-0](https://doi.org/10.1016/S0002-9610(03)00294-0).
- [15] Cukjati D, Reberšek S, Karba R, Miklavčič D. Modelling of chronic wound healing dynamics. *Med Biol Eng Comput* 2000;38:339–47. <https://doi.org/10.1007/BF02347056>.
- [16] Robnik-Šikonja M, Cukjati D, Kononenko I. Comprehensive evaluation of prognostic factors and prediction of wound healing. *Artif Intell Med* 2003;29: 25–38. [https://doi.org/10.1016/S0933-3657\(03\)00044-7](https://doi.org/10.1016/S0933-3657(03)00044-7).
- [17] Cukjati D, Reberšek S, Miklavčič D. A reliable method of determining wound healing rate. *Med Biol Eng Comput* 2001;39:263–71. <https://doi.org/10.1007/BF02344811>.
- [18] Cullell-Dalmau M, Otero-Viñas M, Manzo C. Research techniques made simple: deep learning for the classification of dermatological images. *J Invest Dermatol* 2020;140:507–14. <https://doi.org/10.1016/j.jid.2019.12.029>. e1.

- [19] Kovesi PD. {MATLAB} and {Octave} functions for computer vision and image processing n.d.
- [20] R Core Team. R. A language and environment for statistical computing. Vienna, Austria: R Foundation for Statistical Computing; 2018.
- [21] Ss H, Elshahat A, Elsherbiny K, Massoud K, Safe I. Platelet-rich plasma versus platelet-poor plasma in the management of chronic diabetic foot ulcers: a comparative study. *Int Wound J* 2011;8:307–12. <https://doi.org/10.1111/j.1742-481X.2011.00797.x>.
- [22] Chang A, Dearman B, Greenwood JE. A comparison of wound area measurement techniques: visitrak versus photography. *Eplasty* 2011;11:e18.
- [23] Altman DG, Bland JM. Measurement in Medicine : the analysis of method comparison studies. *Statistician* 1983;32:307–17. <https://doi.org/10.2307/2987937>.
- [24] Mara CA, Cribbie RA. Paired-samples tests of equivalence. *Commun Stat Simulat Comput* 2012;41:1928–43. <https://doi.org/10.1080/03610918.2011.626545>.
- [25] Lindholm C, Searle R. Wound management for the 21st century: combining effectiveness and efficiency. *Int Wound J* 2016;13:5–15. <https://doi.org/10.1111/iwj.12623>.
- [26] Gorin DR, Cordts PR, LaMorte WW, Menzoian JO. The influence of wound geometry on the measurement of wound healing rates in clinical trials. *J Vasc Surg* 1996;23:524–8. [https://doi.org/10.1016/S0741-5214\(96\)80021-8](https://doi.org/10.1016/S0741-5214(96)80021-8).
- [27] Cardinal M, Eisenbud DE, Armstrong DG. Wound shape geometry measurements correlate to eventual wound healing. *Wound Repair Regen* 2009;17:173–8. <https://doi.org/10.1111/j.1524-475X.2009.00464.x>.

ARTICLE 3. Research Techniques Made Simple: Deep Learning for the Classification of Dermatological Images

The objective of this article was to introduce the basics of deep learning (DL) architecture for clinical image classification, in a manner accessible to nonexperts to support them in interpreting and evaluating scientific publications involving these tools.

In this review article, we introduced the readers to several concepts related to artificial intelligence, machine learning, and DL. We also explained the fundamental operations applied by DL routines and described the metrics for the evaluation of its performance.

First, we explained the main operations performed for a CNN, starting with the input image decomposition. Then we detailed the importance of the kernel used for the convolution, its size and the influence of the shifting steps or stride, and the down-sampling image output because of this process. Once the parts were introduced, we discussed the general architecture of the CNN. We explained the architecture of a basic fully connected network composed of an input layer, several hidden convolutional layers, and an output layer. Next, we also described a series of tests used to quantify the model performance, like classification accuracy, the area under the curve, or the receiver operating characteristics curve.

Secondly, we presented examples of recent applications for dermatology image analysis, especially in the field of skin cancer, to show the capability of DL to achieve a highly accurate classification of those lesions. We briefly explained the classification process performed by the ResNet-152 CNN, its architecture, and its outstanding performance obtained in skin lesions classification.

Although the equivalence between computer and human diagnosis has been reported, in this article, we also identified and discussed several limitations or

challenges in the use of DL in medicine. Among them: 1) the need of having a large training dataset of images to avoid any bias by including images from different conditions, ethnicities, and other clinical conditions, 2) the need for standardized images associated with precise clinical metadata, and 3) the difficulty of obtaining information about the decision-making process established during automatic classification.



Research Techniques Made Simple: Deep Learning for the Classification of Dermatological Images

Marta Cullell-Dalmau¹, Marta Otero-Viñas^{2,3} and Carlo Manzo¹

Deep learning is a branch of artificial intelligence that uses computational networks inspired by the human brain to extract patterns from raw data. Development and application of deep learning methods for image analysis, including classification, segmentation, and restoration, have accelerated in the last decade. These tools have been progressively incorporated into several research fields, opening new avenues in the analysis of biomedical imaging. Recently, the application of deep learning to dermatological images has shown great potential. Deep learning algorithms have shown performance comparable with humans in classifying skin lesion images into different skin cancer categories. The potential relevance of deep learning to the clinical realm created the need for researchers in disciplines other than computer science to understand its fundamentals. In this paper, we introduce the basics of a deep learning architecture for image classification, the convolutional neural network, in a manner accessible to nonexperts. We explain its fundamental operation, the convolution, and describe the metrics for the evaluation of its performance. These concepts are important to interpret and evaluate scientific publications involving these tools. We also present examples of recent applications for dermatology. We further discuss the capabilities and limitations of these artificial intelligence-based methods.

Journal of Investigative Dermatology (2020) **140**, 507–514; doi:10.1016/j.jid.2019.12.029

ARTIFICIAL INTELLIGENCE, MACHINE LEARNING, AND DEEP LEARNING

Artificial intelligence (AI) describes a branch of computer science that uses machines to simulate cognitive functions of the human mind, such as learning or reasoning (Figure 1). An increasing number of systems based on AI, such as voice-powered assistants like Alexa and Siri, are progressively affecting human habits. Self-driving cars, speech recognition, and machine vision promise to broadly improve human lives, with applications to business, education, and healthcare.

Subcategories of AI include machine learning (ML) and deep learning (DL, Figure 1). ML is based on the acquisition of knowledge from data and does not provide specific rules for a given task; the machine undergoes a learning process based on examples and optimizes its performance on a specific assignment. ML has been successfully applied to several tasks, including classifying gene expression patterns associated with diseases, predicting protein structures from genetic sequences, or designing chemical scaffolds in drug discovery (Marx, 2019). Generally speaking, DL is one of the several computing systems for ML inspired by the biological neural networks that constitute the human brain. DL utilizes artificial neural networks (ANNs), which attempt to mimic how the brain works, especially the connections between neurons. An

ANN is formed by a collection of nodes (also called artificial neurons) arranged in layers and connected to transmit signals (Figure 2). Typically, each signal consists of a number, and the output of each node is a nonlinear function of the sum of the inputs. Nodes and connections are characterized by weights that are adjusted through the learning process to increase or decrease the strength of a given signal. The aggregate signal of an artificial node may pass through an activation function, such as transmitting only signals above a threshold (Figure 2a). An ANN may have a single or multiple hidden layers between the input and the output. The number of hidden layers and the number of nodes in each layer constitute the variables controlling the architecture of the network, called hyperparameters. ANNs with several hidden layers are generally referred to as deep neural networks, thus leading to the use of the term deep learning (Figure 2b). However, there is no clear consensus on the minimum number of layers for a network to be qualified as deep. One of the first deep ANNs had only three hidden layers (Hinton et al., 2006). A high number of layers makes DL more capable than traditional ML of modeling complex data. Moreover, DL can automatically discover the features needed to accomplish its task, whereas ML requires being programmed with the criteria defining such features. However,

¹QuBI lab, Faculty of Sciences and Technology, University of Vic – Central University of Catalonia, Vic, Spain; ²Tissue Repair and Regeneration Laboratory, Faculty of Sciences and Technology, University of Vic – Central University of Catalonia, Vic, Spain; and ³Faculty of Medicine, University of Vic – Central University of Catalonia, Vic, Spain

Correspondence: Carlo Manzo, Faculty of Sciences and Technology, University of Vic – Central University of Catalonia, C. de la Laura, 13 - 08500, Vic, Spain. E-mail: carlo.manzo@uvic.cat

Glossary of terms can be found at the end of this paper.

Abbreviations: AI, artificial intelligence; ANN, artificial neural network; AUC, area under the curve; CNN, convolutional neural network; DL, deep learning; ISIC, International Skin Imaging Collaboration; ML, machine learning; ROC, receiver operating characteristic

SUMMARY POINTS

- Inspired by the visual cortex mechanism, convolutional neural networks exploit the information contained in image datasets to automatically learn features and patterns not always identified by humans.
- Deep learning has demonstrated the capability of achieving highly accurate classification of images of skin lesions associated with cancer and other dermatological conditions.
- Deep learning might be a formidable tool to potentially assist dermatologists in their diagnostic decisions.
- Important limitations to the extension of deep learning methods to care practice include the lack of clarity of the automated decision-making process, inherent to convolutional neural networks and concerns about its accuracy, related to the use of not fully representative training datasets or nonstandardized images.

Advantages

- Automated classification of images of skin lesions associated with different diseases with high accuracy.
- Short execution time after training.
- Useful to support clinicians in diagnosis
- Cost saving by reducing unnecessary biopsies or instrumental analysis.

Limitations

- Need for large training datasets including images from different conditions, ethnicities, and settings.
- Need for standardized images associated with precise clinical metadata.
- Obscure decision-making process for classification.
- Limited accuracy and generalizability when trained on datasets with underrepresented conditions.

as a consequence of the higher number of weights to be determined, the training of DL networks requires large quantities of data.

CONVOLUTIONAL NEURAL NETWORK

Study and application of DL has rapidly accelerated in academic research, business, and popular interest. These advances have been based mainly on the use of the convolutional neural network (CNN), an algorithmic architecture inspired by the human visual cortex (Schmidhuber, 2015). Although CNNs were invented in the 1980s (Fukushima, 1980), it was not until the early 2010s that

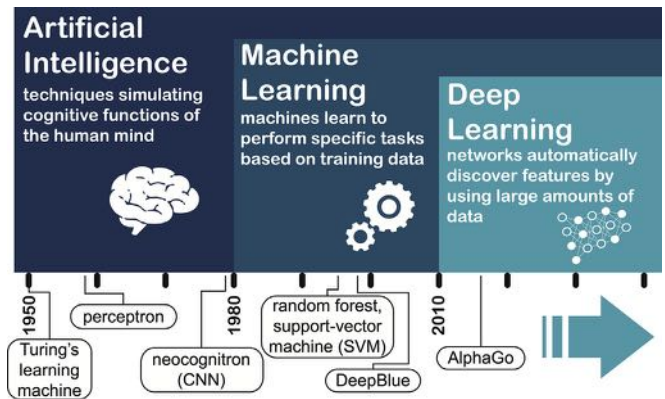


Figure 1. The evolution of artificial intelligence, machine learning, and deep learning. Schematic representation of the timeline and relationship between the three fields, together with a few representative key milestones. CNN, convolutional neural network; SVM, support-vector machine.

massive amounts of labeled data became available for training (Wehner et al., 2017). The growth of computer power deriving from graphics-processing units have fueled massive application of CNNs, in particular as a tool for image classification. As an example of their versatility and power, a CNN constitutes the core of AlphaGo, the computer system that defeated the world’s best human player at the game Go (Silver et al., 2016).

As implied by their name, CNNs are mainly based on convolutional layers. Convolution is a mathematical operation between two mathematical functions, which consists in taking element-wise multiplications followed by a sum while shifting one function along the other. CNNs are very well-suited to work with images because of their similarity with

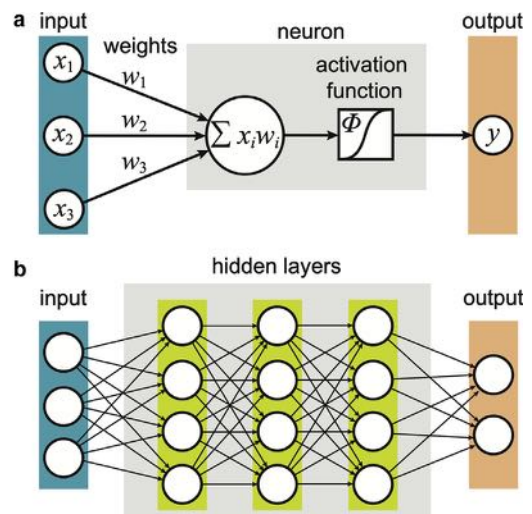


Figure 2. Artificial neurons and neural networks. (a) Structure of a node or artificial neuron. The neuron receives inputs from one or more sources, multiplies each of these inputs by a weight, and adds the resulting products. The resulting sum is passed to an activation function and it provides a single output. (b) Schematic representation of a basic fully connected network. For illustrative purpose, we show a simple network composed of an input layer, three hidden layers, and an output layer. Each hidden layer is composed of four nodes. The training process creates a model by assigning values to all the weights of the network.

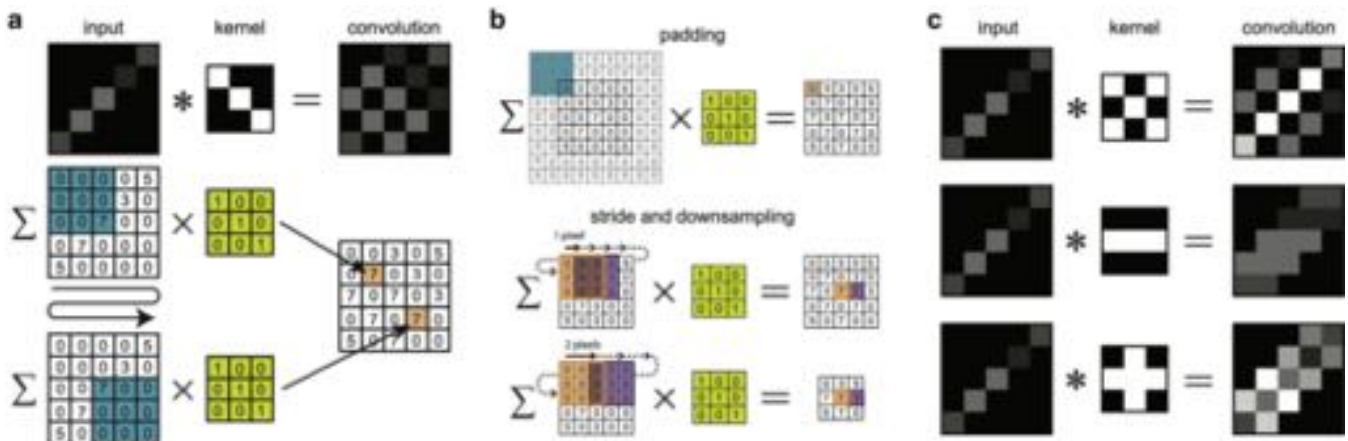


Figure 3. The basics of a CNN: the convolution operation. (a) Example of the convolution (*) of a 5×5 pixels² grayscale image with a 3×3 pixels² kernel. Grayscale images correspond to numeric matrices, where each pixel is associated with a numeric value. The convolutional feature is obtained by shifting the kernel over the image. At each position, the value of a pixel of the convolutional feature is obtained by multiplying each pixel of the input image by the corresponding pixel of the kernel and then taking the sum. (b) Symmetrically padding the input with zeros allows the kernel to operate at the edges of the image and thus preserve the size. Downsampled images can be obtained by changing the stride, the step length at which the kernel is shifted along the input. (c) Examples of different features obtained by applying different convolutional kernels to the same input image. CNN, convolutional neural network.

the animal visual cortex, which is composed by neurons that individually respond to small regions of the visual field. An image can be simply viewed as a collection of planes (corresponding to different colors, e.g., 3 for RGB or 1 for grayscale), where each plane is a two-dimensional matrix of numbers (the pixel values).

The convolution of an image plane implies the use of a second matrix, called a kernel, which is shifted along the first one. At each shift position, every pixel of the region of the input image overlapping with the kernel is multiplied by the corresponding pixel of the kernel. The sum of these products produces the value of a pixel of the convolutional feature (Figure 3a). Thus, the pixels of the kernel act like the weights of an artificial neuron over an input corresponding to a region of the input image. The kernel size defines the receptive field of the neuron, that is, the region of the input that is codified into a single value of the output. To make it possible for the kernel to operate at the edges of the input image and preserve the size, convolutional layers generally use zero-padding, the insertion of zero elements around the input image (Figure 3b). Moreover, the convolved image can be obtained by shifting the kernel in steps of one or more pixels. The length of these steps is called stride and, if larger than one, provides an output with smaller lateral size with respect to the original image (Figure 3b). In this way, the convolution can allow for the downsampling of the image while retaining information contained in adjacent pixels.

An important characteristic of convolution is that it can perform different operations on the original image by changing the kernel (Figure 3c). Examples of these operations include blurring, sharpening, denoising, and edge detection. Therefore, a clever combination of randomly selected kernels can lead to the refinement of the computer vision model and, thus, lead to the discovery of new properties.

CNN workflow and model evaluation

To better understand how a CNN works, we will discuss a schematic example from dermatology. Although several types

of algorithms have been developed, because of space limitations, we will focus on a supervised learning algorithm for skin lesion classification (Figure 4a). The task of the algorithm is to determine from a digital photograph (input) whether a skin lesion is associated with a malignant cancer or is a benign lesion (output). Because the possible outputs are limited to a finite set of values (only two in this case), this is a (binary) classification problem.

In a typical CNN architecture for classification, the input image is progressively downsampled while increasing the number of kernels and thus obtaining more convolutional features. The last layers have the role of transforming the feature map into a vector, the values of which represent the probability that the image belongs to each class (Figure 4a). In addition to convolutional layers, other layers contribute to perform the mathematical operations necessary to transform the input image and to associate it to the output class. However, their description goes beyond the scope of this article.

In a supervised approach, the algorithm is trained using a labeled dataset, a set of images for which the gold standard output label has been obtained with alternative methods, such as a biopsy. As further detailed in Torres and Judson-Torres (2019), the data are usually split in the following three cohorts: the training set, which is used to determine the weights characterizing the model; the validation set, which is used to assess the model performance during training; and the test set, which is used to evaluate how well the model performs on an unknown input. A CNN iteratively updates the kernel weights of its layers in a random fashion to automatically calculate features from the images and combine them to optimize the connection between the input and the output on the training dataset.

Once the training is complete, the test set is used to quantify the model performance. The simplest quality measure is the classification accuracy, which reports the percentage of correct predictions over the total. However, a high accuracy alone does not guarantee the goodness of a model.

RESEARCH TECHNIQUES MADE SIMPLE

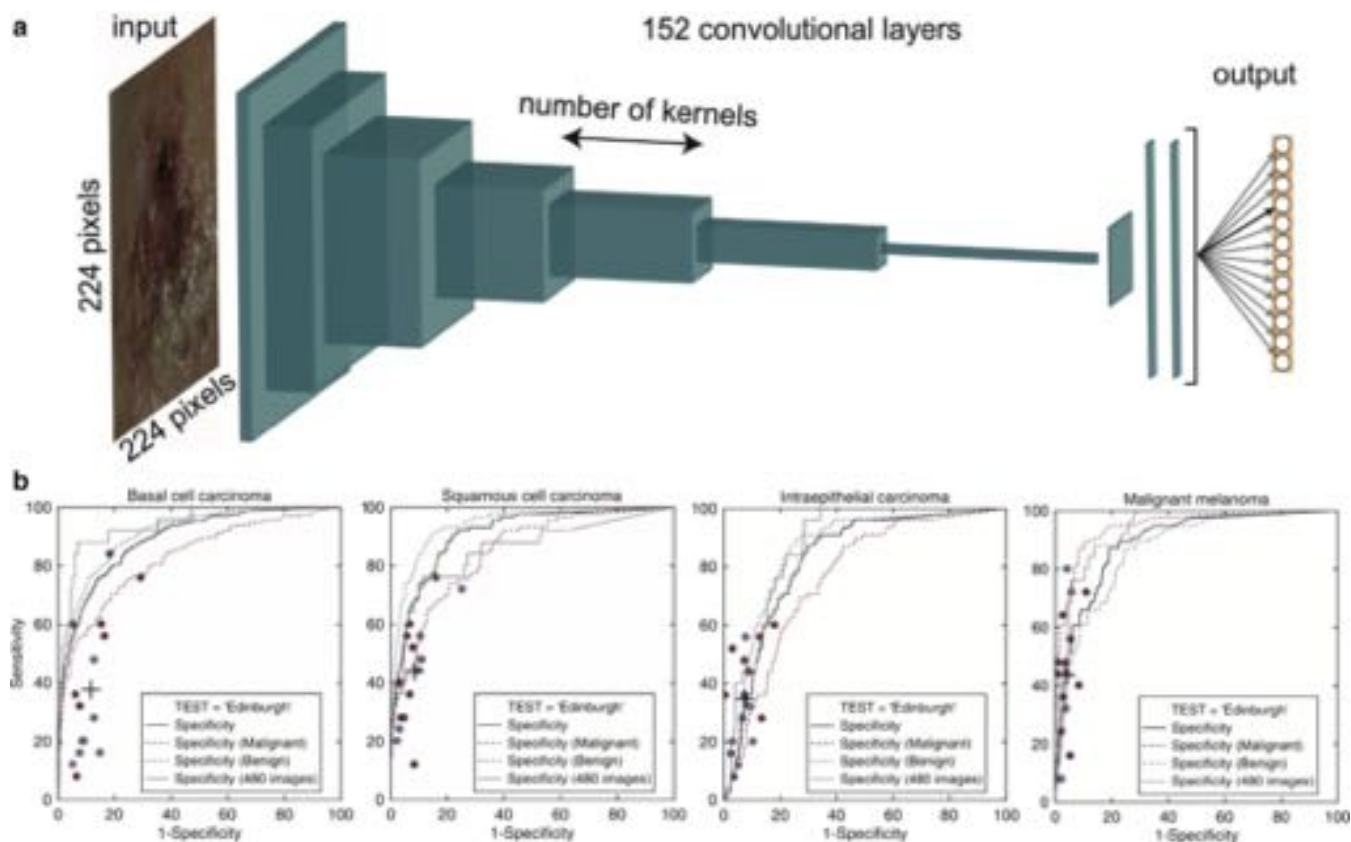


Figure 4. CNN applied to skin cancer classification. (a) Scheme of the ResNet-152 CNN used by Han et al. (2018a). Input images with a size of 224×224 pixels² are analyzed through 152 convolutional layers and classified among 12 different skin diseases. At each block of layers, the CNN progressively downsamples the images while increasing the number of kernels and thus obtaining more convolutional features. The last layers transform the feature map into a vector, the values of which represent the probability that the image belongs to each class. (b) ROC curves for the prediction of malignancy in the Edinburgh dataset cases (220 images) reported in Han et al. (2018a). The gray curve corresponds to the results obtained by the ResNet-152 CNN in comparison with 16 dermatologists (red and blue dots). The other curves display the global specificity (black) and the specificity for benign (blue) and malignant conditions (red). CNN, convolutional neural network; ROC, receiver operating characteristic.

For example, a naïve model that always classifies skin lesions as benign will score 96% accuracy on an unbalanced dataset containing 100 images of skin lesions of which only 4 correspond to cancer. The same model will only reach 50% accuracy on a balanced dataset in which the images are equally split between the categories. This ambiguity can be removed by using the confusion matrix, a table reporting the number of correct and incorrect predictions with respect to the actual class. These metrics provide a complete overview of the performance of a model, and its off diagonal elements characterize the level of misclassification.

The typical output of a binary classifier is a numerical value associated with the probability that a given image belongs to the cancer or benign class. A threshold must thus be set to assign an input to one of these two classes based on this probability value. This property allows for the definition of another useful metric for model performance, the area under the curve (AUC) of the receiver operating characteristic (ROC) curve (Figure 4b). The ROC curve is the plot of the sensitivity against the false positive rate (i.e., one minus the specificity) obtained by varying the discrimination threshold used to assign the input to either of the two classes (Figure 4b). It is important to note that the ROC is insensitive to the proportion of the elements contained in each class (Fawcett, 2006). The

ROC curve will go from the origin of the axes (0, 0) to (100%, 100%) with a trend that depends on the model behavior. An ROC curve steeply increasing toward high sensitivity at small false positive rates indicates a model that achieves high recall without significantly losing precision. In contrast, an ROC curve increasing with a 45° slope indicates a model with no predictive power. The AUC of the ROC curve can thus be used as a metric to summarize the ROC behavior, because a larger AUC is obtained for models more capable of correctly discriminating between classes.

When extending the problem to a multiclass classification, the confusion matrix further allows for simultaneously visualizing the results of all the classes at a glance. The calculation of the ROC curve becomes a complicated multidimensional problem. A simplification relies on calculating an ROC curve for each class against all the others. However, this approximation removes the insensitivity of the ROC to class imbalance (Fawcett, 2006). An alternative metric for multiclass problems is the top-(n) accuracy, which scores the probability of providing the correct classification within its (n)th choice. In fact, for a given input, a multiclass model will provide probability outputs associated with each class, which will allow ranking of the categories from the most likely (highest output probability) to the least. The top-(1)

accuracy, calculated by taking into account only the prediction associated with the highest output probability, provides the percentage of inputs correctly classified, that is, the standard accuracy. The top-(n) accuracy relaxes this condition by quantifying if the correct class is within the top-(n) outputs provided by the model.

Recent applications to dermatology

Without any prior knowledge about dermatological images, CNNs extract and combine sets of abstract features and automatically generate identifying characteristics (such as a combination of colors, shape, texture, and border geometry) associated with different data categories. In this way, a CNN will learn how to achieve a precise classification of images not included in the training dataset and even find patterns not identified by humans.

In the last years, researchers have started to extensively use DL and CNNs for the analysis of medical images from several disciplines, including dermatology (Esteva et al., 2019; Litjens et al., 2017). Because skin cancer is one of the most common malignancies globally, important efforts have been dedicated to its detection from dermoscopic images only (Codella et al., 2015) or in combination with regular photographic images (Esteva et al., 2017).

To support research and development of methods for automated diagnosis of melanoma, the International Skin Imaging Collaboration (ISIC) has developed a repository of dermoscopic images and it yearly organizes a challenge for the analysis of images of skin lesions (Codella et al., 2018; Marchetti et al., 2018; Tschandl et al., 2019). All the teams taking part in the ISBI melanoma detection challenge in 2016 used DL methods. In 2017, approaches combining DL with additional data led to the highest performance in classification tasks. DL is rapidly becoming the method of choice for image analysis, as testified by the increasing number of publications, especially in the last two years (Brinker et al., 2018). Unquestionably, a milestone was set by the work published in Nature by Esteva et al. (2017), in which a standard CNN architecture (Google's Inception v3) was trained on both dermoscopic and standard photographic images using a dataset of over 100,000 images. The authors proved that the CNN performed similarly to tested experts in classifying malignant versus benign lesions of both epidermal and melanocytic origin. Several other studies have been devoted to the same topic by using other CNN architectures (Fujisawa et al., 2019; Haenssle et al., 2018; Han et al., 2018a). As an example, Figure 4 depicts the architecture of the ResNet-152 CNN used by Han et al. (2018a) and some of the corresponding results. All of these works have reported the equivalence between computer and human diagnosis. Besides skin cancer detection, DL is also being successfully applied to other areas of dermatology, such as the monitoring of wound healing (Shenoy et al., 2018), the classification of ulcers (Goyal et al., 2018), and onychomycosis (Han et al., 2018b).

In addition to classification tasks, DL-based models for the segmentation of skin lesions and ulcers have also been successfully developed (Yap et al., 2019). In particular, these methods have been shown to provide an accurate

wound area quantification (Lu et al., 2017; Wang et al., 2015) and promising results on image-based identification of distinct tissues within dermatological wounds (Blanco et al., 2020).

LIMITATIONS AND CHALLENGES

Advances in DL have been accompanied by contrasting reactions. Enthusiastic claims about the outperformance of human diagnosis have been dampened by doubts and criticisms about DL being nothing but an overhyped black box. As always, the truth seems to lie somewhere in between. DL has undoubtedly achieved notable accomplishments in very specific tasks and fields, but it is still far from the realization of a human-equivalent AI.

DL is often considered a black box because its decision-making process is somehow obscured by the thousands of training parameters. In practice, weights and features are often uninterpretable and it is thus difficult for the researchers to fully grasp the working process of a model or the reason why it provides specific performance. The extent to which the inner working of a CNN can be explained in human terms is referred to as explainability. Improving explainability represents a key point for AI to ultimately make decisions on behalf of humans in critical areas, such as in health care. Efforts for gaining insight into why a CNN made a specific decision involve the development of methods to visualize what a CNN sees, such as saliency maps that simplify CNN feature maps into a more meaningful representation.

Because DL approaches are data-driven, their principal limitations often come from the data themselves. A usual criticism concerns the need for large labeled datasets. However, the development of transfer learning has relaxed this requirement by introducing the ability to reuse a model developed for a task and trained on a large dataset as the starting point of a new model with a different task.

Beyond the role of the amount of data, the work of Han et al. (2018a) triggered an interesting discussion about the composition of the training dataset. A letter to the editor of the *Journal of Investigative Dermatology* (Navarrete-Dechent et al., 2018) raised concerns about the generalizability of automated diagnosis when the training dataset presents limitations in the spectrum of human populations and/or clinical presentation, as well as variability in image acquisition settings and limited clinical metadata. Indeed, the underrepresentation of clinical or demographic categories is a common and often inherent problem in healthcare-related data, and it might limit the generalizability of a model.

The inclusion of metadata containing sociodemographic information about the patient (sex, skin type, race, and age) is thus necessary to verify the presence of biases related to imbalance or underrepresentation (Navarrete-Dechent et al., 2018). When possible, the obvious solution to this problem is to broaden the dataset by including images and data of patients from less represented groups. As an alternative, the robustness of a model requires further validation, such as through prospective studies.

An inherent weakness of many of the DL models applied so far to dermatology resides in the lack of a "none of the above"

RESEARCH TECHNIQUES MADE SIMPLE

output. If presented with an image not corresponding to any of the training classes, a model will force it into one of the other categories. In this case, to deal with this issue and prevent misclassification, it is thus necessary to use an approach enabling open set recognition.

The lack of standardization of dermatological images represents a strong limitation that affects the development of the research in this field and undermines its integrity and reproducibility. The variability of dermatological images is due to several causes, such as the type of device used to acquire the images, the image acquisition conditions, the amount and type of metadata, and the lack of a standard terminology. Establishing common criteria for data collection and management is fundamental for the creation of large datasets and their sharing between systems and users. Moreover, the lack of standardization, together with the opacity of the CNN inner process, poses a problem for the operation of classifiers. For example, if images of lesions associated with a specific pathology are generally taken at a high resolution, a CNN might learn to detect the high resolution instead of discriminating the right diagnosis.

An effort toward the establishment of standardized conditions is being carried out by the ISIC to ensure image quality, privacy, and interoperability. The project includes the creation of a public archive of images (<https://isic-archive.com>) to permit independent assessment of the performance of any software. According to ISIC guidelines, images should comply to standards belonging to three categories, technology, technique, and terminology. Furthermore, the presence of detailed metadata including device characteristics, photograph settings, and information about both the patient and the skin lesion is of paramount importance to take full advantage of the information contained in the images. However, the large number of images needed for training further imposes the development of a quality test to automatically assess whether an image respects such quality standards.

Besides image standardization, another strategy might involve the use of an algorithm to intrinsically take this variability into account by introducing an ad hoc augmentation procedure capable of artificially creating variations of brightness, camera angle, body geometry, and skin background, or even introducing rulers, as observed in actual images. Variability sources associated with technical and geometrical parameters might either be measured separately or estimated from the image itself and thus corrected or accounted for by an image preprocessing step. An effective contribution in this sense might come from other DL architectures that are able to infer information such as depth or shape from regular images.

The importance of clinical metadata deserves to be further stressed, because it has also been shown that combining lesion images with sociodemographic data (age and sex), clinical variables (location of the lesion), and close-up images improved the performance of a classifier ([Haenssle et al., 2018](#)).

In conclusion, DL and CNN have demonstrated the capability of achieving highly accurate diagnoses in the classification of skin cancer and other dermatological conditions. DL constitutes a formidable tool to potentially assist dermatologists in their clinical decisions. The computer science and

MULTIPLE CHOICE QUESTIONS

1. Which of the following statements about artificial intelligence is FALSE?
 - A. It is a branch of computer science.
 - B. It is a synonym of deep learning.
 - C. It includes machine learning and deep learning as subcategories.
 - D. It uses machines for simulating cognitive functions of the brain.
2. The advantages of convolutional neural networks do NOT include:
 - A. Automated image classification with high accuracy.
 - B. Once training is done, it achieves fast classification.
 - C. It combines abstract features to find patterns.
 - D. Fast training by using small labeled databases, publicly available.
3. Which of the following statements about convolutional neural network datasets is TRUE?
 - A. They are usually divided into three groups for training, validation, and test.
 - B. Relatively large datasets are needed.
 - C. It needs to be labeled with the correct output.
 - D. All of the above.
4. Which of the following quantities are usually used to evaluate the performance of a classifier?
 - A. The area under the receiver operating characteristic curve.
 - B. The ratio between sensitivity and specificity.
 - C. The false positive rate at varying thresholds.
 - D. The Jaccard index.
5. Deep learning is often dubbed “black box” because:
 - A. It is commonly used as a flight recorder.
 - B. It is the name of the company that first used this technology.
 - C. Its decision-making process is obscured by the thousands of training parameters.
 - D. It is the color of its shipment case.

See online version of this article for a detailed explanation of correct answers.

dermatology communities are fruitfully collaborating to develop novel approaches toward dermatologic diagnosis. However, the use of DL in healthcare practices still requires further substantiation by data and prospective studies to obtain the acceptance of patients and physicians. For this

reason, a careful risk evaluation should be assessed before making publicly available any research tool without a prospective validation (Narla et al., 2018).

ORCID

Marta Cullell-Dalmau: <https://orcid.org/0000-0001-5469-0826>

Marta Otero-Viñas: <https://orcid.org/0000-0003-2718-9977>

Carlo Manzo: <https://orcid.org/0000-0002-8625-0996>

CONFLICT OF INTEREST

The authors state no conflict of interest.

ACKNOWLEDGMENTS

CM gratefully acknowledges funding from FEDER/Ministerio de Ciencia, Innovación y Universidades – Agencia Estatal de Investigación through the “Ramón y Cajal” program 2015 (Grant No. RYC-2015-17896), and the “Programa Estatal de I+D+i Orientada a los Retos de la Sociedad” (Grant No. BFU2017-85693-R) from the Generalitat de Catalunya (AGAUR Grant No. 2017SGR940). CM also acknowledges the support of NVIDIA Corporation with the donation of the Titan Xp GPU. MO-V gratefully acknowledges funding from the PO FEDER of Catalonia 2014-2020 (project PECT Osona Transformació Social, Ref. 001-P-000382) and the Spanish Ministry of Science, Innovation, and Universities through the Instituto de Salud Carlos III-FEDER program (FIS PI19/01379).

AUTHOR CONTRIBUTIONS

Conceptualization: CM, MC-D; Funding Acquisition: CM, MO-V; Supervision: CM, MO-V; Visualization: CM, MC-D; Writing - Original Draft Preparation: CM, MC-D; Writing - Review and Editing: CM, MO-V.

SUPPLEMENTARY MATERIAL

Supplementary material is linked to this paper. Teaching slides are available as supplementary material.

REFERENCES

- Blanco G, Traina AJM, Traina C Jr, Azevedo-Marques PM, Jorge AES, de Oliveira D, et al. A superpixel-driven deep learning approach for the analysis of dermatological wounds. *Comput Methods Programs Biomed* 2020;183:105079.
- Brinker TJ, Hekler A, Utikal JS, Grabe N, Schadendorf D, Klode J, et al. Skin cancer classification using convolutional neural networks: systematic review. *J Med Internet Res* 2018;20:e11936.
- Codella N, Cai J, Abedini M, Garnavi R, Halpern A, Smith JR. Deep learning, sparse coding, and SVM for melanoma recognition in dermoscopy images. In: Zhou L, Wang L, Wang Q, Shi Y, editors. *Machine learning in medical imaging*. Lecture notes computer science series. Cham: Springer International Publishing; 2015. p. 118–26.
- Codella NCF, Gutman D, Celebi ME, Helba B, Marchetti MA, Dusza SW, et al. Skin lesion analysis toward melanoma detection: A challenge at the 2017 International symposium on biomedical imaging (ISBI), hosted by the international skin imaging collaboration (ISIC). In: 2017 IEEE 15th international symposium Biomedicine Imaging (ISBI 2017). New York, NY: IEEE; 2017. p. 168–72.
- Esteva A, Kuprel B, Novoa RA, Ko J, Swetter SM, Blau HM, et al. Dermatologist-level classification of skin cancer with deep neural networks. *Nature* 2017;542:115–8.
- Esteva A, Robicquet A, Ramsundar B, Kuleshov V, DePristo M, Chou K, et al. A guide to deep learning in healthcare. *Nat Med* 2019;25:24–9.
- Fawcett T. An introduction to ROC analysis. *Pattern Recognit Lett* 2006;27:861–74.
- Fujisawa Y, Otomo Y, Ogata Y, Nakamura Y, Fujita R, Ishitsuka Y, et al. Deep-learning-based, computer-aided classifier developed with a small dataset of clinical images surpasses board-certified dermatologists in skin tumour diagnosis. *Br J Dermatol* 2019;180:373–81.
- Fukushima K. Neocognitron: A self-organizing neural network model for a mechanism of pattern recognition unaffected by shift in position. *Biol Cybern* 1980;36:193–202.
- Goyal M, Reeves ND, Davison AK, Rajbhandari S, Spragg J, Yap MH. DFU-Net: convolutional neural networks for diabetic foot ulcer classification. *IEEE Trans Emerg Top Comput Intell* 2018;1–12.
- Haenssle HA, Fink C, Schneiderbauer R, Toberer F, Buhl T, Blum A, et al. Man against machine: diagnostic performance of a deep learning convolutional neural network for dermoscopic melanoma recognition in comparison to 58 dermatologists. *Ann Oncol* 2018;29:1836–42.
- Han SS, Kim MS, Lim W, Park GH, Park I, Chang SE. Classification of the clinical images for benign and malignant cutaneous tumors using a deep learning algorithm. *J Invest Dermatol* 2018a;138:1529–38.
- Han SS, Park GH, Lim W, Kim MS, Na JI, Park I, et al. Deep neural networks show an equivalent and often superior performance to dermatologists in onychomycosis diagnosis: automatic construction of onychomycosis datasets by region-based convolutional deep neural network. *PLOS ONE* 2018b;13:e0191493.
- Hinton GE, Osindero S, Teh YW. A fast learning algorithm for deep belief nets. *Neural Comput* 2006;18:1527–54.
- Litjens G, Kooi T, Bejnordi BE, Setio AAA, Ciompi F, Ghafoorian M, et al. A survey on deep learning in medical image analysis. *Med Image Anal* 2017;42:60–88.
- Lu H, Li B, Zhu J, Li Y, Li Y, Xu X, et al. Wound intensity correction and segmentation with convolutional neural networks. *Concurr. Comput Pract Exp* 2017;29:e3927.
- Marchetti MA, Codella NCF, Dusza SW, Gutman DA, Helba B, Kallou A, et al. Results of the 2016 International Skin Imaging Collaboration International Symposium on Biomedical Imaging challenge: comparison of the accuracy of computer algorithms to dermatologists for the diagnosis of melanoma from dermoscopic images. *J Am Acad Dermatol* 2018;78:270–7.e1.
- Marx V. Machine learning, practically speaking. *Nat Methods* 2019;16:463–7.
- Narla A, Kuprel B, Sarin K, Novoa R, Ko J. Automated classification of skin lesions: from pixels to practice. *J Invest Dermatol* 2018;138:2108–10.
- Navarrete-Dechent C, Dusza SW, Liopyris K, Marghoob AA, Halpern AC, Marchetti MA. Automated dermatological diagnosis: hype or reality? *J Invest Dermatol* 2018;138:2277–9.
- Schmidhuber J. Deep Learning in neural networks: an overview. *Neural Netw* 2015;61:85–117.
- Shenoy VN, Foster E, Aalami L, Majeed B, Aalami O. Deepwound: automated postoperative wound assessment and surgical site surveillance through convolutional neural networks. 2018 IEEE international conference Bioinformatics Biomedicine. New York, NY: IEEE; 2018. p. 1017–21.
- Silver D, Huang A, Maddison CJ, Guez A, Sifre L, Van Den Driessche G, et al. Mastering the game of Go with deep neural networks and tree search. *Nature* 2016;529:484–9.
- Torres R, Judson-Torres RL. Research techniques made simple: feature selection for biomarker discovery. *J Invest Dermatol* 2019;139:2068–74.e1.
- Tschandl P, Codella N, Akay BN, Argenziano G, Braun RP, Cabo H, et al. Comparison of the accuracy of human readers versus machine-learning algorithms for pigmented skin lesion classification: an open, web-based, international, diagnostic study. *Lancet Oncol* 2019;20:938–47.
- Wang C, Yan X, Smith M, Kochhar K, Rubin M, Warren SM, et al. A unified framework for automatic wound segmentation and analysis with deep convolutional neural networks. 2015 37th Annual international conference IEEE engineering in medicine and biology society. New York, NY: IEEE; 2015. p. 2415–8.
- Wehner MR, Levandoski KA, Kulldorff M, Asgari MM. Research techniques made simple: an introduction to use and analysis of big data in dermatology. *J Invest Dermatol* 2017;137:e153–8.
- Yap MH, Goyal M, Ng J, Oakley A. Skin lesion boundary segmentation with fully automated deep extreme cut methods. In: Gimi B, Krol A, editors. *Medical Imaging 2019 Biomedical applications in molecular, structural, and functional imaging*. SPIE; 2019. p. 24.

Glossary

Term	Description
Activation function	A nonlinear function that controls the magnitude of the output signal of a node
Artificial neural network	A brain-inspired computing system that learns to perform tasks by considering examples
Connection	A link between nodes; it transmits the (modified) output signal of a node as the input of another
Convolution	A mathematical operation consisting of the sum of element-wise products between an image and a kernel while shifting one along the other
Convolutional neural network	A class of artificial neural network using the mathematical operation called convolution; they are inspired by the function of the human visual cortex and are well-suited for image analysis
Hidden layer	A layer positioned between the input and the output layer of a network
Kernel	A matrix, generally small, used to extract features from an image through convolution
Layer	A collection of nodes operating simultaneously in the network sequence of tasks
Learnable parameters	Parameters, like weights and biases, that are adjusted during the training process to improve a model
Node, or artificial neuron	The basic unit of a neural network that performs an operation over one or more input signals to produce an output
Stride	The step length in pixels of the kernel shift along the input image during the convolution
Weight	The numerical value associated with a connection that modifies the value of the incoming signal; weights are adjusted during the learning process to strengthen or inhibit specific signals

DETAILED ANSWERS

1. **Which of the following statements about artificial intelligence is FALSE?**

Answer: B. Artificial intelligence and deep learning are not synonyms. Deep learning is a subcategory of machine learning, which in turn is a subcategory of artificial intelligence.

2. **The advantages of convolutional neural networks do NOT include:**

Answer: D. In general, the training is not a very fast process because it requires optimization over a large amount of labeled data, often difficult to obtain.

3. **Which of the following statements about convolutional neural network datasets is TRUE?**

Answer: D. Large labeled datasets are needed to train the great number of parameters of convolutional neural networks. The data are split into three groups and used for training, validation, and testing the model performance.

4. **Which of the following quantities are usually used to evaluate the performance of a classifier?**

Answer: A. The area under the curve of the receiver operating characteristic measures how good a model is in distinguishing between classes.

5. **Deep learning is often dubbed “black box” because:**

Answer: C. The information about the model is encoded inside the values of the weights and is difficult to interpret.

ARTICLE 4. Convolutional Neural Network for Skin Lesion Classification:

Understanding the Fundamentals Through Hands-On Learning

The main objective of this article was to develop a hands-on pedagogical activity that dissected the procedures to train a CNN using a dataset of skin cancer images. This activity was created to support clinicians and medical students in becoming familiar with the working principles of these algorithms and intuitively facilitate their understanding.

The article includes the following: 1) an introduction to DL architectures for the classification of images that have shown outstanding results in a variety of disciplines, including dermatology, and 2) a hands-on pedagogical activity available open source, which execution does not require the installation of software.

The hands-on activity allows the user to dissect the procedures to train a CNN for skin lesion classification providing the scripts, in separated building blocks, with a step-by-step description of the algorithm. In addition, the application allows the visualization and evaluation of the result performed for each block. The code is open source and provided in the Google Colaboratory platform (Colab) for easy execution without any software installation. That network makes it possible to perform the training on GPU on the Colab server, instead of on a particular computer, which could take several days.

The pedagogical activity presented in this article provides accurate explanations and pieces of advice about pre-processing steps, the CNN architecture selection, the training process, and the performance evaluation. In addition, to make this training activity more accessible, we provide instructions to access the ISIC archive of images, which included more than 25,000 images of skin lesions and their verified diagnostic.



Convolutional Neural Network for Skin Lesion Classification: Understanding the Fundamentals Through Hands-On Learning

Marta Cullell-Dalmau¹, Sergio Noé¹, Marta Otero-Viñas², Ivan Meić^{1,3} and Carlo Manzo^{1*}

¹ The QuBI Lab, Facultat de Ciències i Tecnologia, Universitat de Vic – Universitat Central de Catalunya, Vic, Spain, ² Tissue Repair and Regeneration Laboratory, Facultat de Ciències i Tecnologia, Universitat de Vic – Universitat Central de Catalunya, Vic, Spain, ³ University of Zagreb, Zagreb, Croatia

OPEN ACCESS

Edited by:

Je-Ho Mun,
Seoul National University Hospital,
South Korea

Reviewed by:

Luis Puig,
Autonomous University of
Barcelona, Spain
Philippe Lefrançois,
McGill University, Canada

*Correspondence:

Carlo Manzo
carlo.manzo@uvic.cat

Specialty section:

This article was submitted to
Dermatology,
a section of the journal
Frontiers in Medicine

Received: 20 December 2020

Accepted: 10 February 2021

Published: 04 March 2021

Citation:

Cullell-Dalmau M, Noé S,
Otero-Viñas M, Meić I and Manzo C
(2021) Convolutional Neural Network
for Skin Lesion Classification:
Understanding the Fundamentals
Through Hands-On Learning.
Front. Med. 8:644327.
doi: 10.3389/fmed.2021.644327

Deep learning architectures for the classification of images have shown outstanding results in a variety of disciplines, including dermatology. The expectations generated by deep learning for, e.g., image-based diagnosis have created the need for non-experts to become familiar with the working principles of these algorithms. In our opinion, getting hands-on experience with these tools through a simplified but accurate model can facilitate their understanding in an intuitive way. The visualization of the results of the operations performed by deep learning algorithms on dermatological images can help students to grasp concepts like convolution, even without an advanced mathematical background. In addition, the possibility to tune hyperparameters and even to tweak computer code further empower the reach of an intuitive comprehension of these processes, without requiring advanced computational and theoretical skills. This is nowadays possible thanks to recent advances that have helped to lower technical and technological barriers associated with the use of these tools, making them accessible to a broader community. Therefore, we propose a hands-on pedagogical activity that dissects the procedures to train a convolutional neural network on a dataset containing images of skin lesions associated with different skin cancer categories. The activity is available open-source and its execution does not require the installation of software. We further provide a step-by-step description of the algorithm and of its functions, following the development of the building blocks of the computer code, guiding the reader through the execution of a realistic example, including the visualization and the evaluation of the results.

Keywords: convolutional neural networks, skin lesion analysis, classification, melanoma, deep learning

INTRODUCTION: BACKGROUND AND RATIONALE FOR THE EDUCATIONAL ACTIVITY INNOVATION

Over the last two decades, convolutional neural networks (CNNs) (1) have become established as an invaluable tool for biomedical image classification and have been proposed as an instrument for clinical diagnosis in disciplines such as radiology, histology, ophthalmology, and dermatology (2).

The rapid spread of CNNs and other deep learning techniques, has created the need for non-experts to become familiar with these complex tools and understand their principles of

operation. There is a broad literature of introductory articles offering basic reviews on CNNs principles and applications. However, on the practical side, tutorials to start working with CNNs often require a familiarity with terms and concepts that could discourage readers without a solid background in mathematics and/or computer programming to obtain a further understanding of these techniques.

In this scenario, we aim to close this gap by offering a hands-on activity based on the step-by-step execution of a computer code involving all the procedures carried out when implementing a CNN classification, along with their description. Similar educational activities have been recently proposed for other research fields (3). The activity guides the student through two complete examples based on images of skin lesions, starting from the pre-processing of the dataset, and leading through the steps of data augmentation, the choice of the network architecture and its fine-tuning, until the final evaluation of the results.

In our opinion, this hands-on activity can help students to obtain an intuitive understanding of the operations performed by the CNN building blocks, e.g., by visualizing the effect of image convolution with a specific kernel, the feature map generated at specific network layers, or even by performing the network training and exploring the effect of different hyperparameters on the results. The activity can be performed at different levels of difficulty, depending on the user expertise in programming. At the basic level of execution, the students can interactively play with the different sections just by changing input parameters from simple form fields and can run the program by pushing the play button, without even visualizing the code. At the intermediate/advanced levels, students can unfold cells to show, read and (possibly) modify portions of the code. In both cases, the use of the Google Colab and GitHub platforms allows to run the activity in the cloud from any internet browser, without any software installation, strongly simplifying configuration requirements and enabling the capability to use hardware accelerators.

PEDAGOGICAL FRAMEWORK AND LEARNING ENVIRONMENT

We aimed at developing a hands-on activity mainly directed to students (medical school, biomedical engineering), but with the potential of being of interest also for clinicians and other professionals willing to get acquainted with deep learning and CNNs. Four major developments make such a learning-by-doing experience nowadays possible, even for non-experts. First, the creation of specific software libraries, which have reduced the complexity and length of the code necessary to implement these networks, thus allowing their use to operators with a basic knowledge of computer programming. Secondly, the distribution of pre-trained classical CNN under license for reuse has enabled the possibility to perform transfer learning further simplifying the coding and speeding up the training. Third, the free availability of cloud computing on virtual machines with graphics (GPUs) and tensor processing units (TPUs), which has played

an important role in speeding up training procedures. The last development of note is the accessibility of databases containing labeled images for training.

Along these lines, for the proposed activity we use Keras (4), an open-source framework developed by Francois Chollet. Several open-source frameworks are nowadays available for deep learning such as PyTorch or Caffe. However, Keras is recommended for beginners since it is relatively easy to use and has a high-level API that permits to build complex models by writing a few lines of code. In addition, Keras has several models of the best performing architecture (Alexnet, ResNet, VGGNet, Inception, etc.) pre-trained on large datasets (e.g., the one used for the ImageNet Large Scale Visual Recognition Challenge (ILSVRC, <http://image-net.org>) containing millions of photographs from 1,000 categories) that have thus achieved very general classification capabilities. These trained networks can be “reconverted” to the classification of different target images in few simple steps and their learnable parameters (weights and biases) are fine-tuned to provide high classification accuracy, through a procedure called transfer learning.

The code for the activity is provided on the Google Colaboratory platform (Colab, <https://colab.research.google.com/notebooks/intro.ipynb>). Colab is a free cloud service that enable coding in Python and program execution in a web browser, in a highly interactive fashion. In addition, it requires a minimum number of configuration steps, offers free access to GPUs and TPUs, and allows sharing of contents in a straightforward manner. The notebooks and metadata necessary for the activity are shared on GitHub (www.github.com), a free hosting service for software development and version control.

Deep learning requires a massive amount of information in the form of labeled images. Several repositories contain high-quality images associated to dermatology, available as research tools in clinical training and computer science. For example, the archive of the International Skin Imaging Collaboration (ISIC, <https://isic-archive.com/>), or the Edinburgh Dermofit Library (<https://licensing.edinburgh-innovations.ed.ac.uk/i/software/dermofit-image-library.html>) host images of skin lesions, labeled according to their diagnoses. For the activity, we use images from the dataset that has been recently made available for the training of methods competing for the ISIC 2019 challenge (<https://challenge2019.isic-archive.com>), a competition aimed at supporting research toward automated melanoma detection. The full dataset contains 25,331 images of skin lesions associated to 8 different diagnostic categories (melanoma, melanocytic nevus, basal cell carcinoma, actinic keratosis, benign keratosis, dermatofibroma, vascular lesion, and squamous cell carcinoma) and can be accessed by registering to the ISIC website.

DESCRIPTION OF THE HANDS-ON ACTIVITY

The files to perform the activity are stored on the GitHub public repository <https://github.com/qubilab/CNN-for-skin-lesion-classification>. The two links, associated to examples of a binary (benign/malignant) and a multiclass (melanoma/melanocytic

nevus/basal cell carcinoma/actinic keratosis/benign keratosis/dermatofibroma/vascular lesion/squamous cell carcinoma) classification of images of skin lesions, automatically redirect to the respective Colab notebooks.

For the basic use of the notebook, no configuration is needed. For applications requiring hardware accelerators (e.g., training or fine-tuning), GPU or TPU can be enabled by picking the required accelerator from the menu that appears by selecting Runtime/Change runtime type.

For a better pedagogical support, the notebook is organized in consecutive sections, each with a brief explanation of the task performed, that guide the user steps-by-step along the activity. To execute the code in a cell, it is sufficient to select it with a click and then either press the play button within the cell box or use the keyboard shortcut “Command/Ctrl+Enter.” For more advanced applications, the visualization of input form fields or code is achieved by unfolding the cell content, by clicking on the little arrowhead at the left of the cell, thus enabling the necessary editing.

Image Pre-processing and CNN Basics

The first cell “0. Imports” gives access to the code provided in other modules and libraries and defines some basic functions. Once this operation has been performed, we enter into the core of the activity. In fact, since most of the deep learning approaches are data-driven, a major focus must be set on the dataset and its organization. The cell “1. Loading and organizing the dataset” loads the labeled images on the Colab cloud space and arrange them into folders (**Figure 1A**). The first block of this section requires the input of user credential to login on the ISIC archive and the selection of the number of images per category. The photographs will then be organized into folders according to their category and further randomly split into training, validation, and test sets. A variable percentage of images (10–30%) can be used for the final testing, whereas the others are split between training (70–80%) and validation. The folder tree can be visualized in the left frame of Colab, by selecting “Files.” In the example, we use percentages of 65, 20, and 15% of the total number of images for training, validation and test, respectively. These percentages can be changed by the user through the form fields of block 1.3.

The cell “2. Understanding images and convolution” allows the user to visualize an image from a selected folder, together with its decomposition into layers according to RGB color model and the representation of the pixel intensity value. To provide an intuitive understanding of the principle of CNN, the activity shows different convolution kernels and their pixel values. The convolution of the image with these kernels is further provided. An introductory description of the convolution and of the hyperparameters of a convolutional layer can be found in our previous article (5).

Often, the limited amount of data available for training might produce the memorization of specific details of the training images, leading to overfitting and the inability of the model to generalize. In this case, it is recommendable to perform a procedure called data augmentation. The augmentation generates modified images by applying random transformations, such as rotation, shift, scaling, and reflection, to existing

data (**Figure 1B**). Typically, the computer function used for augmentation also takes care of resizing the images to the input size required by the network. These steps can be visualized on a random image by executing the cell “3. Data augmentation.”

CNN Selection

Once the data have been obtained and properly organized, the following step entails the choice of the classification network. In principle, users could build their own network by assembling it layer-by-layer. Application program interfaces allow one to create a CNN from scratch relatively easily. However, this is generally not recommended for beginners, since it requires some background knowledge, a good dose of intuition, and some trial and error. Moreover, unless one is facing a new and very specific image classification task, a personalized CNN is often not needed: many popular deep learning architectures are released under a permissive license for reuse. Even in the case that it is essential to build a custom model, classic networks might still serve as an inspiration, a scaffold, or as a block of the new model. Nowadays, several networks offering outstanding performance for image classification are available, therefore choosing the most suitable CNN for one’s application is not straightforward. Since these CNNs have been originally built for applications on different datasets, the selection should be based on their performance on the target dataset and thus requires their evaluation and comparison (6).

ResNet-50

We use the CNN ResNet-50 (7). ResNet architectures were developed by the Microsoft Research team (7) and are available in several versions with different number of layers, such as 50, 101, 152 (<https://github.com/KaimingHe/deep-residual-networks>). Notably, the ResNet-152 won the 1st places in all the sections of the ILSVRC and COCO (<http://cocodataset.org/#detection-2015>) competitions in 2015. Pre-trained ResNet architectures have been frequently used for the classification of skin lesions, even by several participants to ISIC challenges (8–12).

A schematic representation of the architecture and functions of ResNet-50 is shown in **Figure 2**. **Figure 2A** shows examples of feature maps obtained at specific layers. Moreover, the code of the hands-on activity displays the feature map for any selected layer of the CNN (cell “8.5 Visualize features generated at a specific layer”). **Figure 2B** contains a scheme of the layers and the connections of the network. **Figure 2C** shows the effect of the application of specific operations (convolution, batch normalization, activation and maxpooling) on an image.

As shown in **Figure 2A** and in cell “2. Understanding images and convolution,” an image is a collection of two-dimensional matrices (channels) which elements (pixels) have numeric values representing the brightness in each channel. Color images are composed of multiple channels (e.g., 3 for the RGB representation) whereas grayscale images only have one. The application of the network over an input image, produces its progressive transformation into a larger number of features with smaller lateral dimensions. Eventually, the features are combined to obtain a set of scalar values with the same dimension of the

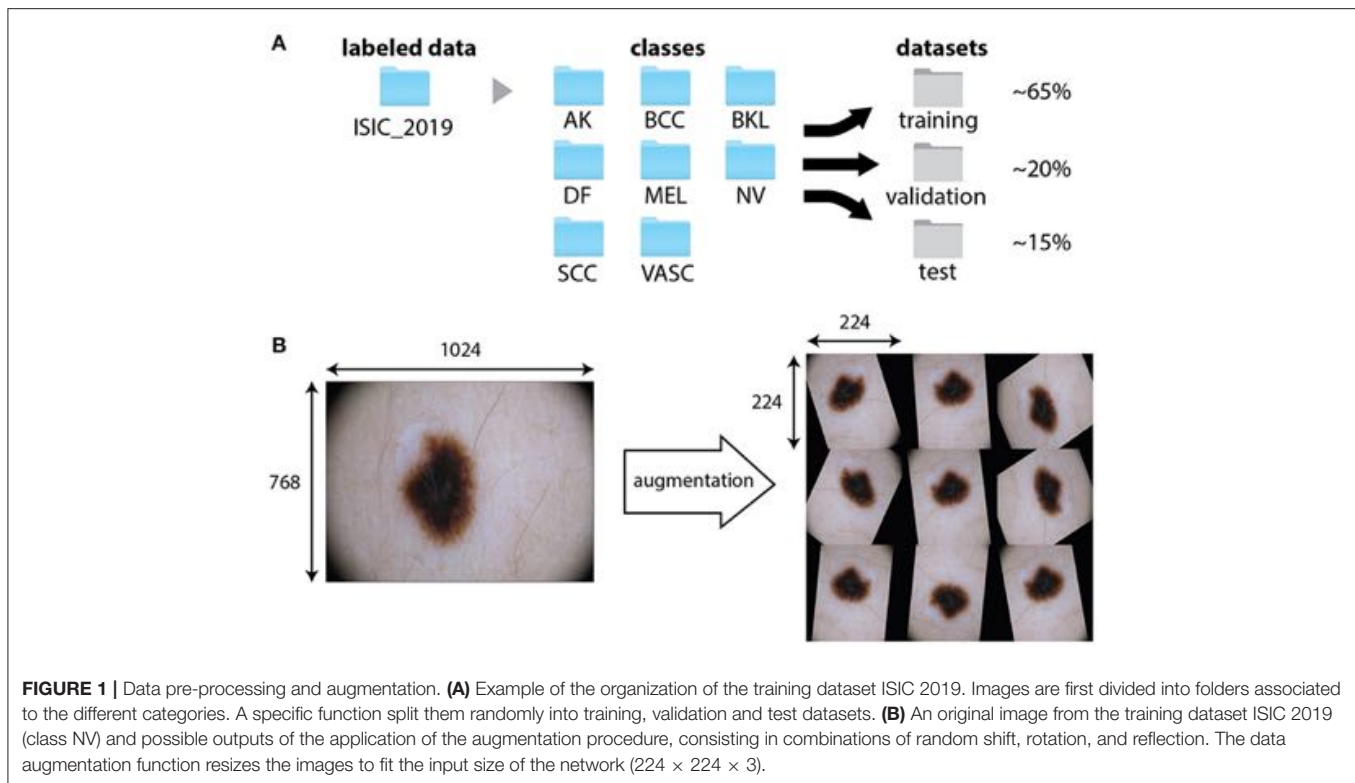


FIGURE 1 | Data pre-processing and augmentation. **(A)** Example of the organization of the training dataset ISIC 2019. Images are first divided into folders associated to the different categories. A specific function split them randomly into training, validation and test datasets. **(B)** An original image from the training dataset ISIC 2019 (class NV) and possible outputs of the application of the augmentation procedure, consisting in combinations of random shift, rotation, and reflection. The data augmentation function resizes the images to fit the input size of the network ($224 \times 224 \times 3$).

output categories. This is achieved through the repetition of mathematical operations performed by the layers and depending on a large number of learnable parameters.

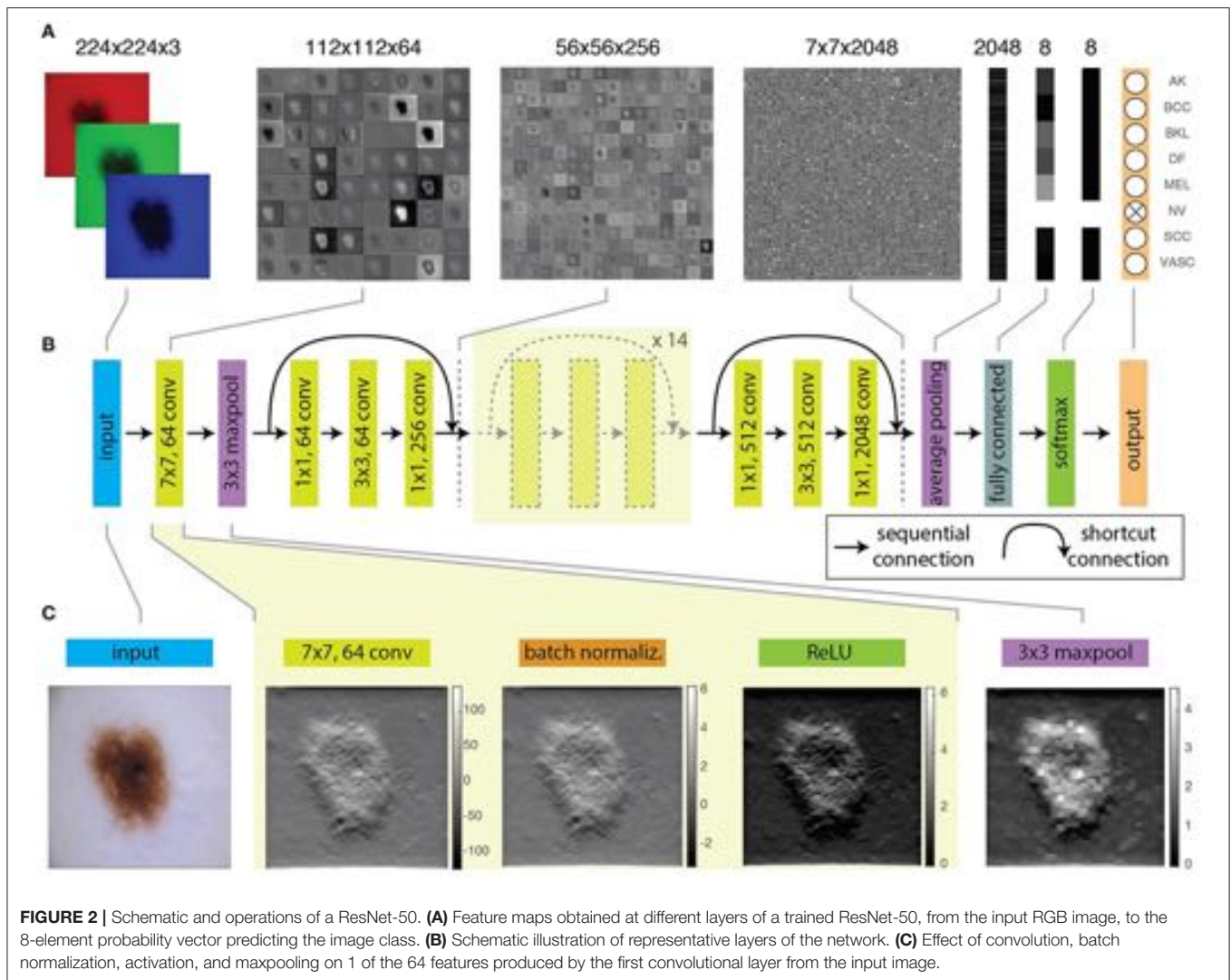
The input is first processed by a convolutional layer. Convolution is a mathematical operation involving the input image and a kernel, typically a matrix with smaller lateral dimensions with respect to the input. During CNN training, kernels are randomly generated and each kernel produces a different feature. Convolution is performed by sequentially shifting the kernel along the input image by a fixed number of pixels, called stride. At each step, the sum of the element-by-element multiplication between overlapping pixels returns the pixel value of the convolutional feature. In cell “2. Understanding images and convolution” the output provided by different kernels can be interactively explored. It must be pointed out that a stride larger than one can be used to obtain features with reduced lateral size with respect to the input.

The first convolutional layer of the ResNet-50 uses 64 kernels of 7×7 pixels² with a stride of 2 pixels and thus produces 64 features with half the lateral size of the input image (Figure 2). The features are regularized through a batch normalization layer (Figure 2C), that performs the standardization of the input, corresponding to the subtraction of the mean of the batch and the division by the standard deviation. The convolutional and batch normalization layers are generally followed by an activation function that performs a non-linear transformation of the feature map, providing the input for the next convolutional layer. Non-linear functions (like sigmoid or hyperbolic tangent) are used as activation functions for their similarity to the behavior of real

neurons, i.e., the transformation of a continuous input into a digital output. The most widely used function is the rectified linear unit (ReLU). The ReLU performs a simple calculation: it returns the same value provided by the input if the input is positive. However, if the input value is negative or null, it returns zero. Inputs that are converted to zero constitute non-activated neurons. In this way, not all neurons are firing simultaneously. The sparse activation and the simpler mathematical operation guarantee a higher computational efficiency for ReLU as compared with other non-linear functions.

The batch normalization and the activation layers preserve the lateral size of features obtained at the output of the convolution layer. However, it is often recommendable to create a lower resolution version (downsampling) of the output image to reduce the number of parameters and account for variations in the position of features in the input image. A common approach is to use a pooling layer, which substitutes adjacent subregions of specific size with the sum, average or maximum values of the corresponding pixels. The ResNet-50 uses a maxpooling layer (Figure 2C) to downsample images by taking the maximum of the input over 3×3 regions.

Combinations of these layers are applied along the network, progressively reducing the lateral size from 224×224 to 7×7 and increasing the depth of the feature map from 3 (the RGB layers of the input image) to 2048. At this point, a group of three layers flattens the feature map, i.e., transforms it into a score vector with the same length as the number of categories. The values of elements of this vector correspond to the probability that the input image belongs to each category (Figure 2B) and



the maximum of this vector will correspond to the category assigned to the input image by the CNN. The first layer of the group performs a downsampling through average pooling, a pooling operation returning the mean of the region of the image considered. By using an average pooling over 7×7 regions, each of the 2048 features is thus reduced to a single value given by the average of all the pixels in the 7×7 map (**Figure 2A**).

The further reduction of the number of elements of the vector to a size equal to the number of categories is obtained through the fully connected layer. Each output value of this layer has a complete connection with all the 2048 inputs, as it is obtained as their weighted sum. The very last layer normalizes these values into the probabilities to belong to each labeled category. Usually, this task is performed through a softmax function that generalizes binary logistic regression to the case of a multiclass problem.

Training

Once the dataset is ready and the CNN has been chosen, it is possible to start the actual training of the network. During

this procedure, values of the learnable parameters are randomly changed, and the corresponding features are calculated to provide a tentative classification of the images in the training set. The performance of the network is evaluated by the calculation of a metric (loss function) that quantifies the similarity between the prediction and the ground-truth. Parameters are iteratively adjusted to optimize the loss function and thus increase correct predictions.

However, as mentioned earlier, we need to distinguish between two different situations. The first refers to the case in which the network needs to be fully trained. In this case, the values of all the parameters of the network need to be learned from scratch. This procedure requires very large datasets, often not available for medical applications. However, the use of a classical network further enables the possibility of performing transfer learning: besides using the same architecture as a classical network, one can also take advantage of parameters learned by the previous training of the CNN on a different, larger dataset. In transfer learning, the parameters obtained from the training

of the model over a large dataset are only fine-tuned to adapt the network for the classification of a different target dataset. In this way, one can skip the time-consuming training steps but still take advantage of the features learned from the training over many photographs. As reported in (6), the top-performing methods submitted for ISIC challenges 2016, 2017, and 2018 used CNNs pre-trained on the ImageNet database. In cells 4–6, we perform these steps using the ResNet-50 pre-trained on the ImageNet dataset.

The ResNet-50 is designed for the ImageNet challenge and thus its output is composed of 1,000 categories. To use the ResNet-50 to classify skin lesion images among a different number of classes, it is first necessary to replace the last layers by ones providing an output over the desired number (2 or 8) of categories (**Figure 2B**). This procedure is performed in the section “4. The CNN: ResNet-50.”

Hyperparameters

The CNN will learn weights and biases by minimizing the loss function over the training set using a method called stochastic gradient descent. However, due to the large size of the dataset and the limited memory, it is not possible to feed all the images simultaneously to the CNN. Therefore, training images are generally passed to the CNN in smaller groups called batches (cell 4.1). The optimum batch size must be set by trial and error in order to provide the fastest convergence. As a rule of thumb, small but not too small batch sizes (e.g., 32, 64, 128) are preferred, since they show higher accuracy than very large batches (13). The number of iterations necessary for the network to “see” the entire training dataset constitutes an epoch.

Another relevant hyperparameter is the global learning rate (cell 5.1), a number between 0 and 1 determining the step size used to update the weights at each iteration. The learning rate sets the speed at which the model is adjusted to the data. A low learning rate applies small changes to the weights at each update, thus requires more epochs of training. Although a high learning rate produces faster changes, if too high it might not converge to an optimal model. The correct learning rate should be empirically chosen to obtain convergence in a reasonable amount of time. Typically, the learning rate is not fixed but is progressively reduced during the optimization. Large rates are first used to quickly obtain values of the weights corresponding to a loss function close to its minimum. At that point, smaller rates further adjust the weights to better approximate the exact minimum of the loss function (cell 5.2). In addition, since in CNN the features provided by the early layers are more generic, whereas those belonging to the last layers are dataset specific, one can introduce non-uniform learning rates and either “freeze” the early layers or train the new layers at a faster rate with respect to the others (cell 5.1 and 5.3). Besides, several other hyperparameters need to be set in relation to the optimization procedure. In the activity, we adopt a procedure and use hyperparameters similar as those described in (11).

Optimization

The algorithm is now ready to start the optimization process, a procedure involving the minimization of a loss function that

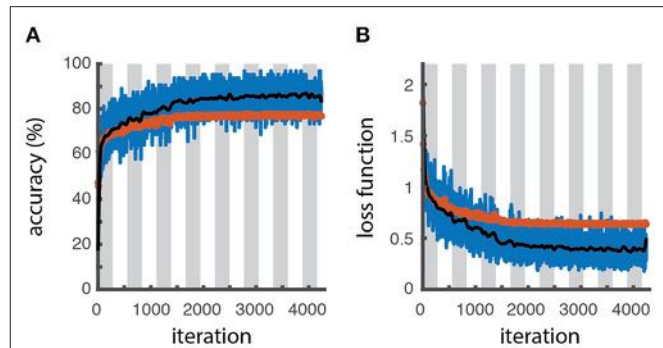


FIGURE 3 | Learning curves. Accuracy (**A**) and loss function (**B**) as a function of the number of iterations for the training batch (blue line for raw data, black line for filtered data) and validation sets (red symbols), as obtained through the optimization procedure. The white and gray areas delimit different epochs. The slightly higher accuracy and lower loss values obtained for the training dataset respect to the validation one reveals a slight overfitting.

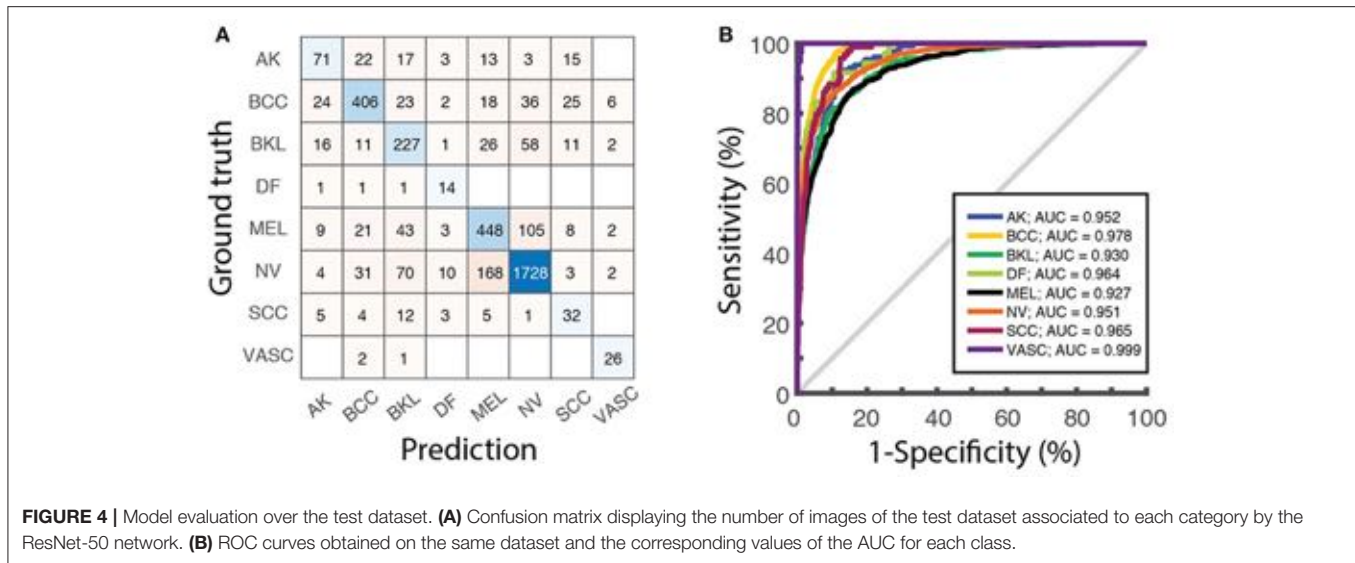
measure the distance between the predicted and the ground-truth classification. For classification tasks, the cross-entropy function is the usual choice (cell 5.4). The optimization will run until some convergence condition is met. This condition is set by the user based either on the value of accuracy/error calculated on the validation set, or on a maximum number of validations without improving the loss value (cell 5.2).

The actual training is performed in section “6. Fine-tuning the model.” The learning process can be visually monitored by displaying the trend of learning curves calculated from both the training and validation datasets as a function of algorithm iterations, to have an idea about how well the model is, respectively, learning and generalizing (defined in cell 5.5). Typically, plots of learning curves associated to optimization (e.g., cross-entropy loss) and performance (e.g., accuracy) are simultaneously created for both datasets (**Figures 3A,B**). The comparison of learning curves obtained for training and validation datasets is a valuable diagnostic method for the model behavior. A training loss showing a continuous decrease with a validation loss showing a minimum, in general correspond to an overfitting model. A good fit is usually associated with training and validation losses decreasing simultaneously toward closely spaced horizontal asymptotes (4). However, a higher accuracy (lower loss) of the training set with respect to the validation can still indicate some degree of overfitting, as obtained for the example shown in **Figures 3A,B**.

Since the training can sometimes run for quite a long time, in section “7. Load a trained network” we also provide a previously-trained model with weights. By loading this model, the user can perform the remaining part of the activity without having to wait for the completion of the training procedure.

Performance Evaluation

Once the learning phase is complete, the network can be finally applied to predict the class of the images contained in the test dataset, that were not used for the training. Since the ground-truth of these images is known, they can be used to calculate



metrics to assess the performance of the classifier (section “8. Performance assessment”). Besides the overall accuracy, the confusion matrix, reporting the number of correct and incorrect predictions over all the classes, (Figure 4A) visually summarize classification and mis-classification performance of the model. The evaluation of the model performance further includes the plot of the receiver operating characteristic (ROC) curves and the calculation of the area under the curve (AUC) for each category (Figure 4B), obtained as detailed in (5).

DISCUSSION AND CONCLUSIONS

We have developed a hands-on activity based on the interactive computer code and a detailed description of the steps needed to implement and fine-tune a CNN to perform the classification of dermatological images, together with an intuitive explanation, suitable for non-experts, of the functions performed by the main blocks of the network. The description is based on two practical examples, consisting of the fine-tuning of a pre-trained ResNet-50 network on a public dataset, containing images of skin lesions corresponding to different diagnoses. The use of *ad hoc* toolboxes and libraries largely simplifies the coding and makes it accessible to beginners.

In our opinion, the hands-on example, together with the description provided in this article, can act as a tool for students interested in obtaining a first understanding of the inner working of a CNN. However, the same activity can also be offered to provide a tutorial for beginners' initiation to computer programming for building and optimizing CNNs. In the first case, the code can be simply executed with the default parameters to visualize the output of each cell. The visualization of the results provides an intuitive understanding of CNN principles. As an example, plotting the feature maps obtained at consecutive layers allows comparing the changes introduced on the features by pooling, batch normalization and activation layers. In the second case, the user can further explore how modifications of the dataset and the change of hyperparameters affect the

network's performance. Examples in this sense might involve the comparison of performance upon the change of learning rates (or even the freezing) of specific layers.

The use of an interactive hands-on activity reproducing a novel approach in its complexity might be a powerful strategy to approach the development of problem-solving and analytical skills, possibly through group work in the classroom. In addition, we believe that making this technology more accessible for non-expert will contribute to further strengthen the collaboration between dermatologists and computer scientists, toward the joint effort of improving image-based medical diagnosis.

AUTHOR CONTRIBUTIONS

CM and MC-D contributed to conception and design of the study. SN, IM, and CM wrote the code and performed analyses. MC-D wrote the first draft of the manuscript. CM wrote the final version of the manuscript. CM and MO-V supervised the research. All authors contributed to manuscript revision, read, and approved the submitted version.

FUNDING

CM gratefully acknowledges funding from FEDER/Ministerio de Ciencia, Innovación y Universidades – Agencia Estatal de Investigación through the Ramón y Cajal program 2015 (Grant No. RYC-2015-17896), and the Programa Estatal de I+D+i Orientada a los Retos de la Sociedad (Grant No. BFU2017-85693-R); from the Generalitat de Catalunya (AGAUR Grant No. 2017SGR940). CM also acknowledges the support of NVIDIA Corporation with the donation of the Titan Xp GPU. MO-V gratefully acknowledges funding from the PO FEDER of Catalonia 2014-2020 (project PECT Osona Transformació Social, Ref. 001-P-000382) and the Spanish Ministry of Science, Innovation, and Universities through the Instituto de Salud Carlos III-FEDER program (FIS PI19/01379). IM acknowledges the support of the Erasmus+ program of the European Union.

REFERENCES

1. LeCun Y, Haffner P, Bottou L, Bengio Y. Object recognition with gradient-based learning. In: *Shape, Contour and Grouping in Computer Vision Lecture Notes in Computer Science, vol 1681*. Berlin; Heidelberg: Springer (1999). p. 319–45. doi: 10.1007/3-540-46805-6_19
2. Litjens G, Kooi T, Bejnordi BE, Setio AAA, Ciompi F, Ghafoorian M, et al. A survey on deep learning in medical image analysis. *Med Image Anal.* (2017) 42:60–88. doi: 10.1016/j.media.2017.07.005
3. Erickson BJ. Magician's corner: how to start learning about deep learning. *Radiol Artif Intell.* (2019) 1:e190072. doi: 10.1148/ryai.2019190072
4. Chollet F. *Deep Learning with Python*. Shelter Island: Manning Publications Company (2018).
5. Cullell-Dalmau M, Otero-Viñas M, Manzo C. Research techniques made simple: deep learning for the classification of dermatological images. *J Invest Dermatol.* (2020) 140:507–14.e1. doi: 10.1016/j.jid.2019.12.029
6. Perez F, Avila S, Valle E. Solo or ensemble? Choosing a CNN architecture for melanoma classification. In: *Proceedings of the IEEE Conference on Computer Vision and Pattern Recognition Workshops*. Long Beach, CA (2019).
7. He K, Zhang X, Ren S, Sun J. Deep residual learning for image recognition. *Proc IEEE Comput Soc Conf Comput Vis Pattern Recognit.* (2016) 2016-Decem:770–8. doi: 10.1109/CVPR.2016.90
8. Gutman D, Codella NCF, Celebi E, Helba B, Marchetti M, Mishra N, et al. Skin lesion analysis toward melanoma detection. In: *A Challenge at the International Symposium on Biomedical Imaging (ISBI) 2016, hosted by the International Skin Imaging Collaboration (ISIC)* (2016). Available online at: <https://arxiv.org/abs/1605.01397>
9. Marchetti MA, Codella NCF, Dusza SW, Gutman DA, Helba B, Kallou A, et al. Results of the 2016 international skin imaging collaboration international symposium on biomedical imaging challenge: comparison of the accuracy of computer algorithms to dermatologists for the diagnosis of melanoma from dermoscopic images. *J Am Acad Dermatol.* (2018) 78:270–7.e1. doi: 10.1016/j.jaad.2017.08.016
10. Codella NCF, Gutman D, Celebi ME, Helba B, Marchetti MA, Dusza SW, et al. Skin lesion analysis toward melanoma detection: a challenge at the 2017 International symposium on biomedical imaging (ISBI), hosted by the international skin imaging collaboration (ISIC). In: *2018 IEEE 15th International Symposium on Biomedical Imaging (ISBI 2018)*. New York, NY: IEEE (2018). p. 168–72.
11. Han SS, Kim MS, Lim W, Park GH, Park I, Chang SE. Classification of the clinical images for benign and malignant cutaneous tumors using a deep learning algorithm. *J Invest Dermatol.* (2018) 138:1529–38. doi: 10.1016/j.jid.2018.01.028
12. Codella N, Rotemberg V, Tschandl P, Celebi ME, Dusza S, Gutman D, et al. Skin lesion analysis toward melanoma detection 2018. In: *A Challenge Hosted by the International Skin Imaging Collaboration (ISIC)*. Washington, DC (2019).
13. Mishkin D, Sergievskiy N, Matas J. Systematic evaluation of convolution neural network advances on the Imagenet. *Comput Vis Image Underst.* (2017) 161:11–9. doi: 10.1016/j.cviu.2017.05.007

Conflict of Interest: The authors declare that the research was conducted in the absence of any commercial or financial relationships that could be construed as a potential conflict of interest.

Copyright © 2021 Cullell-Dalmau, Noé, Otero-Viñas, Meiç and Manzo. This is an open-access article distributed under the terms of the Creative Commons Attribution License (CC BY). The use, distribution or reproduction in other forums is permitted, provided the original author(s) and the copyright owner(s) are credited and that the original publication in this journal is cited, in accordance with accepted academic practice. No use, distribution or reproduction is permitted which does not comply with these terms.

Chapter 4.

Discussion

VEGF-A differentially influences fibroblast migration and receptor spatiotemporal organization as a function of cell density (*article I*)

The study of the cellular and molecular mechanisms altered in chronic wounds has advanced in the last decades with good clinical results. However, some unknown mechanisms could explain the persistence of some kinds of chronic wounds. In our *Article I*, we focused on the understanding of the VEGF-A role in dermal fibroblast activity because it is one of the most enriched growth factors in currently employed biological therapies. For years, the VEGFR-1 was considered a decoy receptor, but more recent results suggest it has other signaling functions⁸².

For sparse fibroblasts, we found that VEGF-A increases the migration speed while decreasing directional persistence. We expected the decrease of the directional persistence as VEGF-A artificially added masks natural gradients of VEGF expressed by other fibroblasts guiding the cell migration. Surprisingly, the VEGF-A effect in high cell density conditions is the opposite. Both results are consistent with the regulation of the Hippo pathway which controls the expression of YAP and TAZ transcriptional coactivators promoting cell migration⁸³.

At the molecular level, we have described for the first time the lateral diffusion of VEGFR-1 at the single-molecule level. The study of VEGFR-1 and integrin $\alpha_5\beta_1$ density and spatiotemporal organization show differences depending on the cell density and fibroblast phenotype, contributing new evidence of the recently discovered feed-forward loop of the Hippo pathway⁸⁴.

New tools to obtain quantitative values of wound healing evolution and to assess the efficacy of therapies in chronic wounds (*article II*)

Monitoring the evolution of chronic wounds is a complex process, even for experienced healthcare staff. An efficient wound healing follow-up requires paying attention to several clinical variables: 1) descriptive parameters (color or exudate presence) and 2) quantitative variables (wound area and shape) to also guarantee an objective monitoring process. Because the planimetry technique is still common in wound clinical units, we have developed a graphic user interface for wound area and shape descriptors measurements (Woundaries) based on the planimetry methodology. Our tool is easy to use, and practical since it allows different forms of planimetry digitalization, like scanning or photographing. The Woundaries tool can detect the area inside the wound perimeter also in the case of partially open wound contours, avoiding the need for tracing again the contour after wound image digitalization. Area values, together with the other wound descriptors provided by the Woundaries, can be further analyzed to determine wound evolution values with prognostic applications⁸⁵.

Our classification routine has several advantages in comparison with others previously reported. First, the determined characteristic healing time is a measure independent of the initial wound extent, being a more robust parameter than total healing time. Secondly, our routine can automatically determine if the wound healing process follows a simple exponential decay model or a mixed model, which is a wound with a delayed start of healing. In agreement with other authors⁸⁶, we observed that some wounds show a delayed start of healing, and our tool is able to automatically detect this behavior which increases the robustness of our method. And finally, the obtained characteristic healing time has prognostic value allowing clinicians to identify wounds with a bad prognostic after only 5 weeks. This earlier prognosis determination

will be very useful for healthcare staff to consider changing wound treatment to a more appropriate one⁸⁷.

In addition, we tested our methodology to compare the efficacy of an autologous therapy with conventional therapies. The characteristic healing time values resulted in enough sensitivity to observe statistically significant differences among sexes and etiologies in response to the analyzed therapy. We are convinced that the use of these metrics for testing the efficacy of new therapies can lead to more efficient use of complex or expensive therapies, especially in cases that require blood extraction and processing, applying them to those patients who would really benefit from them.

Our tools have improved the existing methods to support clinicians in better decision-making to treat chronic wounds. In fact, nowadays, the complete healing time, which is highly influenced by the initial area, is the healing parameter used and accepted by medical agencies like FDA. If the use of the characteristic healing time is broadly adopted, it would result in a more objective metric and will lead to more efficient chronic wound treatment, reducing medical costs and inconveniences for patients.

Improving knowledge and access to use of artificial intelligence (AI) for skin lesions classification (*articles III-IV*)

Although the above-mentioned tools for wound follow-up have been very useful, we observed that they can result in laboriousness, especially in chronic-wound units that treat a lot of ulcers every day. For that reason, we decided to explore the state of the art of using artificial intelligence algorithms in assisting diagnostics in dermatology. Among the different subcategories of AI, machine learning (ML) and deep learning (DL) have demonstrated the capability to achieve great results in the classification of skin lesions based on images. We soon realized there was a lack of a big data set of standardized ulcer images and diagnostics, an essential element for the training of DL algorithms. With the SARS-CoV-2 pandemic heavily pressurizing the healthcare system, it was impossible to collect such a data set of images during this thesis. For that reason, we decided to study and tune our DL algorithm in the context of cancerous skin lesion classification, a dermatological area where DL has been tested for years⁷⁶.

We realized that the literature about DL applied to dermatology is, in general, explained in a very technical language, making its understanding very difficult for non-experts in this area. So, we focused our first review article on comprehensively explaining this technology to approach this technology to the end users, the clinicians. We centered our efforts on the use of comprehensive vocabulary and the creation of figures that visually help to comprehend these advanced methods. In the same way, we also supplemented our paper with some slides and a short multiple-choice test that can be downloaded from the online version and used for teaching purposes. After explaining each part of those algorithms and the main operations performed, we

dedicated a section to emphasizing the benefits but also the possible risks of this technology, and the main tests to detect possible bad performance.

We focused our second review article on the creation of a hands-on tool to allow students and clinicians to interact with the DL algorithm. Based on the learning-by-doing philosophy we divided the code into blocks with a brief explanation in each of them, allowing the user to see the code, execute it, and test the effect in the final output. Also, more advanced users are encouraged to change some hyperparameters to visualize their effect in the final output. As an end user, seeing the results of the intermediate steps of a DL algorithm is an important way to learn while experimenting with the code. Again, in this review, we emphasize the importance of proper training and the performance evaluation metrics and plots that will help the user to detect the performance level of the tested configuration.

Considering together the first article of this series, introducing DL technology, its main parts and operations, and the second article, allowing non-experts to get a deeper comprehension while applying the example algorithm on a real data set of skin lesions images, we are convinced that we have made a significant contribution to make this emerging AI technology more comprehensive and accessible to non-experts.

Chapter 5.

Conclusions

- From article I: “*VEGF-A differentially influences fibroblast migration and receptor spatiotemporal organization as a function of cell density*” we can conclude:

There is a complex relationship between cell density, cell damage signaling, receptor-ligand interactions, and spatiotemporal organization of VEGFR-1 and integrin $\alpha_5\beta_1$, which determines fibroblast behavior in migration and affects the wound healing process.

- From article II: “*A toolkit for the quantitative evaluation of chronic wounds evolution for early detection of non-healing wounds*” we can conclude:

We provide new tools to assist healthcare staff in monitoring the wound healing process for improving clinical decision-making in chronic wound management and early prediction of non-healing wounds. This is a reliable and user-friendly method for the quantification of area and shape descriptors from digitalized hand-traced planimetry that provides information on wound healing evolution and estimates the kinetic parameters of the process.

- From article III: “*Research Techniques Made Simple: Deep Learning for the Classification of Dermatological Images*” we can conclude:

We describe the necessary concepts for clinicians to approach DL algorithms applied to dermatology, detailing their structure, basic processes, and performance evaluation in an understandable way for non-experts in the area.

- From article IV: “*Convolutional Neural Network for Skin Lesion Classification: Understanding the Fundamentals Through Hands-On Learning*” we can conclude:

We provide a hands-on activity and a detailed description of the steps needed to run and fine-tune a CNN to perform the classification of dermatological images. This pedagogical activity introduces dermatologists and medical students to these technologies and contributes to strengthening the collaboration between doctors and computer scientists, to improve image-based medical diagnosis.

Conclusion

Working from a multidisciplinary perspective allows us to improve the comprehension of wound care by understanding the molecular and cellular mechanisms involved in wound healing and introducing new technologies to support clinical decision-making.

Limitations of this doctoral thesis

This thesis has produced new tools and provided evidence of the benefits of using wound healing monitoring aids for improving daily chronic wound management. However, the research included in this doctoral thesis has several limitations:

- The assessment of the clinical tools developed in the context of this thesis for identifying wound healing prognosis was only validated using the most common wounds. Therefore, new studies should be performed using less usual wound etiologies to test the fit and performance of characteristic healing time in this group of wounds. For that purpose, cooperation with different hospitals to increase wound data would be necessary.

- Our methodology for wound area measurement is time-consuming as it includes several steps: drawing the planimetry, digitalizing it, and performing the measurement. Additionally, healthcare staff must spend extra time to perform the fit and obtain the characteristic healing time. That is a relevant limitation of our methodology, especially to be used in clinical wound units where nurses must visit dozens of patients with chronic wounds every day. Therefore, it may be difficult to appreciate the benefits of investing this time, particularly if it leads to longer waiting times for patients.

- We found that the healthcare staff generally had a low background in mathematics and programming, which posed an additional barrier to using our methodology in its current structure. Additionally, computers in hospitals and primary health care centers are strongly protected and installing new software may require numerous permissions and licensing costs.

To address these limitations, we explored the implementation of AI algorithms to create more user-friendly wound-monitoring software. However, we encountered

new limitations concerning the lack of a public database with ulcer images and their classification for training the AI algorithms.

Outlook and future plans

To address the limitations of our tools for wound healing monitoring and prognostic evaluation previously described, we propose integrating these tools into a tablet application. This technological integration would simplify the process, starting with the capture of wound or planimetry photographs using the tablet camera. However, a collaborative agreement with other specialists will be needed since our research team doesn't have the expertise to develop this technological device. In addition, we strongly believe that the application of AI in the wound healing management fields holds promise. However, the development of a complete wound image and classification repository is needed before testing our algorithm architecture in this area.

On the other hand, our study of the VEGF effect on dermal fibroblast activity is just scratching the surface and will require a deeper investigation for a better understanding of the cellular and molecular mechanisms involved. We plan to use dual-color single-molecule localization microscopy to study the organization of receptors and obtain a clear image of the distribution and clustering of the integrin $\alpha_5\beta_1$ and the VEGFR-1 with VEGF treatment, concerning cell density. Furthermore, we are interested in performing other assays to analyze the effect of VEGF in other skin cells like keratinocytes which have also an essential role in good wound healing resolution. Given the strong effect of cell density in VEGF migration regulation observed in this doctoral thesis, we plan to further investigate the involvement of cell-cell interactions and the role of the Hippo pathway control mechanism.

Appendix 1.

Molecular techniques

Antibody reduction

Briefly, 0.05mg of the mouse anti-human integrin α_5 (BD Pharmingen, 555651) and VEGF Receptor 1 rabbit anti-human antibody (SY09-09, Invitrogen) were dialyzed (Slide-A-Lyze MINI Dialysis Device, 2K, Thermo Fisher) in PBS for 4h at room temperature to remove the commercial buffer. Then the antibody was reduced with 1 mM DTT (dithiothreitol) for 30 min at room temperature and purified from DTT via dialysis as mentioned before. To avoid reassociation of the reduced Abs, sulfhydryl groups were blocked with 20mM of iodoacetamide for 1 hour at 4 °C. Then iodoacetamide was removed from the reaction solution by dialysis. To check the result of the digestion process 10ul of each reduced antibody was mixed with an equal amount of 2X nonreductive sample buffer and directly loaded in an SDS-Page gel with 8% polyacrylamide (detailed in the next section).

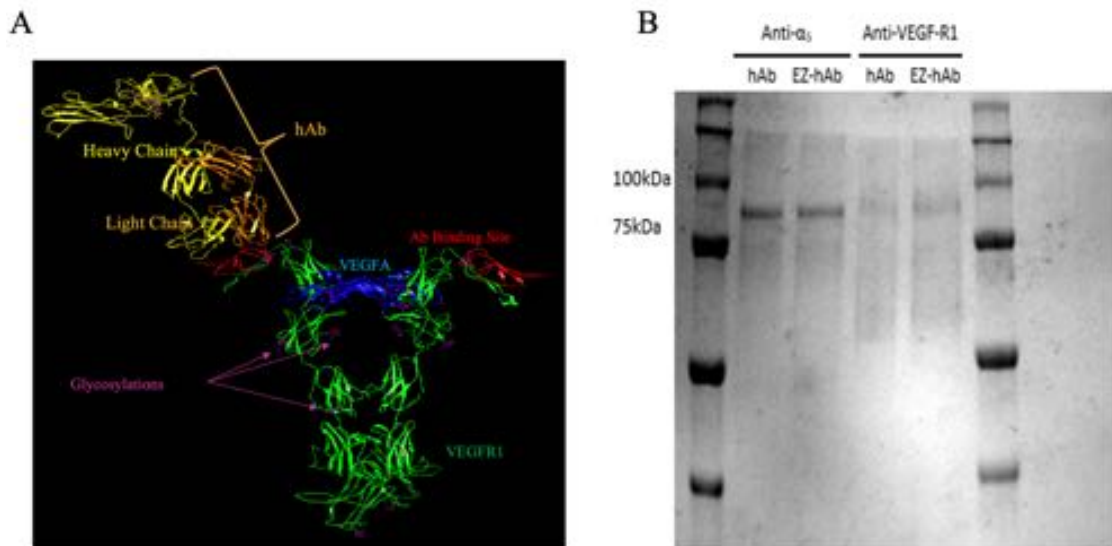


Figure I. 3D representation of half antibody fragment interaction site prediction and reduction testing.

A) Representation of crystallized structures of VEGFR-1⁸⁸ (PDB: 5T89) in green and a generic half IgG⁸⁹ (PDB: 1Igy) in yellow and orange. Red color marks the binding site reported in the commercial antibody SY09-09 (Thermo Fisher) technical sheet and in blue the vascular endothelial growth factor in his binding site. B) Image of the gel testing the result of the antibodies digestion process. For each antibody, we tested the half antibody fragment after the digestion process (hAB) and after the digestion and the biotinylation process (EZ-HAb). The half antibody fragment (75-kDa+ glycosylation's weight) is present in both antibodies while the full antibody fragment (150kDa) is indistinguishable. Own source.

Sodium dodecyl sulfate-polyacrylamide gel electrophoresis (SDS-PAGE)

Gels were prepared at 8% acrylamide/bisacrylamide for the resolving gel and 4% for the stacking gel. The samples after the reduction process and the biotinylation process (detailed in the next section), were mixed with 2x non-reducing buffer, heated at 95°C for 10 min, and loaded in the gels. Gels were run at 35mA per gel. The running buffer was Tris 25mM, glycine 192mM, and SDS 0,1%. Proteins were separated according to their molecular weight until the front of the electrophoresis reached the

bottom of the gel. After running the gel was stained with Coomassie stained and imaged on a Versadoc scanner (Versadoc 4000MP, Bio-Rad) (Figure I-B).

Half antibody fragment biotinylation and conjugation with quantum dots (QD)

To use the reduced antibody for single particle tracking is necessary to biotinylate and conjugate them with quantum dots. The antibody biotinylation was performed following the commercial protocol, with a 10-fold molar excess of EZ-Link Sulfo-NHS_{LC} Biotin (Thermo Fisher, A39257) for 30 min at room temperature under movement. This reaction adds biotins to the side chain of lysine and at the N-terminus of the polypeptides.

Once biotinylated, the half antibody fragments are ready to be conjugated with quantum dots₆₅₅ streptavidin conjugates (Thermo Fisher Q10123MP). To perform the reaction and get the desired proportion of 1 QD for each half antibody fragment we perform the reaction with 1hAb:1QD:10 D-biotin (Thermo Fisher D1595) molecules proportions, where biotin is used to compete for the binding in 10-fold higher concentration. Three final 200 μ l solutions a) hAb fragments at 20mM, b) D-biotin at 200mM, and c) quantum dots at 20mM, all of them diluted in PBS with 6% of BSA were finally joined and incubated together for 2 hours at 4°C in an orbital tray.

Appendix 2.

Wound healing and single particle tracking experiments

In this Appendix 2, we detail the methodologies used to analyze the fibroblast migration data obtained in this thesis. We describe the processes and equations used for cell migration quantification and for describing the motion of cell membrane receptors.

Diffusion measurements

Diffusion measurements are applied similarly to study individual cell migration behavior or membrane protein diffusion, with the unique difference of the scale of distances and time. For cells moving in a 2D plane, the diffusivity measures to get the rate at which cells spread from the initial position. This is a time-consuming technique, so it is recommended to use software to automatically detect the precise localization of all objects (cells or labeled proteins) in all frames matching the expected cell or particle radius (Figure II-A) and then connect all the localizations in tracks (Figure II-B).

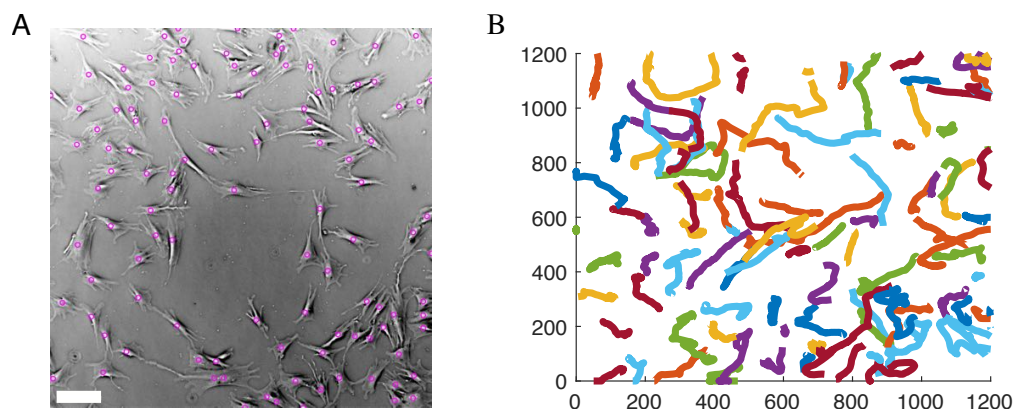


Figure II. Cell tracking detection and tracks resulting after a single localization connection.

A) Example of a phase contrast image at low cell density for individual fibroblast migration assays. Magenta circles show the bright spots (cells) detected in that frame by the tracking software TrackMate⁹⁰. Scale bar = 150 μ m. B) Plot of the trajectories resulting from the detection and connection of all cell positions in each frame during 24h for the same field of view. Own source.

The main equation used to determine single-cell or single-protein diffusion is the mean-squared displacement (MSD) given in Equation 1, which describes the average extent of space explored by a cell or a particle as a function of different time intervals (also called time lag “ t_{lag} ”). For a single particle j moving in 2D, MSD is calculated by determining their position coordinates $\mathbf{x}_j = \{x_j, y_j\}$ sampled at N discrete times $m\Delta t$ (Figure III-A). MSD can be used to characterize the mode of motion^{91,92}.

$$MSD(t_{lag} = m\Delta t) = \frac{1}{N - m} \sum_{i=1}^{N-m} [x_j(t_i + m\Delta t) - x_j(t_i)]^2$$

Equation 1.

In Figure III-B we can observe an exemplary MSD plot. While increasing t_{lag} , MSD data points result in more scattered and less statistically significant⁹¹ for the calculation of diffusion parameters. For this reason, the fitting used is performed over a limited number of points having larger statistics, usually the first 4 or 6 points. Therefore, only trajectories having a minimum length of at least 20 points are typically used, causing the rejection of a great number of shorter trajectories. To determine the effective diffusion coefficient also from short trajectories, Jaqaman and colleagues developed an alternative method (Equation 2). This calculation uses frame-to-frame squared displacement (r^2) and localization precision σ averaged over all frames of the track⁹³ (<https://github.com/kjaqaman/diffModesF2F>).

$$D = \frac{r^2}{4} - \sigma^2$$

Equation 2.

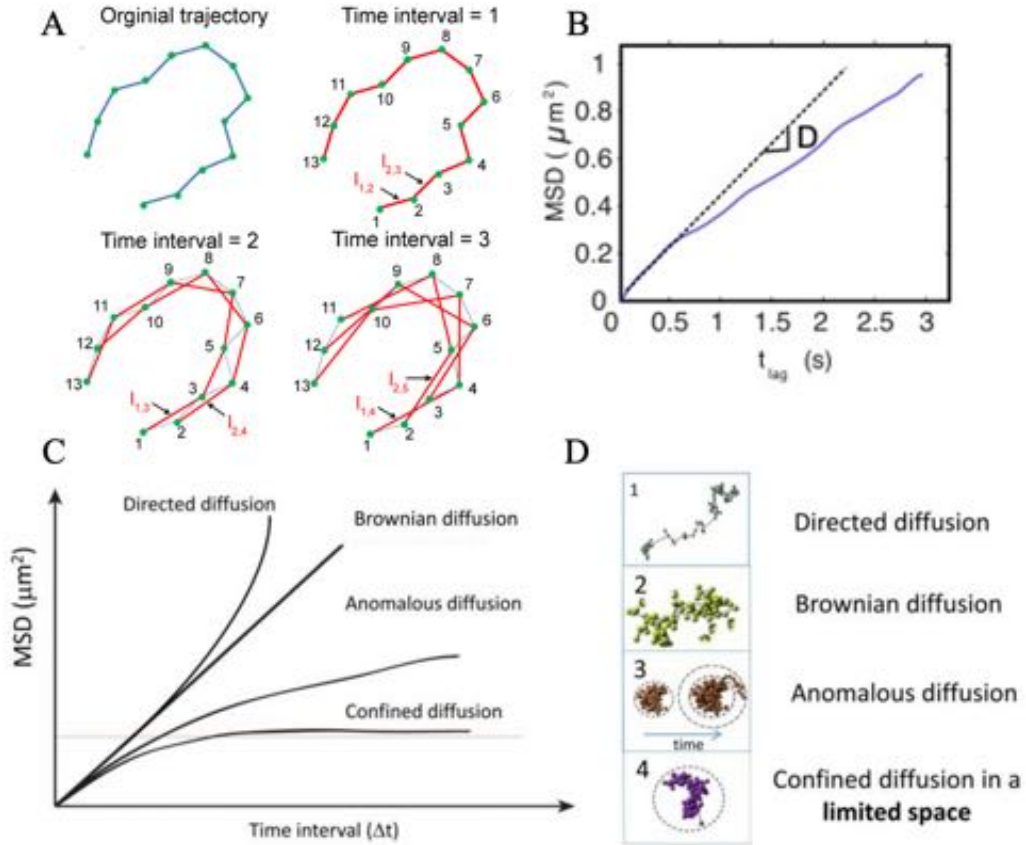


Figure III. Diffusion calculation and trajectory types.

A) 2D trajectory example showing different time intervals (t_{lag}). Adapted from Ref. ⁹⁴.
 B) MSD plot at different t_{lag} for a 2D trajectory. The dotted line shows the linear fit over the first 4 points to get the slope or the diffusion coefficient. Own source. C) MSD plot of representative different types of motion. D) Examples of different types of trajectories. Adapted from Ref. ⁹⁵.

As it can be appreciated in Figure III-C and D, a pure random walk like Brownian motion produces a straight line in an MSD plot as given by Equation 3, where d represents the dimensionality of the space in which the motion takes place (2 for a 2D motion) and D is the diffusion coefficient.

$$MSD(t_{lag}) = 2dDt_{lag}$$

Equation 3.

If the diffusing particle finds obstacles, the diffusion shows an anomalous behavior, characterized by Equation 4, where k is a generalized diffusion constant and

α is the anomalous exponent. This exponent can indicate a sub-diffusive behavior if $\alpha < 1$ or a super-diffusive behavior if $\alpha > 1$.

$$MSD(t_{lag}) = 2dKt_{lag}^{\alpha}$$

Equation 4.

Less frequent but also present are those trajectories showing directed motion behavior. This can be defined as straight-line particle motion and is sometimes observed for active transport events along microtubules or molecular motors⁹⁶. For a 2D diffusion, directed motion is defined by Equation 5.

$$MSD(t_{lag}) = 2dDt_{lag} + (vt_{lag})^2$$

Equation 5.

The cell membrane is a very complex environment, containing physical links with extracellular components like glycocalyx and ECM components and with intracellular elements like cytoskeleton elements like actin or intracellular signaling proteins. For that reason, it is common to observe trajectories confined in some regions, with an MSD curve fitting Equation 6, where a_1 and a_2 are positive constants related to the geometry of the region and R is proportional to the size of the confinement region. Finally, trajectories with $R=0$ are defined as immobile⁹².

$$MSD(t_{lag}) = R [1 - a_1 e^{(-2a_2 4Dt_{lag}/R)}]$$

Equation 6.

Methods based on the mean-squared displacement are mostly limited to quantitative analysis of particles that exhibit a unique behavior over time. To detect switching from one behavior to another, which is very common in most biological systems, other approaches are necessary. One of these alternatives is to perform segmentation using other diffusion estimators as, for example, the moment scaling spectrum (MSS). For this analysis, the moments of order p of the distribution of

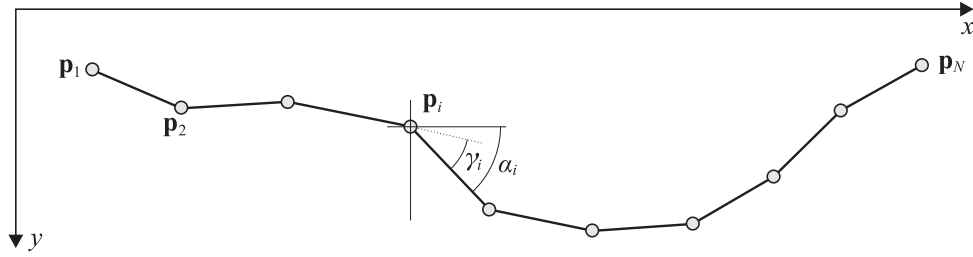
displacements are calculated according to Equation 7, where N is the number of trajectories, T_n is the duration of trajectory n , t_{lag} is the time step, $x_n(t)$ is the position of the n^{th} particle at time t , and p is the moment order⁹⁷.

$$\langle |x|^p \rangle(\tau) = \frac{1}{N} \sum_{n=1}^N \sum_{t=1}^{T_n - t_{lag}} |x_n(t + t_{lag}) - x_n(t)|^p$$

Equation 7.

In contrast to MSD-based methods, which use only the second moment ($x^2 \sim t_{lag}$ with x position and t_{lag} time step) MSS utilizes higher-order moments⁹¹. This means that $x^p \sim t_{lag}^{\gamma_p}$, where the plot of the moment exponents γ_p versus p gives the MSS. The slope of the MSS, denoted as S_{MSS} , indicates the motion type of the track segment, where $S_{MSS} = 0.5$ represents pure diffusion, $0 < S_{MSS} < 0.5$ represents restricted motion, and $0.5 < S_{MSS} < 1.0$ represents directed motion^{97,98}.

With the trajectory information, it is also possible to extract other measures for understanding cell or protein behavior. In our case, we decided to explore deeply the dermal fibroblast behavior, due to their peculiarities. As seen in the introduction Section 2 fibroblast migration is driven by cell polarization, which depends on extracellular signaling but also is influenced by extracellular matrix composition and organization. To understand better this behavior, we also calculated the distribution of the turning angle. As seen in Figure IV, the turning angle (γ_i) describes the propensity of a moving object to change direction at each step⁹⁹. This quantity, used on sparse cells, is useful to understand if cells move randomly or if they temporarily follow a preferred direction. In relation to this measure, we also determine the motile persistence considering the end-to-end displacement divided by the total displacement.



Measure	Definition
Instantaneous angle	$\alpha_i = \arctan(y_{i+1} - y_i)/(x_{i+1} - x_i)$
Instantaneous speed	$v_i = d(\mathbf{p}_i, \mathbf{p}_{i+1})/\Delta t$

Figure IV. Summary of other measures on individual trajectories.

Top: schematic representation of sample trajectory consisting of N points $\mathbf{p}_i = (x_i, y_i)$. Bottom: table summarizing other measures applied to trajectories assuming constant time interval Δt between successive frames. Adapted from ref.⁹⁹.

We also compute the instantaneous velocity as the displacement from one frame to the next divided by the time interval (Figure IV)⁹⁹. This is also necessary to understand if cells move at different velocities while increasing the experimental time. With all the instantaneous velocities for the same trajectory, we can also get a mean instantaneous velocity for that trajectory.

Quantification of collective cell migration

In vitro wound healing assay is a widely used technique to assess drug testing effects on cell migration. Automated microscopes with incubation chambers have converted this technique into a reproducible and easy-to-perform procedure. This technique aims to quantify the collective cell migration kinetics to obtain quantitative value and statistically determine the effect of a concrete drug or therapy on cell

migration⁴⁶. Hundreds of time-series images must be processed to calculate the remaining gap area in each frame, which is the wound area. This analysis is a time-consuming process¹⁰⁰ that can be done using different public or custom software based on different processes. Some of these software tools are based on automated image segmentation¹⁰¹. We created a custom script adapting the algorithm described in Ref.¹⁰². In Figure V-A, time-lapse images of a scratch assay taken at different times with an automated microscope are shown together with the mask transformation performed by our custom script (Figure V-B) to automatically measure the free area of the field of view.

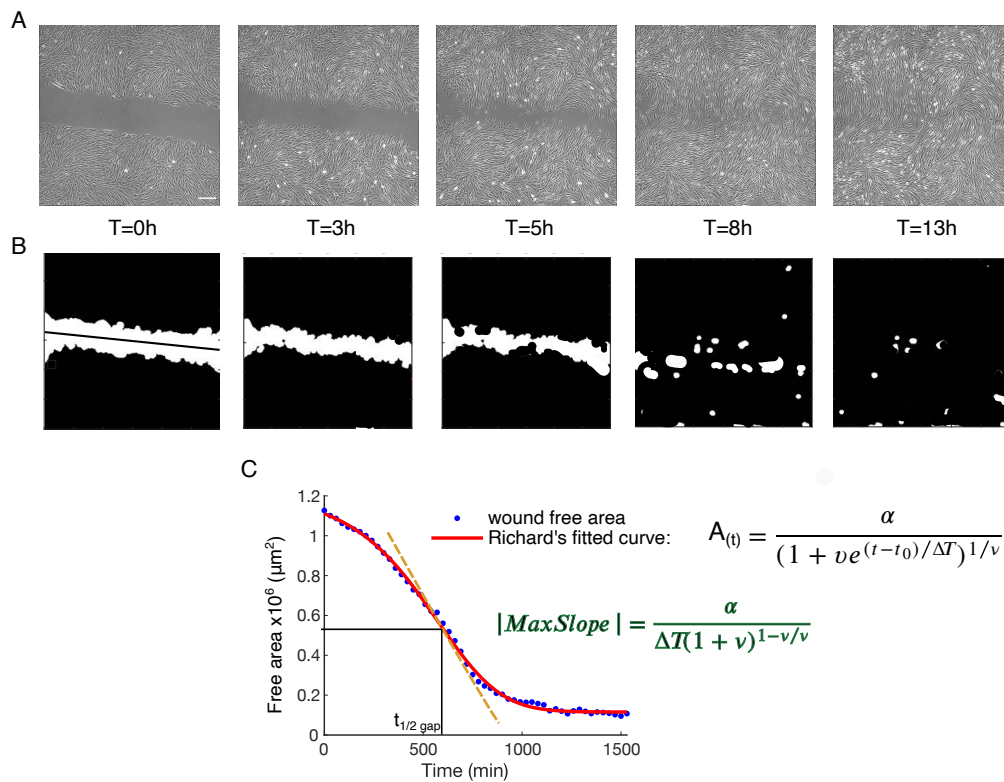


Figure V. Scratch assay experiments analysis and quantification.

A) Time series phase contrast images from the same field of view or wound region obtained with an automated microscope with an incubation chamber. Scale bar =250m.
B) Resulting masks obtained from the processing of images shown in panel A. White areas represent free cell zones and are used for the script to measure wounds or free areas. The black line in the middle of the first wound zone is automatically fitted

equidistant from the wound edges for linear edge velocity calculation (Cr). C) Free area versus time plot with data obtained from the analysis shown in the B panel. In blue are plotted wound-free areas at different times showing a negative sigmoid shape. In red we can see the adjusted Richard's equation. Richard's fit main equation and max slope equation are shown. Own source.

Independently of the image processing method applied, free areas by time can be used to calculate some measures related to the migration kinetics. A multitude of quantification methods had been described to quantify collective cell migration; some of the most common ones are based on wound width or area change⁴⁶. These methods use different metrics, like the percentage difference in the wound width at different time points¹⁰³, the wound at specific times¹⁰⁴, and the slope based on different fits.

Wound healing experiments can display a non-linear tendency, with a sigmoidal shape that can be locally approximated as a linear behavior. For those reasons and to simplify the process, some authors proposed a linear fit between the 5th and 12th hours, coinciding with the maximum slope of the sigmoid curve¹⁰⁵. Other functions, such as the Richard's function (non-symmetrical sigmoid) have been also proposed¹⁰⁶ (Figure V-C). In Richard's equation (Figure V-C) A represents the wound area, ΔT is the time between consecutive frames, and α , v , t_0 are the coefficients obtained from minimizing an objective function of the sum of squared errors between the experimental Areas vs. time plot. In this equation, the maximum slope of the fitted equation corresponds to the maximum cell migration rate and can be evaluated with the bottom equation in Figure V-C and represented in the plot with a golden line.

The slope of the Area vs time curve can be converted into a rate assuming that the wound length is constant and thus obtaining the width of the gap¹⁰⁷. Considering the migration rate is calculated for one of the two edges of the wound and combining all together, we obtain Equation 8 where m is the maximum slope and l is the length of

the field of view, represented for the black line in the middle of the wound in Figure V-B.

$$C_r = \frac{|m|}{2 \times l}$$

Equation 8.

Another useful measure we can obtain from wound healing assays is the time necessary to reduce one-half of the initial area $t_{1/2gap}$. That information can be useful to compare wound healing assay experiments with different initial gaps. The $t_{1/2gap}$ can be obtained graphically by setting $y = b/2$ and solving for x like seen in Figure V-C or calculated with Equation 9

$$t_{1/2gap} = \frac{\text{Initial Gap Area}}{2 \times |\text{Slope}|}$$

Equation 9.

***In vivo* wound healing rate determination**

The first reported skin cicatrization studies were performed in the 1910s. Carrel and Hartmann¹⁰⁸ performed an extensive study on men and guinea pig wounds and observed a greater healing rate at the beginning of the wound. These data were used by Du Noüy¹⁰⁹ to determine one of the first wound-healing equations. In this equation (Equation 10), S_T is the wound area at a certain time, S_0 is the initial area, K is the healing coefficient and T is the time in days. It was observed that the exponential decay equation fits well for most of the wounds except at the end part when wounds were smaller than 0.4 cm².

$$S_T = S_0 e^{-KT}$$

Equation 10.

In the following decades, several authors tested the equations proposed by Du Noüy in animal models¹¹⁰ and with human ulcers¹¹¹. Other authors opted to improve the published models to get a better fit also at the end of the wound or find a better reproducibility among the different etiologies of ulcers. In Equation 11, Wallenstein and Harold¹¹² introduced a variation from sigmoid Gompertz's function with an error component to accommodate the variability between patients and a constant value for a better fit¹¹³.

$$Y_i(t) = e^{\left\{0.69 \left[1 - e^{\left(-t\beta_i / 0.69 \right)} \right] \right\}} + \epsilon_i(t)$$

Equation 11.

Cukjati and colleagues¹¹⁴ tested three models, a linear model, and an exponential decay model, and introduced what they called a delayed exponential model (Equation 12). That delayed exponential model was the one that fits better for pressure ulcers. In that equation S_d is the wound surface area, S_0 is the initial fitted area, T is the delay, and is the delayed exponential healing rate.

$$S_d = \begin{cases} S_0; t \leq T \\ S_0 e^{-\theta_a(t-T)}; t > T \end{cases}$$

Equation 12.

Lately, Cukjati and colleagues⁸⁶ improved their delayed exponential model by integrating the perimeter of a circle in the equation and tested a more complex model based on a double exponential decay with four parameters or creating a rational four-parameters model. Other authors chose models based on other parameters such as the linear healing of the wound edge¹¹⁵ or the wound width and length¹¹⁶.

While more sophisticated and complex mathematical models appeared, their increasing number of parameters and complexity implies that a better background in mathematics was necessary to apply them and make also necessary the use of

mathematical programs to resolve it. That could be the reason why none of those models reached widespread acceptance among clinicians. In fact, 200 years later since the first model¹¹², the efficacy of treatments is mainly determined as a comparison of completely healed wounds versus not completely healed wounds on a chosen day or comparing the mean days necessary for the complete healing. Considering that the mentioned models demonstrate an effect of the initial wound area (S_0) the approaches used by clinicians cannot be used to predict the chance of healing or to project the total healing time¹¹¹. On the other hand, only a few attempts of using some of the described mathematical models for the prediction of wound evolution have been reported⁸⁷.

Appendix 3.

Microscopy techniques

Reflection interference contrast microscopy (RICM)

This optical microscopy technique was first used in 1961 on oil films and in 1964 it was applied for the first time to study animal cells. This technique uses reflected light to get topological information about the sample. The light is transmitted through the objective to a sample containing, e.g., cells attached to a glass surface. Rays reflected from the cell basal membrane and those reflected from the glass interfere, creating a characteristic pattern of fringes that can be captured for the camera. This pattern contains the information needed to determine the distance of the object from the glass surface, looking dark gray those cell zones more closely attached to the glass and light gray those cell parts with a higher distance from the glass⁶⁹. This technique is very useful to visualize adhesion structures like focal adhesions but also to get a clear image of the cell contour in the absence of a phase contrast objective.

Total internal reflection fluorescence microscopy

Total internal reflection fluorescence (TIRF) is a microscopy technique used with fluorescent samples to selectively excite fluorophores close to the glass-cell interface. When the light encounters the interface of two transparent materials with different refractive indexes light is partially reflected and partially diffracted. With a certain angle of laser beam incident θ_T at the interphase called critical angle θ_c , (Figure

VI-A) the light is completely reflected in a phenomenon called total internal reflection. Under this phenomenon, a portion of the energy from the incident light is converted to an electromagnetic field called an evanescent wave with the same wavelength as the incident light¹¹⁷. That evanescent wave decays exponentially while increasing the penetration depth, exciting only the fluorophores within the 100-200nm region above the glass. In fact, that technology reduces the background noise by 2000 folds compared with epifluorescence, improves the signal-to-noise ratio, and significantly reduces cell exposure to light¹¹⁸. As shown in representative images in Figure VI-B comparing epifluorescence illumination (left) versus TIRF (right), yellow arrows mark zones where epifluorescence images have blurred parts around the nucleus, where cells are higher. In TIRF images the blurring zone disappeared and the protein distribution in the basal cell membrane is clearly visible.

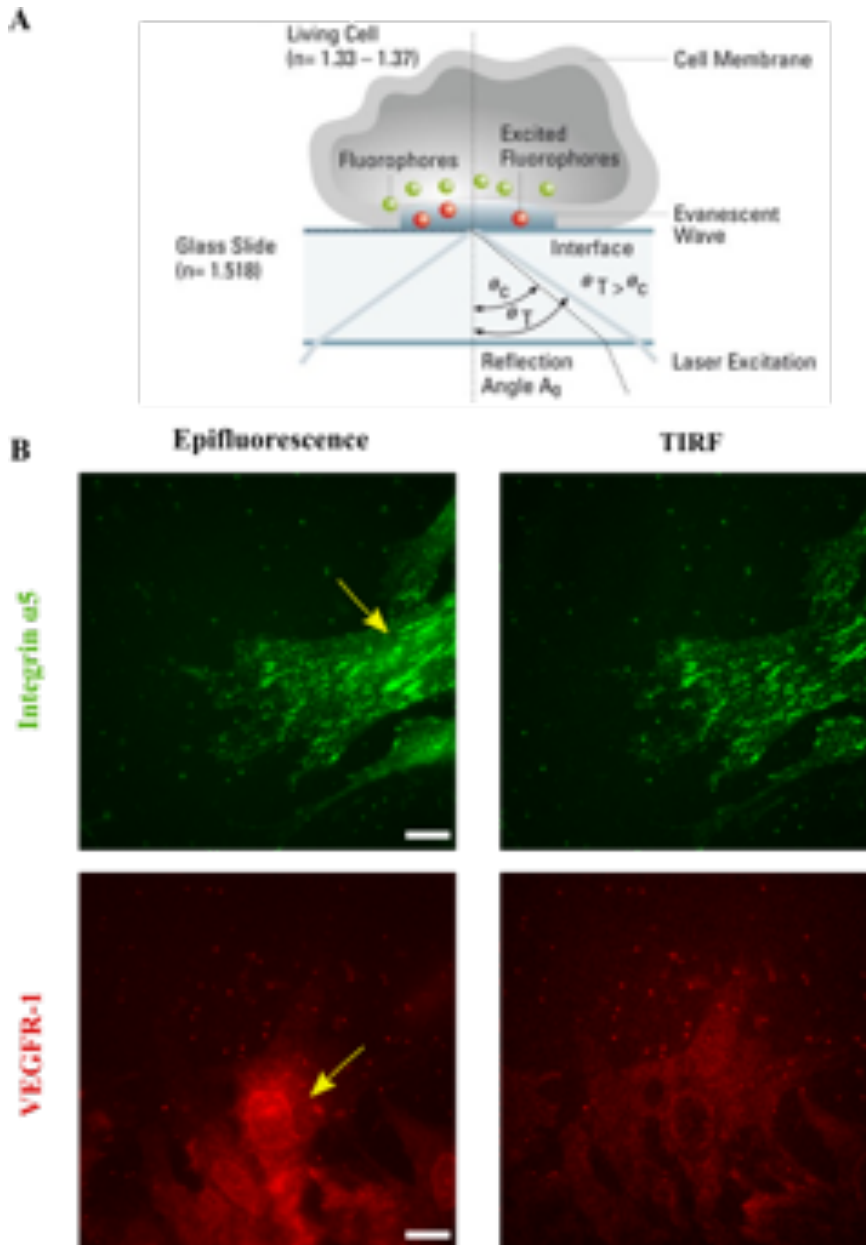


Figure VI. TIRF microscopy scheme and comparative of epifluorescence and TIRF images.

A) TIRF microscopy scheme showing the excitation, the reflection angle, and the evanescent wave. Adapted from Ref. ¹¹⁹. B) Comparative images of the same field of view with epifluorescence illumination (left) and with TIRF (right). The top images (green) show dermal fibroblast with integrin $\alpha 5$ immunostained. The bottom images (red) show dermal fibroblasts with VEGFR-1 immunostained. Yellow arrows indicate blurred zones in higher cell parts due to background fluorescence in epifluorescence. Scale bar = $15\mu m$. Own source

Single particle tracking

Single particle tracking (SPT) is a technique for the observation of individual molecule dynamics in living cells. Also known as single-molecule tracking (SMT), it was developed in the mid-1980s by Brabander and colleagues with the use of gold nanoparticles to visualize the surface of a living cell. In 1993, it was used to visualize individual fluorescent molecules or organic dyes. The main problem at the beginning was that the fast photobleaching of organic dyes restrict the detection to a few seconds¹²⁰. That problem was lately overcome by substituting organic dyes with semiconductor nanocrystals known as quantum dots (QDs) that allow the detection of fluorophores for long periods (even minutes). With the use of half-antibodies fragments (hAb) conjugated with QD (for detailed protocol see Appendix I) we can use biological affinity to label a subpopulation of the protein of interest, to capture their dynamics. Using TIRF illumination at a high temporal resolution (up to 40 kHz), a time-lapse movie is performed with excellent spatial localization precision (1-10 nm)¹²⁰. To capture the localization of each labeled protein, it is necessary to illuminate the sample with a laser and to acquire videos with a fast camera. After image acquisition, several steps of digital computing processing are necessary to detect each spot, get the centroid of each diffraction pattern, and connect the coordinates of the same spot across consecutive frames into trajectories⁶⁸ (Figure VII-A). The resulting trajectories can be later analyzed to get different parameters such as their type of motion, mean-squared displacement (Figure VII-B), mean diffusion, etc. (See Appendix 2 for detailed equations).

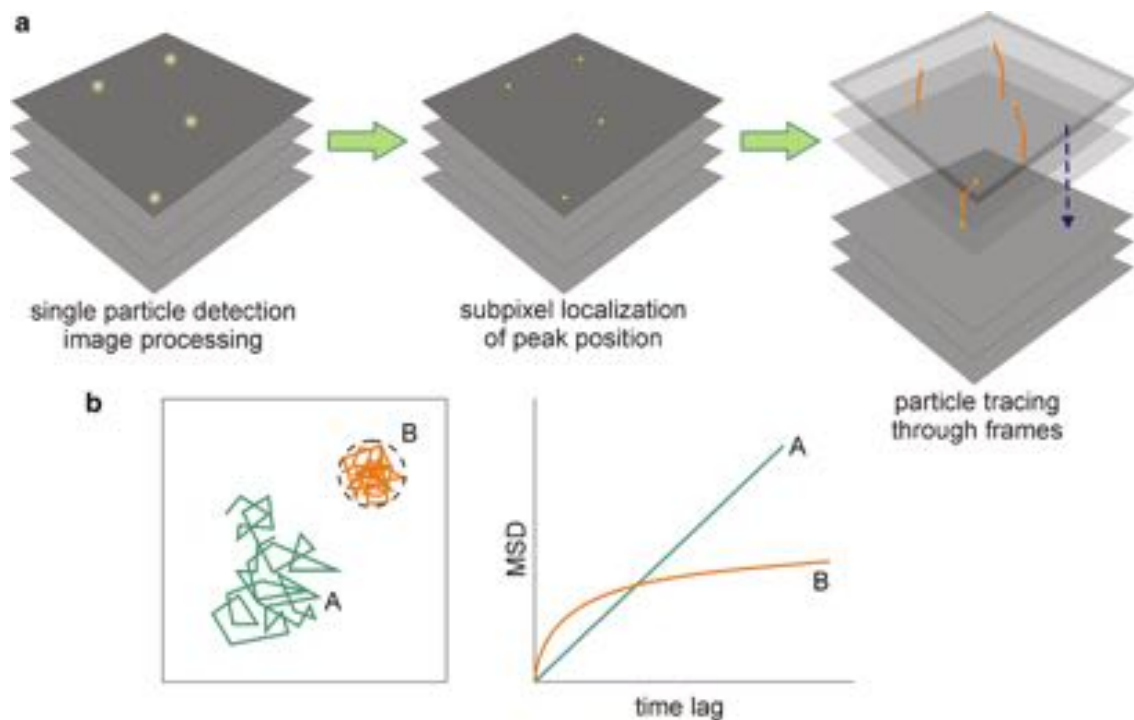


Figure VII. Schematic representation of the single particle tracking steps and posterior trajectory analysis.

a) Single particles are detected for each frame in a time-lapse movie. The raw images are computationally analyzed to get the coordinates of each spot in each frame. Then, fluorescence peaks are reduced to their centroid to achieve a subpixel localization. Localizations considered from the same fluorophore are connected in successive frames to get particle tracks. b) Representation of the single-particle trajectories analysis. Left: Examples of two trajectories of free-diffusing (A) and confined (B) particles are shown. Right: The corresponding mean-squared displacement vs lag time plot for the same particles⁶⁸.

Bibliography

1. Järbrink, K. *et al.* Prevalence and incidence of chronic wounds and related complications: a protocol for a systematic review. *Syst Rev* **5**, 1–6 (2016).
2. Espauella-Ferrer, M. *et al.* Assessment of frailty in elderly patients attending a multidisciplinary wound care centre: a cohort study. *BMC Geriatr* **21**, 1–9 (2021).
3. Kingston, A. *et al.* Projections of multi-morbidity in the older population in England to 2035: Estimates from the Population Ageing and Care Simulation (PACSim) model. *Age Ageing* **47**, 374–380 (2018).
4. Otero-Viñas, M. & Falanga, V. Mesenchymal Stem Cells in Chronic Wounds: The Spectrum from Basic to Advanced Therapy. *Adv Wound Care (New Rochelle)* **5**, 149–163 (2016).
5. Falanga, V. *et al.* Autologous Cultured Bone Marrow-Derived Mesenchymal Stem Cells in a Fibrin Spray to Treat Venous Ulcers: A Randomized Controlled Double-Blind Pilot Study. *Surg Technol Int* **40**, 47–54 (2022).
6. Soldevilla Agreda, J. J. *et al.* Una aproximación al impacto del coste económico del tratamiento de las úlceras por presión en España. *Gerokomos* **18**, (2007).
7. Sen, C. K. *et al.* Human skin wounds: a major and snowballing threat to public health and the economy. *Wiley Online Library* **17**, 763–771 (2009).
8. Lopez-Ojeda, W., Pandey, A., Alhaji, M. & Oakley, A. M. Anatomy, Skin (Integument). *StatPearls* (2021).
9. Tavakoli, S. & Klar, A. S. Advanced Hydrogels as Wound Dressings. *Biomolecules* **10**, 1169 (2020).
10. Kular, J. K., Basu, S. & Sharma, R. I. The extracellular matrix: Structure, composition, age-related differences, tools for analysis and applications for tissue engineering. *J Tissue Eng* **5**, (2014).
11. Thariseoch, A. D., Skandalis, S. S., Gialeli, C. & Karamanos, N. K. Extracellular matrix structure. *Adv Drug Deliv Rev* **97**, 4–27 (2016).
12. Zhu, J. & Clark, R. A. F. Fibronectin at Select Sites Binds Multiple Growth Factors and Enhances their Activity: Expansion of the Collaborative ECM-GF Paradigm. *Journal of Investigative Dermatology* **134**, 895–901 (2014).
13. Koivisto, L., Heino, J., Häkkinen, L. & Larjava, H. Integrins in Wound Healing. *Adv Wound Care (New Rochelle)* **3**, 762–783 (2014).

14. Wijelath, E. S. *et al.* Heparin-II domain of fibronectin is a vascular endothelial growth factor-binding domain: enhancement of VEGF biological activity by a singular growth factor/matrix protein synergism. *Circ Res* **99**, 853–860 (2006).
15. Gurtner, G. C., Werner, S., Barrandon, Y. & Longaker, M. T. Wound repair and regeneration. *Nature* **453**, 314–321 (2008).
16. Lawrence, W. T. Physiology of the acute wound. *Clin Plast Surg* **25**, 321–340 (1998).
17. Broughton, G., Janis, J. E. & Attinger, C. E. Wound healing: An overview. *Plast Reconstr Surg* **117**, (2006).
18. Ennis, W. J. & Meneses, P. Wound healing at the local level: the stunned wound. *Ostomy/wound management* vol. 46 Preprint at <https://europepmc.org/article/med/10732639> (2000).
19. Levinson, H. A Paradigm of Fibroblast Activation and Dermal Wound Contraction to Guide the Development of Therapies for Chronic Wounds and Pathologic Scars. *Adv Wound Care (New Rochelle)* **2**, 149–159 (2013).
20. Singer, A. J. & Clark, R. A. F. Cutaneous Wound Healing. *N Engl J Med* **341**, 738–746 (1999).
21. Velnar, T., Bailey, T. & Smrkolj, V. The Wound Healing Process: an Overview of the Cellular and Molecular Mechanisms. *J Int Med Res* **37**, 1528 (2009).
22. Ferrara, N. VEGF: an update on biological and therapeutic aspects. *Curr Opin Biotechnol* **11**, 617–624 (2000).
23. Baum, C. L. & Arpey, C. J. Normal Cutaneous Wound Healing: Clinical Correlation with Cellular and Molecular Events. *Dermatologic Surgery* **31**, 674–686 (2005).
24. Falanga, V. Wound healing and chronic wounds. *J Cutan Med Surg* **3**, (1998).
25. Dubhashi, S. P. & Sindwani, R. D. A Comparative Study of Honey and Phenytoin Dressings for Chronic Wounds. *Indian Journal of Surgery* **77**, 1209–1213 (2015).
26. Falanga, V. *et al.* Chronic wounds. *Nat Rev Dis Primers* **8**, 1–21 (2022).
27. Lazarus, G. S. *et al.* Definitions and guidelines for assessment of wounds and evaluation of healing. *Wound Repair and Regeneration* **2**, 165–170 (1994).
28. Khanna, A. K. & Tiwary, S. K. *Ulcers of the lower extremity. Ulcers of the Lower Extremity* (Springer India, 2016). doi:10.1007/978-81-322-2635-2.

29. Pereira, S. G., Moura, J., Carvalho, E. & Empadinhas, N. Microbiota of chronic diabetic wounds: Ecology, impact, and potential for innovative treatment strategies. *Front Microbiol* **8**, (2017).
30. Mervis, J. S. & Phillips, T. J. Pressure ulcers: Pathophysiology, epidemiology, risk factors, and presentation. *J Am Acad Dermatol* **81**, 881–890 (2019).
31. Boyko, T. v., Longaker, M. T. & Yang, G. P. Review of the Current Management of Pressure Ulcers. *Adv Wound Care (New Rochelle)* **7**, 57–67 (2018).
32. Sriram, G., Bigliardi, P. L. & Bigliardi-Qi, M. Fibroblast heterogeneity and its implications for engineering organotypic skin models in vitro. *Eur J Cell Biol* **94**, 483–512 (2015).
33. Mitra, M., Ho, L. D. & Collier, H. A. An in vitro model of cellular quiescence in primary human dermal fibroblasts. *Methods in molecular biology* **1686**, 27–47 (2018).
34. Otero-Vinas, M., Lin, X., Carson, P., Maclauchlan, S. & Falanga, V. Dermal Fibroblasts from Chronic Wounds Exhibit Paradoxically Enhanced Proliferative and Migratory Activities that May be Related to the Non-Canonical Wnt Signaling Pathway. *Surg Technol Int* **39**, 1–8 (2021).
35. Aragona, M. *et al.* A mechanical checkpoint controls multicellular growth through YAP/TAZ regulation by actin-processing factors. *Cell* **154**, 1047–1059 (2013).
36. Fan, Y. & Meyer, T. Molecular control of cell density-mediated exit to quiescence. *Cell Rep* **36**, 109436 (2021).
37. Pakshir, P. *et al.* The myofibroblast at a glance. *J Cell Sci* **133**, (2020).
38. Lichtman, M. K., Otero-Vinas, M. & Falanga, V. Transforming growth factor beta (TGF- β) isoforms in wound healing and fibrosis. *Wound repair and regeneration* **24**, 215–222 (2016).
39. Lu, P. & Lu, Y. Born to Run? Diverse Modes of Epithelial Migration. *Front Cell Dev Biol* **9**, 2187 (2021).
40. Ridley, A. J. *et al.* Cell Migration: Integrating Signals from Front to Back. *Science (1979)* **302**, 1704–1709 (2003).
41. Tschumperlin, D. J., Shively, J. D., Kikuchi, T. & Drazen, J. M. Mechanical stress triggers selective release of fibrotic mediators from bronchial epithelium. *Am J Respir Cell Mol Biol* **28**, 142–149 (2003).
42. Mayor, R. & Etienne-Manneville, S. The front and rear of collective cell migration. *Nature Reviews Molecular Cell Biology* 2016 17:2 **17**, 97–109 (2016).

43. Roycroft, A. & Mayor, R. Molecular basis of contact inhibition of locomotion. *Cellular and Molecular Life Sciences* **73**, 1119–1130 (2016).
44. Theveneau, E. & Mayor, R. Collective cell migration of epithelial and mesenchymal cells. *Cellular and Molecular Life Sciences* **70**, 3481–3492 (2013).
45. Scarpa, E. & Mayor, R. Collective cell migration in development. *Journal of Cell Biology* **212**, 143–155 (2016).
46. Grada, A., Otero-Vinas, M., Prieto-Castrillo, F., Obagi, Z. & Falanga, V. Research Techniques Made Simple: Analysis of Collective Cell Migration Using the Wound Healing Assay. *Journal of Investigative Dermatology* **137**, 11–16 (2017).
47. Humphries, J. D., Byron, A. & Humphries, M. J. Integrin ligands at a glance. *J Cell Sci* **119**, 3901–3903 (2006).
48. Bonus, M., Häussinger, D. & Gohlke, H. Liver cell hydration and integrin signaling. *Biol Chem* **402**, 1033–1045 (2021).
49. Barczyk, M. M. *et al.* A role for $\alpha 11 \beta 1$ integrin in the human periodontal ligament. *J Dent Res* **88**, 621–626 (2009).
50. Harburger, D. S. & Calderwood, D. A. Integrin signalling at a glance. *J Cell Sci* **122**, 159–163 (2009).
51. Galbraith, C. G., Davidson, M. W. & Galbraith, J. A. Coupling integrin dynamics to cellular adhesion behaviors. *Biol Open* **7**, (2018).
52. Plopper, G. E., McNamee, H. P., Dike, L. E., Bojanowski, K. & Ingber, D. E. Convergence of integrin and growth factor receptor signaling pathways within the focal adhesion complex. *Mol Biol Cell* **6**, 1349–1365 (1995).
53. Kurisinkal, E., Caroprese, V., Koga, M., Molecules, D. M.- & 2022, undefined. Selective Integrin $\alpha 5 \beta 1$ Targeting through Spatially Constrained Multivalent DNA-Based Nanoparticles. *Molecules* **27**, 4968 (2022).
54. Razyieva, K. *et al.* Immunology of Acute and Chronic Wound Healing. *Biomolecules* **11**, 700 (2021).
55. Li, G. *et al.* Expression and influence of matrix metalloproteinase-9/tissue inhibitor of metalloproteinase-1 and vascular endothelial growth factor in diabetic foot ulcers. *International Journal of Lower Extremity Wounds* **16**, 6–13 (2017).
56. Salcedo, X. *et al.* Review article: Angiogenesis soluble factors as liver disease markers. *Aliment Pharmacol Ther* **22**, 23–30 (2005).

57. Nash, A. D., Baca, M., Wright, C. & Scotney, P. D. The biology of vascular endothelial growth factor-B (VEGF-B). *Pulm Pharmacol Ther* **19**, 61–69 (2006).
58. Zhou, K., Ma, Y. & Brogan, M. S. Chronic and non-healing wounds: The story of vascular endothelial growth factor. *Med Hypotheses* **85**, 399–404 (2015).
59. Shaik, F. *et al.* Structural Basis for Vascular Endothelial Growth Factor Receptor Activation and Implications for Disease Therapy. *Biomolecules* **10**, 1673 (2020).
60. Cianfarani, F. *et al.* Placenta growth factor in diabetic wound healing: Altered expression and therapeutic potential. *American Journal of Pathology* **169**, 1167–1182 (2006).
61. Shibuya, M. & Claesson-Welsh, L. Signal transduction by VEGF receptors in regulation of angiogenesis and lymphangiogenesis. *Exp Cell Res* **312**, 549–560 (2006).
62. Hu, Z., Mellor, J., Wu, J. & DeLisi, C. VisANT: An online visualization and analysis tool for biological interaction data. *BMC Bioinformatics* **5**, (2004).
63. Martino, M. M. *et al.* Engineering the growth factor microenvironment with fibronectin domains to promote wound and bone tissue healing. *Sci Transl Med* **3**, (2011).
64. Ferrer Solà, M. Atenció a les ferides complexes en unitats clíniques de ferides. *TDX (Tesis Doctorals en Xarxa)* (2017).
65. Ferrer-Solà, M., Otero-Viñas, M., Sureda-Vidal, H. & Espauella-Panicot, J. Autologous Platelets-rich-plasma is a safe and efficient method to promote wound healing in a clinical wound unit. *WUWHs Abstracts supplement* 188–188 (2016).
66. Everts, P. A. M. *et al.* Platelet-Rich Plasma and Platelet Gel: A Review. *J Extra Corpor Technol* **38**, 174 (2006).
67. Eppley, B. L., Woodell, J. E. & Higgins, J. Platelet quantification and growth factor analysis from platelet-rich plasma: Implications for wound healing. *Plast Reconstr Surg* **114**, 1502–1508 (2004).
68. García-Sáez, A. J. & Schwille, P. Single molecule techniques for the study of membrane proteins. *Appl Microbiol Biotechnol* **76**, 257–266 (2007).
69. Curtis, A. S. The mechanism of adhesion of cells to glass. A study by interference reflection microscopy. *J Cell Biol* **20**, 199–215 (1964).
70. Jørgensen, L. B., Sørensen, J. A., Jemec, G. B. E. & Yderstræde, K. B. Methods to assess area and volume of wounds – a systematic review. *Int Wound J* **13**, 540–553 (2016).

71. Foltynski, P. *et al.* Wound area measurement with digital planimetry: Improved accuracy and precision with calibration based on 2 rulers. *PLoS One* **10**, 1–13 (2015).
72. O’Meara, S. M., Bland, J. M., Dumville, J. C. & Cullum, N. A. Systematic review of wound measurement instruments. *Wound Repair and Regeneration* **20**, 263–276 (2012).
73. LeCun, Y., Haffner, P., Bottou, L. & Bengio, Y. Object recognition with gradient-based learning. *Lecture Notes in Computer Science (including subseries Lecture Notes in Artificial Intelligence and Lecture Notes in Bioinformatics)* **1681**, 319–345 (1999).
74. Litjens, G. *et al.* A survey on deep learning in medical image analysis. *Med Image Anal* **42**, 60–88 (2017).
75. Ghosh, S., Das, N., Das, I. & Maulik, U. Understanding Deep Learning Techniques for Image Segmentation. *ACM Computing Surveys (CSUR)* **52**, (2019).
76. Codella, N. C. F. *et al.* Skin lesion analysis toward melanoma detection: A challenge at the 2017 International symposium on biomedical imaging (ISBI), hosted by the international skin imaging collaboration (ISIC). *Proceedings - International Symposium on Biomedical Imaging 2018-April*, 168–172 (2018).
77. Esteva, A. *et al.* Dermatologist-level classification of skin cancer with deep neural networks. *Nature* **542**, 115–118 (2017).
78. Codella, N. *et al.* Deep learning, sparse coding, and SVM for melanoma recognition in dermoscopy images. *Lecture Notes in Computer Science (including subseries Lecture Machine Learning in Medical Imaging)* **9352**, 118–126 (2015).
79. Marchetti, M. A. *et al.* Results of the 2016 International Skin Imaging Collaboration International Symposium on Biomedical Imaging challenge: Comparison of the accuracy of computer algorithms to dermatologists for the diagnosis of melanoma from dermoscopic images. *J Am Acad Dermatol* **78**, 270-277.e1 (2018).
80. Tschandl, P. *et al.* Comparison of the accuracy of human readers versus machine-learning algorithms for pigmented skin lesion classification: an open, web-based, international, diagnostic study. *Lancet Oncol* **20**, 938–947 (2019).
81. Wang, C. *et al.* Fully automatic wound segmentation with deep convolutional neural networks. *Sci Rep* **10**, 1–9 (2020).
82. Shibuya, M. Vascular Endothelial Growth Factor (VEGF) and Its Receptor (VEGFR) Signaling in Angiogenesis: A Crucial Target for Anti- and Pro-Angiogenic Therapies. *Genes Cancer* **2**, 1097 (2011).

83. Mason, D. E. *et al.* YAP and TAZ limit cytoskeletal and focal adhesion maturation to enable persistent cell motility. *Journal of Cell Biology* **218**, 1369–1389 (2019).
84. Rausch, V. & Hansen, C. G. The Hippo Pathway, YAP/TAZ, and the Plasma Membrane. *Trends Cell Biol* **30**, 32–48 (2020).
85. Cukjati, D., Reberšek, S. & Miklavčič. A reliable method of determining wound healing rate. *Med Biol Eng Comput* **39**, 263–271 (2001).
86. Cukjati, D., Reberšek, S., Karba, R. & Miklavčič, D. Modelling of chronic wound healing dynamics. *Med Biol Eng Comput* **38**, 339–347 (2000).
87. Robnik-Šikonja, M., Cukjati, D. & Kononenko, I. Comprehensible evaluation of prognostic factors and prediction of wound healing. in *Artificial Intelligence in Medicine* vol. 29 25–38 (2003).
88. Markovic-Mueller, S. *et al.* Structure of the Full-length VEGFR-1 Extracellular Domain in Complex with VEGF-A. *Structure* **25**, 341–352 (2017).
89. Harris, L. J., Skaletsky, E. & McPherson, A. Crystallographic structure of an intact IgG1 monoclonal antibody. *J Mol Biol* **275**, 861–872 (1998).
90. Tinevez, J. Y. *et al.* TrackMate: An open and extensible platform for single-particle tracking. *Methods* **115**, 80–90 (2017).
91. Qian, H., Sheetz, M. P. & Elson, E. L. Single particle tracking. Analysis of diffusion and flow in two-dimensional systems. *Biophys J* **60**, 910–921 (1991).
92. Saxton, M. J. & Jacobson, K. Single-particle tracking: Applications to membrane dynamics. *Annu Rev Biophys Biomol Struct* **26**, 373–399 (1997).
93. Jaqaman, K., Galbraith, J. A., Davidson, M. W. & Galbraith, C. G. Changes in single-molecule integrin dynamics linked to local cellular behavior. *Mol Biol Cell* **27**, 1561 (2016).
94. Wang, Y., Jeong, Y., Jhiang, S. M., Yu, L. & Menq, C. H. Quantitative Characterization of Cell Behaviors through Cell Cycle Progression via Automated Cell Tracking. *PLoS One* **9**, e98762 (2014).
95. Klein, H. L. *et al.* Guidelines for DNA recombination and repair studies: Cellular assays of DNA repair pathways. *Microbial Cell* **6**, 1 (2019).
96. Jaqaman, K. *et al.* Robust single-particle tracking in live-cell time-lapse sequences. *Nat Methods* **5**, 695–702 (2008).
97. Ferrari, R., Manfroi, A. J. & Young, W. R. Strongly and weakly self-similar diffusion. *Physica D* **154**, 111–137 (2001).

98. Arts, M., Smal, I., Paul, M. W., Wyman, C. & Meijering, E. Particle Mobility Analysis Using Deep Learning and the Moment Scaling Spectrum. *Sci Rep* **9**, (2019).
99. Meijering, E., Dzyubachyk, O. & Smal, I. Methods for Cell and Particle Tracking. *Methods Enzymol* **504**, 183–200 (2012).
100. Stamm, A. *et al.* In vitro wound healing assays - State of the art. *BioNanoMaterials* **17**, 79–87 (2016).
101. Cortesi, M., Pasini, A., Tesei, A. & Giordano, E. AIM: A Computational Tool for the Automatic Quantification of Scratch Wound Healing Assays. *Applied Sciences* **7**, 1237 (2017).
102. Vargas, A. *et al.* Robust quantitative scratch assay. *Bioinformatics* **32**, 1439–1440 (2016).
103. Walter, M. N. M., Wright, K. T., Fuller, H. R., MacNeil, S. & Johnson, W. E. B. Mesenchymal stem cell-conditioned medium accelerates skin wound healing: An in vitro study of fibroblast and keratinocyte scratch assays. *Exp Cell Res* **316**, 1271–1281 (2010).
104. Büth, H. *et al.* Cathepsin B is essential for regeneration of scratch-wounded normal human epidermal keratinocytes. *Eur J Cell Biol* **86**, 747–761 (2007).
105. Kauanova, S., Urazbayev, A. & Vorobjev, I. The Frequent Sampling of Wound Scratch Assay Reveals the “Opportunity” Window for Quantitative Evaluation of Cell Motility-Impeding Drugs. *Front Cell Dev Biol* **9**, 391 (2021).
106. Topman, G., Sharabani-Yosef, O. & Gefen, A. A standardized objective method for continuously measuring the kinematics of cultures covering a mechanically damaged site. *Med Eng Phys* **34**, 225–232 (2012).
107. Bobadilla, A. V. P. *et al.* In vitro cell migration quantification method for scratch assays. *J R Soc Interface* **16**, (2019).
108. Carrel, A. & Hartmann, A. Cicatrization of wounds: I. The relation between the size of a wound and the rate of its cicatrization. *Journal of Experimental Medicine* **24**, 429–450 (1916).
109. du Noüy, P. L. Cicatrization of wounds: X. a general equation for the law of cicatrization of surface wounds. *Journal of Experimental Medicine* **29**, 329–350 (1919).
110. Billingham, R. E. & Russell, P. S. Studies on wound healing, with special reference to the phenomenon of contracture in experimental wounds in rabbits' skin. *Ann Surg* **144**, 961–981 (1956).
111. Cardinal, M. *et al.* Nonlinear modeling of venous leg ulcer healing rates. *BMC Dermatol* **9**, 2 (2009).

112. Gompertz, B. XXIV. On the nature of the function expressive of the law of human mortality, and on a new mode of determining the value of life contingencies. In a letter to Francis Baily, Esq. F. R. S. &c. *Philos Trans R Soc Lond* **115**, 513–583 (1825).
113. Wallenstein, S. & Brem, H. Statistical analysis of wound-healing rates for pressure ulcers. *Am J Surg* **188**, 73–78 (2004).
114. Cukjati, D., Reberšek, S., Karba, R. & Miklavčič, D. Mathematical modeling of chronic wound healing. *Electromagn Biol Med* **17**, 237–242 (1998).
115. Gorin, D. R., Cordts, P. R., LaMorte, W. W. & Menzoian, J. O. The influence of wound geometry on the measurement of wound healing rates in clinical trials. *J Vasc Surg* **23**, 524–528 (1996).
116. Lyman, I. R., Tenery, J. H. & Basson, R. P. Correlation between decrease in bacterial load and rate of wound healing. *Surg Gynecol Obstet* **130**, 616–621 (1970).
117. Fish, K. N. Total Internal Reflection Fluorescence (TIRF) Microscopy. *Curr Protoc Cytom* **50**, 12–18 (2009).
118. Funatsu, T., Harada, Y., Tokunaga, M., Saito, K. & Yanagida, T. Imaging of single fluorescent molecules and individual ATP turnovers by single myosin molecules in aqueous solution. *Nature* **374**, 555–559 (1995).
119. Parhamifar, L. & Moghimi, S. M. Total internal reflection fluorescence (TIRF) microscopy for real-time imaging of nanoparticle-cell plasma membrane interaction. *Methods in Molecular Biology* **906**, 473–482 (2012).
120. Manzo, C. & Garcia-Parajo, M. F. A review of progress in single particle tracking: from methods to biophysical insights. *Reports on Progress in Physics* **78**, 124601 (2015).